**UNIVERSIDADE DE SÃO PAULO**
FACULDADE DE CIÊNCIAS FARMACÊUTICAS
Programa de Pós-Graduação em Tecnologia Bioquímico-Farmacêutica
Área de Tecnologia de Fermentações

# Nanopartículas de quitosana e derivado carboximetilado como sistemas de fornecimento (*delivery)* de produtos biológicos: preparo, caracterização, estabilidade e avaliação *in vitro*/*in vivo*

**Natalia Marchesan Bexiga**

Tese para obtenção do grau de
DOUTOR

Orientador:
Prof. Dr. Marco Antônio Stephano

São Paulo
2018

Natalia Marchesan Bexiga

# Nanopartículas de quitosana e derivado carboximetilado como sistemas de fornecimento (*delivery*) de produtos biológicos: preparo, caracterização, estabilidade e avaliação *in vitro*/*in vivo*

Tese apresentada à Faculdade de Ciências Farmacêuticas da Universidade de São Paulo para obtenção do título de Doutor em Ciências Farmacêuticas

Área de Concentração: Fermentacões

Orientador: Prof. Dr. Marco Antonio Stephano

São Paulo
2018

Natalia Marchesan Bexiga

Nanopartículas de quitosana e derivado carboximetilado como sistemas de fornecimento (*delivery*) de produtos biológicos: preparo, caracterização, estabilidade e avaliação *in vitro*/*in vivo*

Comissão Julgadora
do
Tese para obtenção do grau de Doutor

Prof. Dr. Marco Antônio Stephano
Orientador/presidente

Professor_____Assinatura_____
1º examinador

Professor_____Assinatura_____
2º examinador

Professor_____Assinatura_____
3º examinador

Professor_____Assinatura_____
4º examinador

São Paulo, Outubro, 2018

## DEDICATÓRIA

Dedico este trabalho primeiramente a Deus que me deu forças em todos os momentos e inteligência para a conclusão desse projeto. Sem Ele, nada disso teria sido possível.

Ao meu pai, João Roberto Bexiga, que sempre esteve ao meu lado em todos os momentos, fáceis e difíceis. Ele é o meu exemplo de honestidade, caráter e dedicação.

A minha mãe Luisa Marchesan, que sempre me apoiou, incentivou, e me deu o suporte que eu necessitava para a conclusão deste grande desafio.

Ao meu orientador Marco Antonio Stephano, por ter sido sobretudo um grande amigo e conselheiro, e que me ensinou o verdadeiro significado da palavra “pesquisador”, fazendo com que eu me tornasse a pessoa que sou hoje.

Aos professores Adriano Mesquita Alencar do Instituto de Física da USP e Steven S. An, da Johns Hopkins Bloomberg School of Public Health, pela grande oportunidade e orientação durante o meu estágio no exterior. Agradeço pela amizade e orientação de valor inestimável em minha vida profissional.

Ao meu companheiro, Marcelo Gallon da Silva, pelo carinho e apoio incondicionais, pelas orientações e encorajamento, sobretudo nos momentos mais difíceis. Você é o meu grande exemplo de profissionalismo, dedicação e humildade.

## AGRADECIMENTOS

Agradeço primeiramente à Faculdade de Ciências Farmacêuticas pela formação e oportunidade de concluir meu doutorado.

Às agências de fomento CAPES (Coordenação de Aperfeiçoamento de Pessoal de Nível Superior) pelo apoio financeiro, e FAPESP (Fundação de Amparo à Pesquisa do Estado de São Paulo), pela oportunidade de participar do evento *Sao Paulo School of Advance Sciences on Vaccines*.

A toda secretaria do Departamento de Tecnologia Bioquímico-Farmacêutica por toda atenção e auxílio, imprescindíveis durante o meu curso de doutorado.

Aos professores da FCF que, desde o meu curso de mestrado, me apoiaram e me incentivaram a seguir este caminho.

Ao Dr. Steven An que, com seu todo seu conhecimento, auxiliou na minha formação e conclusão deste trabalho de doutorado.

A Jessie Huang, minha colega de laboratório da Bloomberg School of Public Health, que me auxiliou nos experimentos de citometria óptica de torção magnética.

A todos os meus amigos por sua dedicação e carinho, que estiveram ao meu lado durante toda essa jornada. Agradeço em especial a Carolina Raíssa Costa Picossi pelo seu enorme companheirismo e apoio, ao Bruno Bitarães Neto Salgado Brandão pelas inúmeras risadas e parceria, e à Sibylle Sophie Hacker pelos conselhos valorosos.

**“[Great scientists] are men of bold ideas, but highly critical of their own ideas: they try to find whether their ideas are right by trying first to find whether they are not perhaps wrong. They work with bold conjectures and severe attempts at refuting their own conjectures”.**

*(Karl Popper)*

# RESUMO

BEXIGA, N. M. **Nanopartículas de quitosana e derivado carboximetilado como sistemas de fornecimento (*delivery*) de produtos biológicos: preparo, caracterização, estabilidade e avaliação *in vitro*/*in vivo*.** 2018. Número de folhas f. 177. Tese (Doutorado) – Faculdade de Ciências Farmacêuticas, Universidade de São Paulo, São Paulo, 2018.

A quitosana é um polímero mucoadesivo biocompatível e biodegradável, com vantagens únicas, tais como a característica distinta de abrir as junções que permitim o transporte paracelular de antígenos e boa tolerabilidade. No entanto, sua baixa solubilidade em meios neutros ou alcalinizados tem restringido suas aplicações no campo farmacêutico. A quitosana pode ser facilmente carboximetilada para melhorar de sua solubilidade em meios aquosos, enquanto sua biodegradabilidade e biocompatibilidade são preservadas. Além disso, a carboximetilquitosana (CMCS) pode ser facilmente processada na forma de nanopartículas, o que destaca sua adequabilidade para uso extensivo no preparo de sistemas de *delivery* de medicamentos. O presente estudo trata do desenvolvimento e caracterização de um sistema de *delivery* baseado em nanopartículas de CMCS utilizando ovalbumina como proteína modelo. Nós demonstramos que as nanopartículas carregadas com ovalbumina foram sintetizadas com sucesso utilizando cloreto de cálcio como agente de reticulação por gelificação iônica. As nanopartículas exibiram um tamanho médio de aproximadamente 169 nm e apresentaram uma forma pseudo-esférica. O tamanho das nanopartículas aumentou de acordo com a adição de $CaCl_2$ devido à forte atração eletrostática. Durante o armazenamento, o tamanho aumentado das nanopartículas foi atribuído a incorporação de água e agregação. A eficiência de encapsulamento da ovalbumina foi de aproximadamente 17%. A microscopia confocal mostrou claramente a associação entre ovalbumina e a cadeias de CMCS nas nanopartículas. Sugerimos, portanto, que tal sistema pode ser considerado como candidato atraente e promissor para o carreamento de proteínas e antígenos. O principal desafio que limita o uso desses carreadores consiste na instabilidade em meio aquoso. Assim, o próximo passo deste trabalho foi determinar a robustez de várias formulações utilizando-se diferentes protocolos de liofilização. Este estudo demonstrou que o manitol em uma concentração de 10% (p/v) é adequado para preservar da agregação as nanocápsulas de CMCS carregadas com ovalbumina durante a liofilização e subsequente reconstituição. Mais importante, os resultados mostraram que uma etapa de *annealing* tem um enorme impacto sobre a porosidade da amostra liofilizada devido a quase completa cristalização do manitol, uma vez que a matriz cristalina evita o colapso parcial e a formação de poros maiores observados na ausência do *annealing*. Portanto, a observação comum de que o *annealing* aumenta o tamanho doporos devido ao crescimento dos cristais de gelo nem sempre se aplica, pelo menos quando a cristalização de um soluto está envolvida. Uma vez que todas as caracterizações e estudos de estabilidade foram realizados, o principal objetivo deste estudo foi desenvolver um sistema estável de *delivery* de antígeno para imunização oral utilizando CMCS e vírus rábico inativado (RV) como antígeno. Verificou-se que as nanopartículas carregadas com RV aumentam as respostas imune sistêmica (IgG) e local (IgA) contra o RV após administração oral em camundongos. As doses efetivas 50% foram 50 vezes maiores que os controles negativos, indicando que a resposta imune foi iniciada apenas após a terceira dose da vacina. Além disso, foram produzidos anticorpos neutralizantes suficientes para proteção contra os efeitos nocivos do vírus rábico. Conclui-se, portanto, que as nanopartículas de CMCS formuladas neste estudo, são adequadas para o *delivery* oral de vacinas, e podem ser sugeridas como um sistema promissor de *delivery* para uma gama diversa de antígenos, bem como para o *delivery* de genes/proteínas, especialmente para aqueles carregados positivamente. Uma vez que diversas abordagens mostram que uma intervenção efetiva em casos de inflamação alérgica de vias aéreas pode ser conseguida por meio de células secretoras de interleucina 10 (IL-10) mediante ativação por alergenos, a parte final deste trabalho esteve dedicada a avaliação de nanopartículas de quitosana carregadas com IL-10 (IL10-CSNPs) como possível ferramenta terapêutica inalável para prevenção de exacerbações em pacientes asmáticos. Como controles positivos, avaliou-se adicionalmente se as interleucinas 17A (IL-17A) e 9 (IL-9) possuem a capacidade de estimular a contratilidade de células humanas de músculo liso de vias aéreas humanas (HASM) por meio de citometria de torção magnética (MTC). Uma diminuição significativa da rigidez celular basal foi observada em células HASM pré-tratadas com IL-10, mas não com IL10-CSNPs, enquanto que o tratamento com IL-17A aumentou significativamente a magnitude rigidez celular basal. Nossos resultados revelam um mecanismo previamente desconhecido subjacente à imunoterapia para prevenção e tratamento da asma.

**Palavras-chave:** Nanopartículas**,** carboximetil quitosana, vírus rábico, imunização de mucosa, interleucinas, rigidez celular, células humanas de músculo liso de via aéreas, asma

# ABSTRACT

**BEXIGA, N. M. Chitosan and carboxymethylated derivative nanoparticles as delivery systems for biological products: preparation, characterization, stability and *in vitro*/*in vivo* evaluation.** 2018. Número de folhas f. 177. Tese (Doutorado) – Faculdade de Ciências Farmacêuticas, Universidade de São Paulo, São Paulo, 2018.

Chitosan is a biocompatible and biodegradable mucoadhesive polymer with unique advantages, such as the distinct trait of opening the junctions to allow paracellular transport of antigen and good tolerability. However, the poor solubility of chitosan in neutral or alkalinized media has restricted its applications in the pharmaceutical field. Chitosan can be easily carboxymethylated to improve its solubility in aqueous media, while its biodegradability and biocompatibility are preserved. Apart from this, carboxymethyl chitosan (CMCS) can be easily processed into nanoparticles which highlight its suitability and extensive usage for preparing different drug delivery formulations. The present study deals with the development and characterization of a delivery system based on CMCS nanoparticles using ovalbumin as model protein. We demonstrated that ovalbumin loaded nanoparticles were successfully synthetized using calcium chloride as a cross-linker by ionic gelation. The nanoparticles exhibited an average size of approximately 169 nm and presented a pseudo-spherical shape. The nanoparticles size increased according to the addition of $CaCl_2$ due to the strong electrostatic attraction. During storage the nanoparticles size increased was attributed to swelling and aggregation. The loading efficiency of ovalbumin was found to be 17%. Confocal microscopy clearly showed the association between ovalbumin and CMCS chains into nanoparticles. Therefore, we suggest these nanoparticles can be considered as an attractive and promising carrier candidate for proteins and antigens. The major challenge that limits the use of such carriers is their instability in an aqueous medium. Thus, the next step of this work was to determine the robustness of several formulations using distinct freeze-drying protocols. This study demonstrated that mannitol in concentration of 10% (w/v) is well suited to preserve ovalbumin loaded CMCS nanocapsules from aggregation during lyophilization and subsequent reconstitution. Importantly, the results showed that an annealing step has a huge impact on porosity of freeze-dried cake by nearly complete crystallization of mannitol, once the crystalline matrix prevents the partial collapse and the formation of larger pores observed without annealing. Therefore, the usual observation that annealing increases the pore size due to growth of ice crystal size does not always apply, at least when crystallization of solute is involved. Since all characterizations and stability studies had been performed, the main purpose of this study was to develop a stable antigen delivery system for oral immunization using CMCS and inactivated rabies virus (RV) as the antigen. RV loaded nanoparticles was found to enhance both systemic (IgG) and local (IgA) immune responses against RV after oral delivery in mice. The effective doses 50% were 50-times higher than the negative controls, indicating that the immune response started only after the third boosting dose. Furthermore, enough neutralizing antibodies was produced to be protected against the harmful effects of the rabies virus. It is therefore concluded, that the CMCS nanoparticles formulated in this study, are suitable for oral vaccine delivery, and can be suggested as a promising delivery system for a diverse range of antigens as well as a gene/protein delivery system, especially for those positively charged. Since several approaches show that effective intervention in airway allergic inflammation can be achieved with allergen-activated interleukin-10-secreting cells, the final part of this work was dedicated to assessing whether IL-10 loaded chitosan nanoparticles (IL10-CSNPs) could be used as a possible inhalable therapeutic tool for preventing exacerbations in asthmatic patients. As positive controls, we also assess whether interleukin 17A and interleukin 9 have the ability to stimulate human airway smooth muscle (HASM) cell contractility using magnetic twisting cytometry (MTC). Significant decreased baseline cell stiffness was observed in HASM cells pre-treated with IL-10, but not with IL10-CSNPs, whereas treatment with IL-17A significantly enhanced baseline cell stiffening. Our findings reveal a previously unknown mechanism underlying immunotherapy for prevention and treatment of asthma.

**Keywords:** Nanoparticles**,** carboxymethyl chitosan, rabies virus, mucosal immunization, interleukins, cell stiffness, human airway smooth muscle cells, asthma

# TABLE OF CONTENTS

## INTRODUCTION

Vaccination has been one of the most effective approaches of preventing disease, and it is also the most cost-effective way to prevent morbidity and economic losses caused by infectious diseases [1]. More than 600 million vaccine formulations are now administered by subcutaneous or intramuscular injections, according to WHO records. Safety issues, however, like systemic and local adverse effects and possible recombination of a weakened organism into a virulent specie have increased the interest in subunit or inactivated vaccines. On the other hand, a dramatic decrease in the effectiveness of these vaccines is caused by the lack of virulence factors, generating poor immune responses in general, despite of their safety and better pharmaceutical definition [2]. Therefore, vaccine formulation may be instrumental to successful vaccination.

The oral route can be considered as one of the most comfortable ways for vaccines administration. The benefits over parenteral administration includes reduced side effects, ease of administration, and reduced risk of spread of infectious pathogens via contaminated syringes [3]. All these benefits result in better patient compliance and lower costs. However, in case of subunit or inactivated vaccines, the oral route exhibits several inadequacies due to the high acidity of stomach and the enzymatic attack in the intestinal tract [4]. Therefore, in order to obtain high immune responses via oral route, an adjuvant/delivery system is necessary to make oral immunizations more effective.

Encapsulation of the antigen into particulate carrier systems has been explored extensively in recent years and holds great promise as particles can be specifically designed to meet the challenges that oral vaccination offers. The potential of nanoparticles as vaccine delivery systems has been shown in several

studies [4, 5, 6, 7]. The advantages of this kind of system include its ability to cross biological barriers to delivery drugs or macromolecules in a controlled manner, and to prevent peptides, proteins, or genes from decomposition in biological media. Association of the vaccines with particulate systems may stimulate antigen transport to the Peyer's patches increasing the immune response after its administration via mucosal route [8].

The mucosal epithelium as well as distal mucosal surfaces of the gut associated lymphoid tissue (GALT) contains antigen specialized antigen-sampling cells known as the M cells. These cells may represent an efficient potential portal for oral vaccine delivery, due to their ability to transport antigens from the mucosal surfaces into the lymphoid tissues. After entering into the mucosal associated lymphoid tissue (MALT), the antigens are processed by antigen presenting cells such as macrophages, dendritic cells, and presented to B cells and T cells located in this tissue [9]. For mucosal immunization, chitosan, alginates and PLGA are used as delivery systems generally [4, 5, 6, 7].

Due to their biocompatibility, biodegradability and non-toxicity, natural polysaccharides are widely being studied as biomaterials for drug delivery applications [10]. Because of its low cost, biodegradability, biocompatibility, mucoadhesivity, and immuno-adjuvant properties, chitosan, the deacetylated form of chitin (poly-β-(1→4)-*N*-acetyl-*D*-glucosamin) prepared by alkaline *N*-deacetylation of chitin has a great potential to be used as a delivery system for antigens by mucosal surfaces [11, 12]. Chitosan nanoparticles has shown effective endocytotic uptake and low cytotoxicity using different cell models [13, 14].

However, limited colloidal stability, uncontrollable degradability, and the limited solubility in water or at pH higher than chitosan pKa (pH 5.5-6.5) has prevented its full exploitation in the drug delivery field, whereas chitosan derivatives offer a better solubility at neutral pH values [15, 16, 17]. The reactive hydroxyl groups in both chitin and chitosan, and amino groups in chitosan, can be used for synthetizing several derivatives. Carboxyl groups can be introduced to the hydroxyl and/or amino groups of chitosan to enhance its solubility in water at neutral pH [18]. The biological safety of carboxymethyl chitosan (CMCS) has been well established *in vitro* models, blood systems and tumor application [19, 20, 21]. Additionally, the excellent biodegradability of CMCS *in vitro* and *in vivo* has been demonstrated experimentally in rats [22]. Furthermore, the inherent absorption enhancing and mucoadhesive properties of chitosan are retained in CMCS which is extremely favorable for delivery applications. Therefore, the positive biopharmaceutical and toxicological profile of CMCS has encouraged its application in the drug delivery field [17].

The major challenge that limits the use of such carriers is their instability in an aqueous medium. Aggregation and particle fusion are frequently noticed after a long period of storage of these systems. Furthermore, polymer hydrolysis and drug leakage out of the particles can happen. Thus, the stabilization of colloidal vectors is deeply explored to reach a shelf-life of several years [23]. For stabilization of nanoparticles, freeze-drying is a commonly used process, and is considered to be an attractive way to achieve long-term stability with the advantage of easy handling [23, 24, 25]. Also termed lyophilization, freeze-drying is an industrial process of drying by freezing and sublimation of ice under vacuum

and it is used to convert solutions of labile materials into solids of sufficient stability for distribution and storage [26].

The purpose of this study was to develop a stable antigen delivery system for oral immunization using CMCS and inactivated rabies virus (RV) as the antigen. RV loaded nanoparticles was found to enhance both systemic (IgG) and local (IgA) immune responses against RV after oral delivery in mice. The effective doses 50% were 50-times higher than the negative controls, indicating that the immune response started only after the third boosting dose. Furthermore, enough neutralizing antibodies was produced to be protected against the harmful effects of the rabies virus. It is therefore concluded, that the CMCS nanoparticles formulated in this study, are suitable for oral vaccine delivery, and can be suggested as a promising delivery system for a diverse range of antigens as well as a gene/protein delivery system, especially for those positively charged

The final part of this work was dedicated to assessing whether IL-10 loaded chitosan nanoparticles (IL10-CSNPs) could prolong the half-life of IL-10 *in vitro* and be used as a possible inhalable therapeutic tool for preventing exacerbations in asthmatic patients. Patients with asthma typically experience periodic or persistent decreases in airflow from bronchospasm, and virtually all patients exhibit an exaggerated bronchoconstrictive response to exogenously administered agents such as histamine and methacholine, termed airway hyperresponsiveness (AHR). Clinically, AHR may represent the physiological outcome of an enhanced shortening of muscle fibers around the bronchial walls, which can lead to asthma exacerbations from a variety of stimuli [27].

The current view stipulates that the hyper-contractility of human airway smooth muscle (HASM) in asthma is a direct result of airway inflammation. However, the

precise nature of the immunologic phenotype and the resulting mechanical phenotype associated with disease presentation, including AHR, remain unclear.

Type-2 cytokines recruit and activate inflammatory cells, leading to airway remodeling. This remodeling is then thought to affect the structural cells in the airways, including HASM cells, contributing to bronchial obstruction. A growing body of evidence, however, supports the hypothesis that cytokines mainly those produced by TH2 cells, can also act directly on HASM cells promoting AHR to contractile agonists and attenuating HASM relaxation to β-adrenoreceptor stimulation [28, 29]. Exogenous administration of IL-13 to the lungs or overexpression of IL-13 in the lungs, for example, results in increased airway responsiveness [29]. In culture HASM cells, IL-13 increases intracellular calcium $[Ca^{2+}]_i$ induced by bradykinin, histamine and acetylcholine. IL-13 also augments leukotriene-D4 (LTD4)-induced changes in cell stiffness [30]. Strikingly, mice lacking αvβ8 integrin expressed on dendritic cells are protected from AHR as a result of impaired IL-17A signaling without changes in inflammatory cell numbers in response to sensitization and challenge with OVA demonstrating that IL-17A can contribute to AHR through its direct effects on smooth muscle, with no modulation on airway inflammation [31].

Since several approaches show that effective intervention in airway allergic inflammation can be achieved with allergen-activated interleukin-10-secreting cells, here we assessed whether interleukin 10 (IL-10) and interleukin 22 (IL-22), a member of IL-10 cytokine family, have the ability to directly affect HASM cell contractility upon histamine stimulation using magnetic twisting cytometry (MTC). We further investigate whether IL-10 loaded chitosan nanoparticles (IL-10-CSNPs) could be used as a possible inhalable therapeutic

tool for preventing exacerbations in asthmatic patients.

## REFERENCES


1. Wack A, Rappouli R. Vaccinology at the beginning of the 21st century. Curr Opin Immunol 2005;17:411–8.
2. Huang DB, Wu JJ, Tyring SK. A review of licensed viral vaccines, some of their safety concerns, and the advances in the development of investigacional viral vaccines. J Infect 2004;49:179–209.
3. Ryan EJ, Daly LM, Mills KHG. Immunomodulators and delivery systems for vaccination by mucosal routes. Trends Biotechnol 2001;19:293–304.
4. Hori M, Onishi H, Machida Y. Evaluation of Eudragit-coated chitosan microparticles as an oral immune delivery system. Int J Pharm 2005;297:223–34.
5. Kim B, Bowersock T, Griebel P, Kidane A, Babiuk LA, Sanches M, et al. Mucosal immune responses following oral immunization with rotavirus antigens encapsulated in alginate microspheres. J Control Rel 2002;85:191202.
6. van der Lubben IM, Kersten G, Fretz MM, Beuvery C, Verhoef JC, Junginger HE. Chitosan microparticles for mucosal vaccination against diphtheria: oral and nasal efficacy studies in mice. Vaccine 2003;21:1400–8.
7. Borges O, Tavares J, de Souza A, Borchard G, Junginger HE, Cordeiro-da-Silva A. Evaluation of the immune response following a short oral vaccination schedule with hepatitis B antigen encapsulated into alginate-coated chitosan nanoparticles. Eur J Pharm Sci 2007;32:278–290.

8. Borges O, Cordeiro-da-Silva A, Romeijin SG, Amidi M, de Souza A, Borchard G, Junginger HE. Uptake studies in rat Peyer's patches, cytotoxicity and release studies of alginate coated chitosan nanoparticles for mucosal vaccination. J Control Rel 2006;114:348–358.
9. Frey A, Neutra MR. Targeting of mucosal vaccines to Peyer's patch M cells. Behring Inst Mitt 1997;98:376–389.
10. Liu Z, Jiao Y, Wang Y, Zhou C, Zhang Z. Polysaccharides-based nanoparticles as drug delivery systems. Adv Drug Deliv Rev 2008;60:1650–62.
11. Vila A, Sánchez A, Janes K, Behrens I, Kissel T, Jato JLV, Alonso MJ. Low molecular weight chitosan nanoparticles as new carriers for nasal vaccine delivery in mice. European Journal of Pharmaceutics and Biopharmarmaceutics 2004;57:123–131.
12. Jiang H-L, Park I-K, Shin N-R, Kang S-G, Yoo H-S, Kim S-I, et al. In vitro study of the immune stimulating activity of an athrophic rhinitis vaccine associated to chitosan microspheres. Eur J Pharm Biopharm 2004;58:471–6.
13. Behrens I, Vila-Pena AI, Alonso MJ, Kissel T. Comparative uptake studies of bioadhesive and non-bioadhesive nanoparticles in human intestinal cell lines and rats: the effect of mucus on particle absorption and transport. Pharm Res 2002;19:1185–93.
14. Huang M, Khor E, Lim LY. Uptake and cytotoxicity of chitosan molecules and nanoparticles: effects of molecular weight and degree of deacetylation. Pharm Res 2004;21:344–53.

15. de Campos AM, Diebold Y, Carvalho EL, Sánchez A, Alonso MJ. Chitosan nanoparticles as new ocular drug delivery systems: in vitro stability, in vivo fate, and cellular toxicity. Pharm. Res. 2004;21:803–10.
16. Prego C, Paolicelli P, Díaz B, Vicente S, Sánchez A, González-Fernández A. Chitosan-based nanoparticles for improving immunization against hepatitis B infection. Vaccine 2010;28:2607–14.
17. Upadhyaya L, Singh J, Agarwal V, Tewari RP. The implications of recent advances in carboxymethyl chitosan based targeted drug delivery and tissue engineering applications. J Control Release 2014;86:54–87.
18. Upadhyaya L, Singh J, Agarwal V, Tewari RP. Biomedical applications of carboxymethyl chitosans. Carbohydr Polym 2013;91:452–66.
19. El-Sherbiny IM. Enhanced pH-responsive carrier system based on alginate and chemically modified carboxymethyl chitosan for oral delivery of protein drugs: preparation and in-vitro assessment. Carbohydr Polym 2010;80:1125–36.
20. Fu D, Han B, Dong W, Yang Z, Lv Y, Liu W. Effects of carboxymethyl chitosan on the blood system of rats. Biochem Biophys Res Commun 2011;408:110–4.
21. Zheng M, Han B, Yang Y, Liu W. Synthesis, characterization and biological safety of O-carboxymethyl chitosan used to treat Sarcoma 180 tumor. Carbohydr Polym 2011;86: 231–8.
22. Dong W, Han B, Feng Y, Song F, Chang J, Jiang H. Pharmacokinetics and bio- degradation mechanisms of a versatile carboxymethyl derivative of chitosan in rats: in vivo and in vitro evaluation. Biomacromolecules 2010;11:527–33

23. Abdelwahed W, Degobert G, Fessi H. A pilot study of freeze-drying of poly(epsilon-caprolactone) nanocapsules stabilized by poly(vinyl alcohol): formulation and process optimization. Int J Pharm 2006;309:178–188.
24. Abdelwahed W, Degobert G, Fessi H. Investigation of nanocapsules stabilization by amorphous excipients during freeze-drying and storage. Eur J Pharm Biopharm 2006;63:87–94.
25. Abdelwahed W, Degobert G, Fessi, H. Freeze-drying of nanocapsules: impact of annealing on drying process. Int J Pharm 2006;324:74–82.
26. Abdelwahed W, Degobert G, Stainmesse S, Fessi, H. Freeze-drying of nanoparticles: formulation, process and storage considerations. Adv Drug Deliv Rev 2006;58:1688–1713.
27. An SS, Bai TR, Bates JHT, et al. Airway smooth muscle dynamics: a common pathway of airway obstruction in asthma. Eur Resp J 2007;29:834–860.
28. Shore SA, Moore PE. Effects of cytokines on contractile and dilator responses of airway smooth muscle. Clin Exp Pharmacol Physiol 2002;29:859–866.
29. Renauld J-C. New insights into the role of cytokines in asthma. J Clin Pathol 2001;54:577–589.
30. S. A. Shore. Direct effects of Th2 cytokines on airway smooth muscle. Curr Opin Pharmacol 2004;4:235–240.
31. Kudo M, Melton AC, Chen C, et al. IL-17A produced by $\alpha\beta$ T cells drives airway hyperresponsiveness in mice and enhances mouse and human airway smooth muscle contraction, Nat Med 2012;18:547–554.

# CHAPTER 1

## *O-carboxymethyl chitosan nanoparticles: effect of time, stirring and cross-linker concentration on size evolution and storage stability*

## 1. INTRODUCTION

Due to biocompatibility, biodegradability and non-toxicity, natural polysaccharides are widely being studied as biomaterial for drug delivery applications. Chitosan, which is well known to be biodegradable, non-toxic, biocompatible and mucoadhesive has been exploited for the development of formulations for controlled delivery of biotherapeutics [1, 2]. Chemically, chitosan is a poly-1,4-linked $\beta$-D-glucosamine, a cationic polysaccharide prepared by alkaline N-deacetylation of chitin. However, limited colloidal stability, uncontrollable degradability, and the limited solubility in water or at pH higher than chitosan $pK_a$ (pH 5.5-6.5) has prevented its full exploitation in the drug delivery field [3, 4]. The fact that the pH of the small intestines increases from duodenum to the terminal ileum from 4.5 to 7.4 is well known. Therefore, chitosan will not be soluble in the lower part of intestine and in order to achieve higher oral bioavailability through its use as an absorption enhancing delivery system, dissolution of chitosan at the pH values in the lumen of small and large intestine is must. In this sense, derivatization of chitosan seems promising way to get rid of these limitations [5].

Among chitosan derivatives, carboxymethyl chitosan (CMCS), a water-soluble derivative, has attracted a lot of interest due to its great impact in the drug delivery area [5, 6]. In addition, CMCS a chemically versatile (COOH and $NH_2$) groups and various molecular weight (MW) is potentially biocompatible material. CMCS has provided many opportunities to the drug delivery scientists to create a lot of formulations due to its increased water solubility, high moisture retention ability, admirable biocompatibility, enhanced bacterial, antifungal and antioxidant activity, and non-toxicity as compared to chitosan [7, 8, 9, 10, 11, 12]. The

biological safety of CMCS has been well established *in vitro* models, blood systems and tumor application [13, 14, 15]. Furthermore, the excellent biodegradability of CMCS *in vitro* and *in vivo* has been demonstrated experimentally in rats [16]. The same study revealed that liver played a central role in CMCS biodegradation. Finally, the inherent excellent absorption enhancing and mucoadhesive properties of chitosan are retained in CMCS which is extremely favorable for drug delivery applications. Therefore, the positive biopharmaceutical and toxicological profile of CMCS has encouraged its application in the drug delivery field [5].

The recent advances in nanotechnology has made a significant impact on the development of drug delivery systems. Nanoscale drug delivery carriers have attracted a great deal of interest in the development of formulations that can be administered by non-invasive alternative routes such as the vaginal, nasal, and pulmonary routes [17]. Additionally, nanostructured vehicles of small size and large surface area are of particular interest for oral drug delivery because of increased absorption and penetration through the gastrointestinal tract and cellular uptake. Particulate systems should also be able to protect drugs and proteins from enzymatic degradation and modulate pharmacokinetic parameters by increasing their effectiveness. Compared to conventional formulations, delivery systems offer several advantages such as improved efficacy, reduced frequency of doses and toxicity, and convenience [18, 19, 20]. Since most of the front-line drugs are toxic compounds that act in unspecific fashion being untargeted, often eliciting unwanted and debilitating side effects, nanoscale drug delivery vehicles are capable of prolonging drug half-life, releasing drugs in a sustained or stimuli-triggered fashion, and improving solubility of hydrophobic

drugs [5]. Moreover, nanoscale particles can passively accumulate in specific tissues (e.g., tumors) through the enhanced permeability and retention (EPR) effect [21].

Polysaccharides like CMCS have emerged as a promising drug delivery nanovehicle due to its improved water solubility, biocompatibility, biodegradability, safety, biological functionality. CMCS based nanoparticles mediated vehicles have been prepared for delivery of peptides, proteins [22], antigens [23], anti-cancer [24] and anti-inflammatory drugs [25], along with poorly water-soluble drugs like triamcinolone [26] and vitamin D3 [27]. In addition to the inherent pharmacological and excellent biological properties of CMCS like unique mucoadhesivity, it has received significant attention due to the presence of active functional groups which can easily attach targeting ligants like folic acid. It can release the entrapped agents selectively at desired site in a controlled fashion [5].

The mono-*N*-carboxymethyl chitosan and trimethyl chitosan-based nanoparticles were synthetized and characterized by ionic gelation. These nanoparticles were used to investigate the higher loading efficiency of tetanus toxoid. Also, the *in vivo* studies were carried out in Balb/c mice. The mouse Balb/c monocyte macrophages that were employed for cellular uptake studies indicated that FITC-BSA loaded nanoparticles [28]. In addition to it, the higher cellular viability, loading efficacy and nasal immunization of mice with tetanus toxoid loaded nanoparticles showed that the formulation has potential for mucosal administration of vaccines. A study has demonstrated that enhanced immune response was obtained with intranasal application of nanoparticle formulations and therefore the nanoparticulate vehicle developed showed promising potential

for mucosal immunization [23]. The functionalization of nanodiamond particles with *N, O*-carboxymethyl chitosan for protein drug delivery applications has been recently demonstrated [29]. A study on the preparation of ionic cross-linked Amidase-*O*-CMCS Nps showed a sustained release of Ami which is thought to enhance the immunogenicity of Ami and in turn act as a better vaccine candidate to provide protection against *S. aureus* infections [30]. Newly, stimuli-responsive CMCS/poly (γ-glutamic acid) cross-linked with genipin was prepared and BSA was loaded onto it to demonstrate its potential in protein delivery [31].

## 2. OBJECTIVES

In this paper, we studied the formation, characterization, and stability of Ova-6-*O*-CMCS Nps to evaluate how parameters such as stirring, time, and cross-linker concentration affect nanoparticles size and stability. Ova-6-*O*-CMCS Nps were synthetized through the simple ionic gelation method. Loading efficiency of ovalbumin and size measurements of the nanoparticles were determined. Morphology and association of ovalbumin to CMCS chains into nanoparticles were also elucidated. All samples stored at room temperature presented an increase of size with formation of micrometric aggregates after 7 days. An increase of size by 24 and 32% was observed after 7 and 28 days respectively for nanoparticles stored at 4oC. Nanoparticles left without stirring took longer to reach the equilibrium with a more variable size. Thus, this study is focused on the production process reproducibility, which ultimately aims at product quality consistency.

# 3. MATERIALS AND METHODS

## 3.1. Materials

Chitosan powder with a degree of deacetylation of 80% and molecular weight of 700 kDa, ovalbumin and ovalbumin-FITC were purchased from Sigma-Aldrich (Sao Paulo, Brazil). Chloroacetic acid, acetic acid, sodium hydroxide pellets, calcium chloride and all the other chemicals used were purchased from Synth (Sao Paulo, Brazil) and were of analytical grade. The water was purified by Alpha-Q ultra-pure water system (Milipore, Ireland).

## 3.2. Chitosan carboxymethylation

The synthesis of 6-*O*-carboxymethyl chitosan (6-*O*-CMCS) was performed as previously reported [32] with minor modifications. Briefly, chitosan (3 g), NaOH 40% (23 g) and solvent (65 ml) were mixed to form slurry and allowed to swell and alkaline at 25$^{o}$C for 10 min. Then, a solution of chloroacetic acid (17.5 g) dissolved in isopropanol (20 ml) was prepared. The solution of chloroacetic acid was added slurry drop-wise at regular intervals followed by continuous stirring at 25$^{o}$C for 12 h. The reaction was stopped by adding 70% ethanol to the reaction mixture. The solution was filtered and washed with 70% ethanol four times and dehydrated with absolute alcohol. Finally, the product obtained was dialyzed for 5 days to remove impurity and freeze-dried to obtain the cotton-like product. The degree of substitution was determined based on protocol reported earlier [7, 33].

## 3.3. Freeze-drying microscopy

The collapse temperature ($T_c$) of 6-*O*-CMCS solution (3 mg/ml) was measured by a freeze-drying microscope (Linkam Scientific Instruments, Surrey,

UK) equipped by a video camera, a computer to capture the collapse image (optical window), a nitrogen cooling system, a vaccum pump and a small freeze-drying chamber with a temperature controller. Direct observation of the freeze-dried sample was done by using a polarized microscope (Nikon Elipse E600, Nikon, Japan). Samples were frozen at 2.5°C/min to -50°C and kept at this temperature during 1 min under vacuum at about 0.1 Pa. The temperature was stepwise increased 5°C or 3°C when the region of collapse approached until the collapse was observed. $T_c$ corresponds to the lowest temperature of overall loss of the initial frozen structure during freeze-drying.

### 3.4. Differential scanning calorimetry (DSC)

The thermal behavior of 6-*O*-CMCS solution (3mg/ml) was studied through differential thermal analysis using a Perkim Elmer Pyris DSC model Pyris 1 instrument (Norwallk, CT, USA) equipped with a cooling system (CryoFill, Perkim Elmer). It was calibrated using indium, mercury, and distilled water as standards. Approximately 5-10 mg of 6-*O*-CMCS solution was weighed in an aluminum pan and sealed. An empty pan was used as the reference. The solution was cooled to -50°C at 2.5°C/min and held for 1 min. It was then heated to 25°C at 10°C/min.

### 3.5. Freeze-drying cycle

The lyophilization of 6-*O*-CMCS was performed using a pilot freeze-dryer Dura-Stop MP Dura-Top MP Tray Dryer MNL-031-A (New York, USA). The 2 ml of 6-*O*-CMCS solution (3 mg/ml) were dispensed into 10 ml freeze-drying moulded vials. The conditions applied during the present study were: (1) freezing to -50°C with a temperature ramp of 2.5°C/min and holding for 30 min; (2) primary

drying performed at -30ºC for 6 h and finally (3) secondary drying was carried out at a shelf temperature of 20ºC for 4 h. To determine the end of the sublimation step, the partial pressure of water in the freeze-drying chamber was measured by a hygrometer. The chamber pressure was maintained at 10 mTorr during the drying process and a thermocouple was placed into a vial to monitor de sample temperature. At the end of the lyophilization the vials were stoppered under vacuum which is subsequently broken by injection of nitrogen gas.

### 3.6. Fourier transform infrared spectroscopy (FTIR)

The FTIR measurements of chitosan and 6-*O*-CMCS were recorded using an Alpha FTIR Spectrometer Bruker Optik GmbH (Ettlingen, Germany) by accumulation of at least 24 scans with a resolution of 4 cm-1 in the frequency range from 400-4000 $cm^{-1}$. Sample/KBr disc was formed with 2 mg/100 mg. The mixture was pressed into a 1 mm disc in a hydraulic press to obtain a pellet.

### 3.7. $^{1}$H NMR spectroscopy

For the $^{1}$H-NMR experiments 6-*O*-CMCS was dissolved in $D_2O$ at a concentration of 20 mg/ml. The $^{1}$H-NMR spectra were acquired using a Bruker Ascend 500 spectrometer (Billerica, MA, USA) at 40ºC with 65536 data points, 12 kHz spectral window, a 30º pulse, and acquisition time of 2.0 s.

### 3.8. X-ray diffraction (XRD)

X-ray diffraction of 6-*O*-CMCS was carried out using a Rigako Diffratometer model Ultima III (Tokyo, Japan). The X-ray diffraction patterns with CuKα radiation (λ = 1.54 Å) at 40 kV and 30 mA were recorded in the range of 2θ = 4-

$50^{o,}$ with steps of $0.05^{o}$ 2θ and a duration of 4 s per step.

### 3.9. Preparation of Ova-6-*O*-CMCS nanoparticles

6-*O*-CMCS nanoparticles were prepared according to a method previously reported [34] based on ionotropic gelation of 6-*O*-CMCS with $Ca^{2+}$ cations from $CaCl_2$ as a cross-linker. Ova-6-*O*-CMCS Nps were formed spontaneously upon addition of an aqueous solution of $CaCl_2$ (10 mg/ml) to a 6-*O*-CMCS solution (3 mg/ml) under magnetic stirring for 1 h at 900 rpm resulting in the formation of a turbid suspension. For association of ovalbumin with 6-*O*-CMCS nanoparticles, ovalbumin was incorporated in the $CaCl_2$ solution (132 µg/ml). Ova-6-*O*-CMCS Nps were isolated by centrifugation at 12,000 rpm at $4^{o}$C on a glycerol bed for 30 min. Supernatants were discarded and the nanoparticles were resuspended in PBS. To verify the effect of $CaCl_2$ concentration on Ova-6-*O*-CMCS Nps size, the $CaCl_2$ solution was added to a 6-*O*-CMCS solution drop wise at different 6-*O*-CMCS:$CaCl_2$ ratios under vigorous magnetic stirring at room temperature. The dynamic evolution of particle formation was investigated by monitoring particle size over time on the formulation with the best characteristics. After addition of $CaCl_2$, one set of samples was left under stirring and another was removed from the stirrer, and both were left at room temperature. Particle size was measured on freshly prepared nanoparticles, after 2, 4, 8 and 24 h from preparation.

### 3.10. Characterization of Ova-6-*O*-CMCS nanoparticles

Particle size of nanoparticles was determined by dynamic light scattering (DLS Malvern Particle analyzer, England) and nanoparticle tracking analysis (NTA NanoSight NS300, NanoSight, Amesbury, UK). The software used for

capturing and analyzing data was NTA 3.1 Build 3.1.45. Morphology of nanoparticles was determined by atomic force microscopy (NanoScope IIIA Bruker, Billerica, MA, USA). Each batch was analyzed in triplicate.

### 3.11. Loading efficacy and stability studies

The loading efficacy of the nanoparticles was calculated by an indirect way, quantifying FITC-labeled ovalbumin (Ova-FITC) that remained in solution as described before. After the synthesis of Ova-FITC-6-*O*-CMCS Nps, an aliquot of nanoparticles suspension was centrifuged at 12,000 rpm at 4$^{o}$C for 30 min and Ova-FITC in the supernatant was quantified by fluorescence spectroscopy (F-4500 Hitachi high technologies corporation, Tokyo, Japan). To eliminate background interference, the supernatant of unloaded nanoparticles was treated in the same way. The loading efficacy (LE) was determined from the following equation:

$$LE\ (\%) = \frac{\text{total amount of Ova-FITC} - \text{free Ova-FITC supernatant} \times 100}{\text{total amount of Ova-FITC}}$$

To determine the stability of the prepared Ova-6-*O*-CMCS Nps over a period of 5 weeks, the nanoparticles were stored at room temperature and at 4$^{o}$C as suspensions in PBS (7.3). Samples were taken from week 0 to 5 after preparation.

### 3.12. Confocal microscopy

Ova-FITC, 6-*O*-CMCS Nps and Ova-FITC-6-*O*-CMCS Nps were deposited

on a coverslip and observed under the microscope DMI6000 equipped with laser scanning confocal module LEICA DMI6000 (Wetzlar, Germany) equipped with the laser scanning confocal module LEICA TCS SP8. To avoid agglutination, samples were observed as liquid drops and were not dried during analysis. The laser line 488 was used for FITC detection ranging from 500 to 550 nm in PMT mode, while laser reflection images were obtained by PMT-Trans mode. The FITC labeled images were digitally processed by LEICA LAS X software and were pseudo-colored in green.

## 4. RESULTS AND DISCUSSION

### 4.1. Freeze-drying microscopy

The value of collapse temperature ($T_c$), defined as the maximum allowable product temperature during primary drying, was found to be -25$^{o}$C. Collapse and loosening of porous structure can happen when the product is heated above $T_c$ during primary drying step (Fig. 1). Therefore, the collapse during the sublimation step can prolong the reconstitution time and increase the residual humidity affecting the product quality [35, 36].

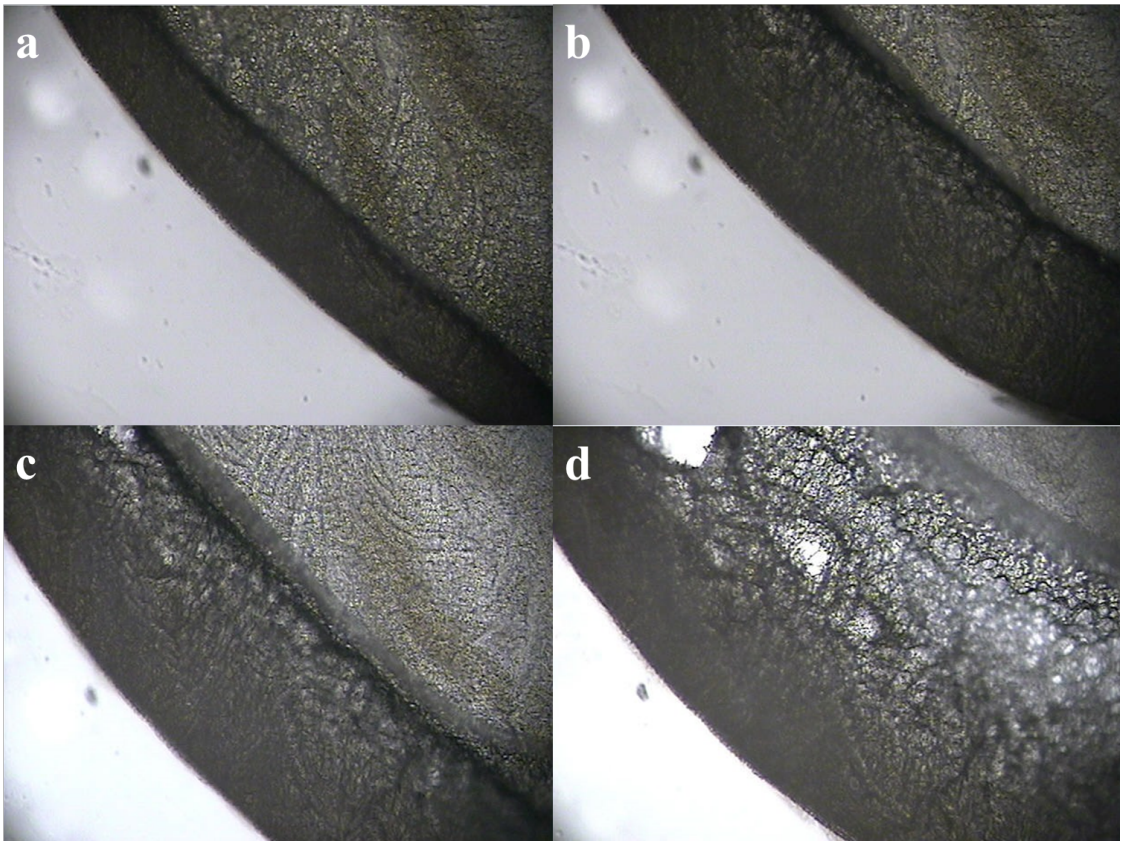


**Figure 1**. Light transmission freeze-drying microscopy of 6-*O*-CMCS. (a) Frozen and dried region (b) Micro collapse (c) Onset of overall collapse (d) overall collapse.

### 4.2. Differential scanning calorimetry

The glass transition temperature ($T_g$) obtained by DSC was found at -11ºC. The primary drying, the most time-consuming stage of the lyophilization process, should be performed at a maximum allowable temperature. This maximum allowable temperature is closely related to the physical state of the frozen system. If the solute not crystallize, the frozen product is characterized by $T_g$. For crystalline materials that forms a eutectic with ice, the maximum allowable temperature corresponds to the eutectic melting temperature, $T_e$. Primary drying above $T_g$ results in collapse of the freeze-dried matrix whereas drying above $T_e$ can lead the “melt-back” [35, 36, 37].

### 4.3. Fourier transform infrared spectroscopy (FTIR)

Fig. 2a illustrates that the main bands observed in infrared spectra of chitosan are at 3418 $cm^{-1}$ (axial stretching of O-H and N-H bond), 2870 $cm^{-1}$ (axial stretching of C-H bonds), 1590 $cm^{-1}$ (angular deformation of N-H bonds of the amino groups), 1319 $cm^{-1}$ (amide III band), 1154 $cm^{-1}$ and 1083-895 $cm^{-1}$ (glycoside bonds vibrations, C-O-C and C-O stretching) [38].

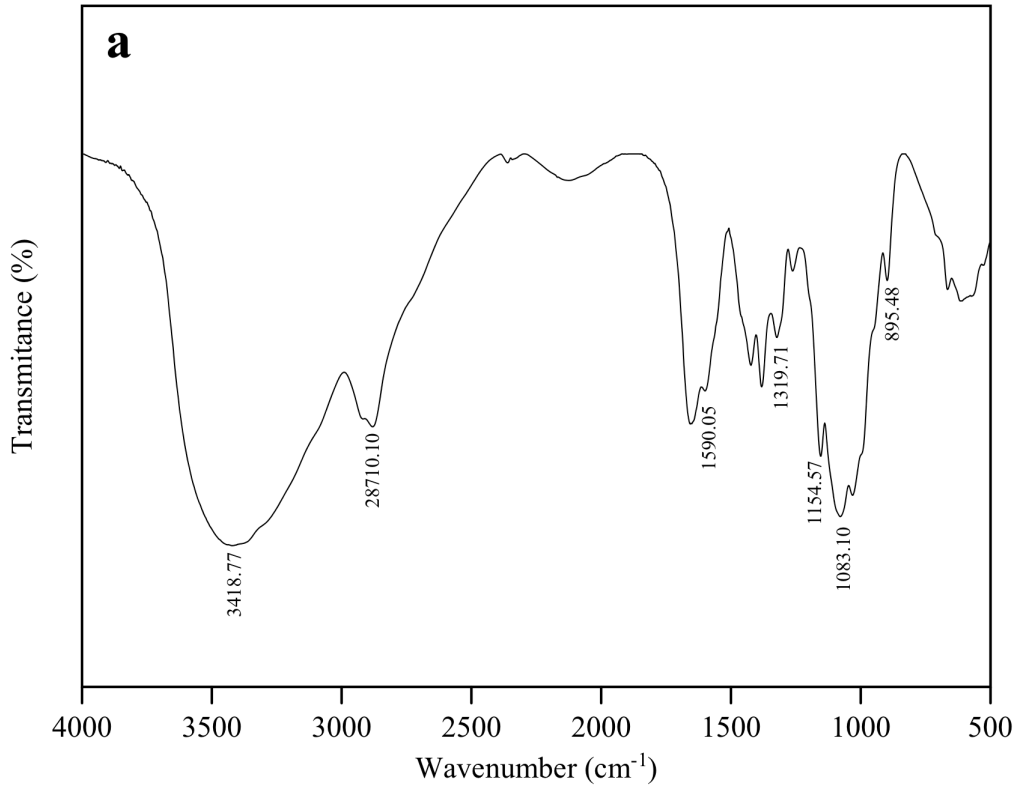


**Figure 2**. IR spectra of CS (a) and the sodium salt of 6-*O*-CMCS (b).

As shown in Fig. 2b, the presence of the assymetric and symmetrical stretching vibrations at 1594 $cm^{-1}$ and 1410 $cm^{-1}$ indicates the presence of carboxyl groups ($COO^-$), confirming that the carboxymethylation of chitosan has occurred. Moreover, the absorption peak at 1064 $cm^{-1}$ related to the stretching vibration of C-O, indicates that the carboxymethylation reaction has occurred

mainly in the C-6 position. The absorption peaks at 2921 $cm^{1}$ and 1324 $cm^{-1}$ are related to the stretching and bending vibrations of C-H, respectively. Finally, the strong broad absorption peak at 3376 $cm^{-1}$ represents the stretching vibration of O-H and N-H. All the results, in accordance with previous studies, indicates that the substitution occurred at the C-6 position [39, 40].

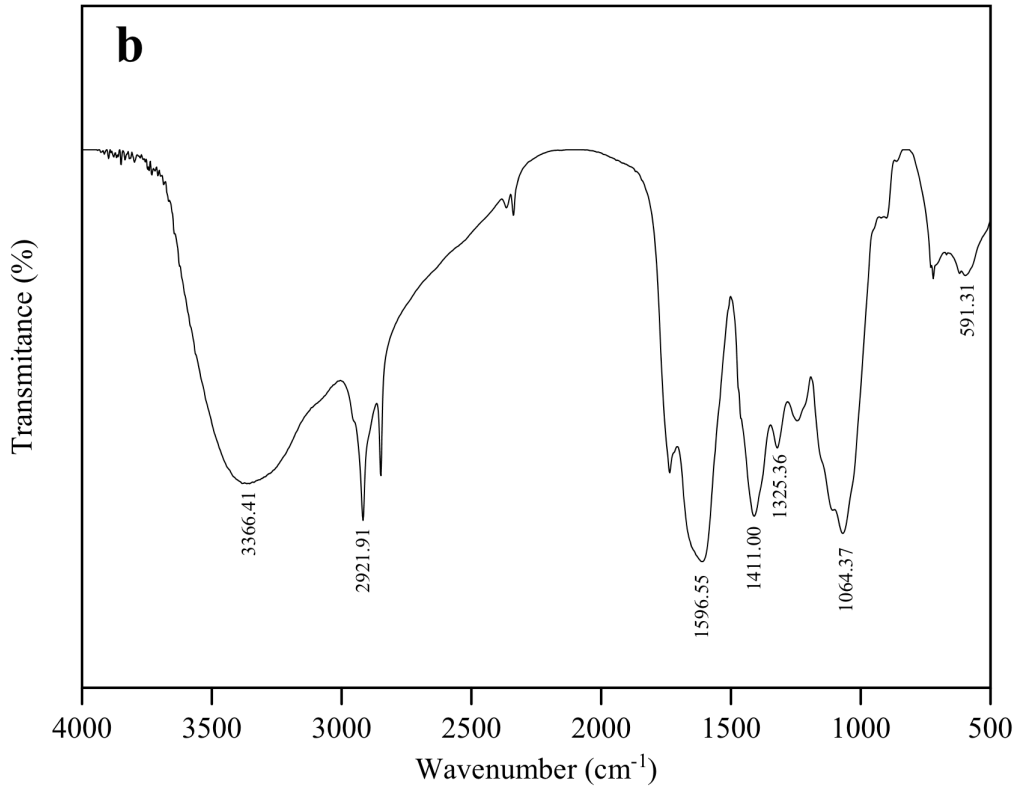


**Figure 2**. IR spectra of CS (a) and the sodium salt of 6-*O*-CMCS (b).

### 4.4. $^{1}$H NMR spectroscopy and degree of carboxymethylation

The basic assignment of $^{1}$H NMR chitosan spectra is: the resonance of H-1D (4.8 ppm), H-1A (4.6 ppm), 3-acetyl-protons (2.1 ppm), H3-H6D, H2-H6A (3.5–4.1 ppm), H-2D (3.2 ppm) [40]. The occurrence of 6-*O*-carboxymethylation in the spectra of CMCS was evidenced by the signals in the range 3.61–3.74 ppm (O-$CH_2$-COOD) (Fig. 3). The degree of carboxymethylation of the chitosan chains

was found to be 0.70. The increase in time reaction did not result in an increase of the degree of carboxymethylation. The resonance signal of the protons from N-$CH_2$-COOD group (3.25 ppm) was not found in the spectra [7].

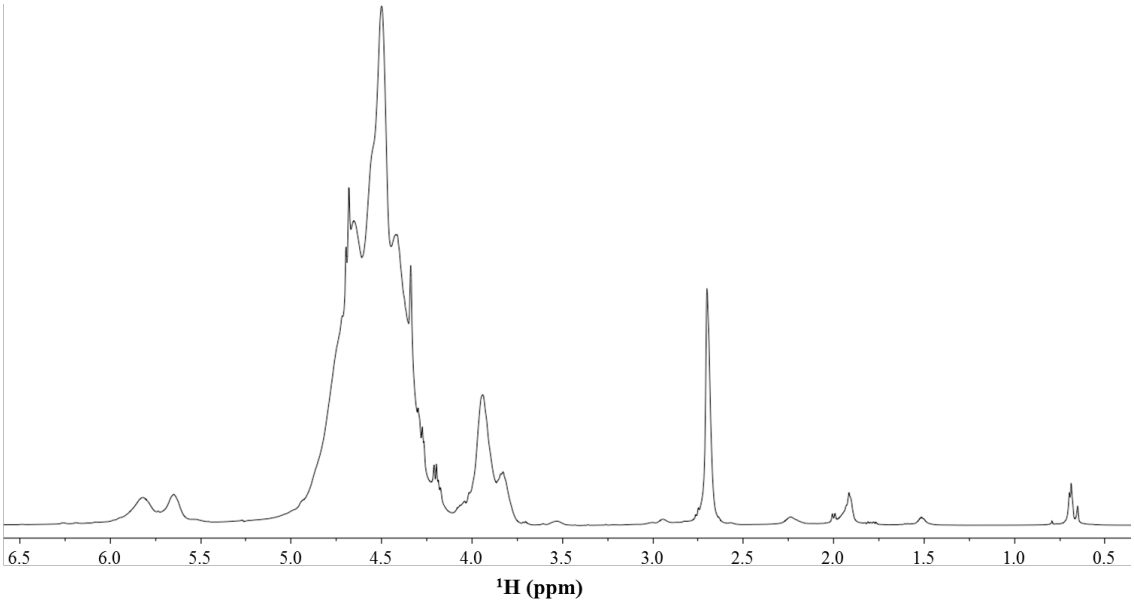


**Figure 3**. $^1$H NMR spectrum of 6-*O*-CMCS.

## 4.5. X-ray diffraction (XRD)

The comparison of the X-ray patterns of chitosan (Fig. 4a) and 6-*O*-CMCS (Fig. 4b) indicates a drastic decrease of crystallinity upon the carboxymethylation reaction. This is attributed to the presence of carboxymethyl groups which substitute de hydrogen atoms of the amino and hydroxyl groups of chitosan, affecting the establishment of hydrogen bonding involving its groups [32].

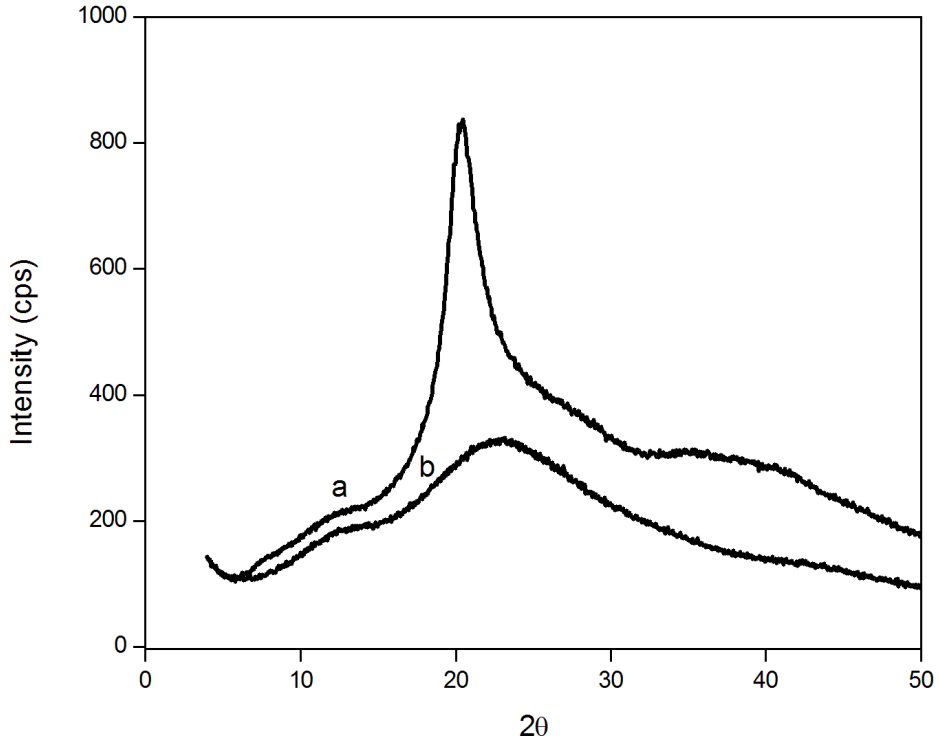


**Figure 4**. X-ray diffraction patterns of (a) chitosan and (b) 6-O-CMCS.

A previous study demonstrated that when the substitution degree was above 0.46, the peaks at 2θ = 10.4° decreased progressively and disappeared when the substitution degree was above 0.63. Finally, when the substitution degree value was higher than 1.08 carboxymethyl chitosan became amorphous [7]. These observations confirmed that carboxymethylation strongly affected the packing of the carboxymethyl chitosan chains in the solid state, resulting in a less ordered arrangement than chitosan.

### 4.6. Preparation and characterization of Ova-6-*O*-CMCS nanoparticles

Ova-6-*O*-CMCS Nps were obtained by ionic crosslinking of carboxyl groups of 6-*O*-CMCS chains and $Ca^{2+}$ cations from $CaCl_2$. DLS analysis resulted in a

size average of 169 nm and the polydispersity index was around 0.126 ± 0.020, which indicates a monodisperse distribution of the prepared nanoparticles (Fig. 5a).

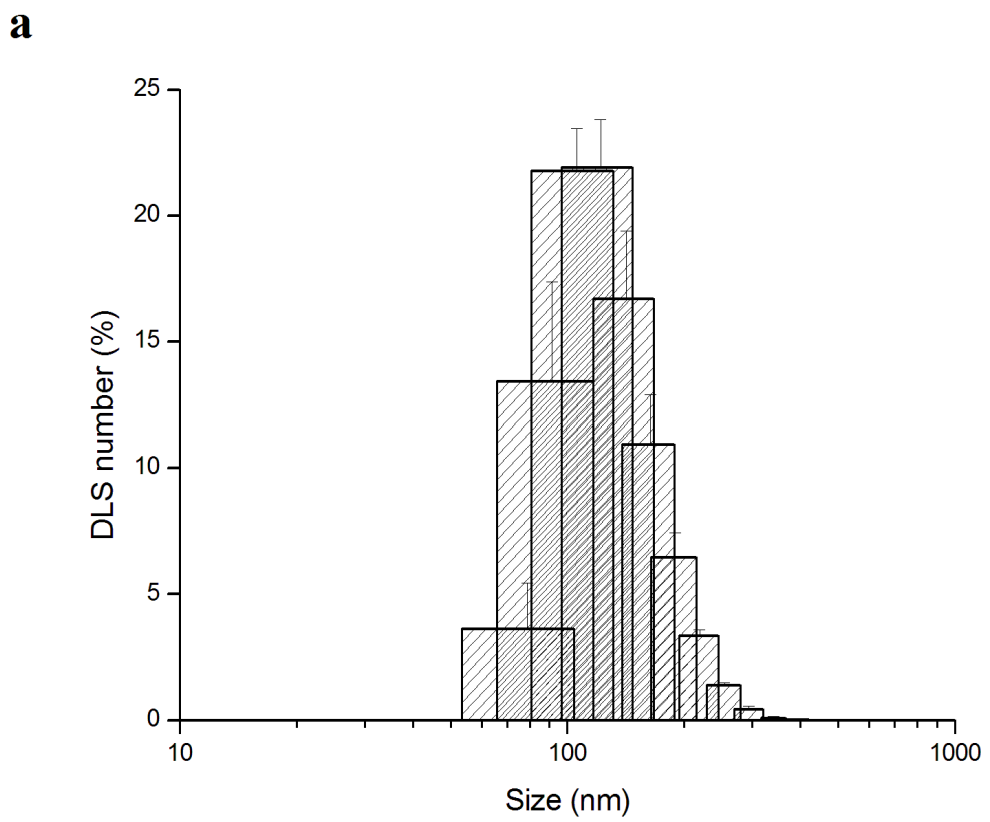


**Figure 5**. Size distribution from (a) DLS and (b) NTA of Ova-6-*O*-CMCS Nps.

The mean size and distribution of the nanoparticles were also analyzed by NTA, that enables sample visualization and provides approximate particles concentration. The mean size value obtained by NTA was 124 nm, which is about 50 nm smaller than the size average given by DLS (Fig. 5b).

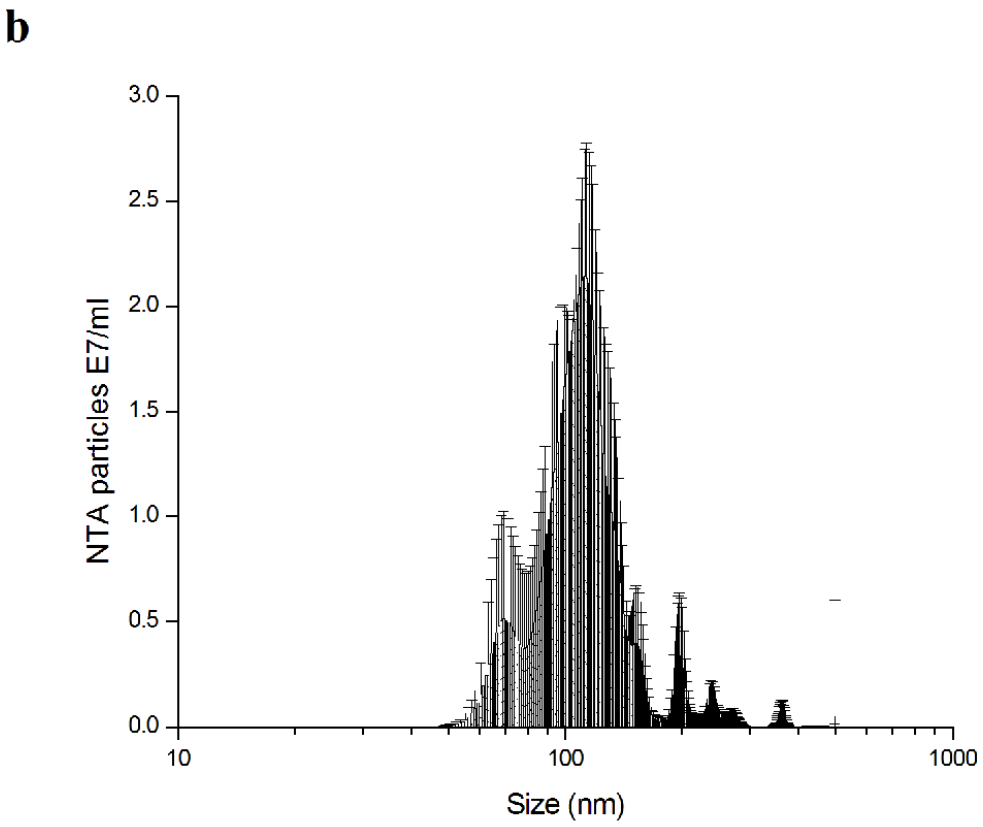


**Figure 5**. Size distribution from (a) DLS and (b) NTA of Ova-6-*O*-CMCS Nps.

Furthermore, the presence of different populations was clearly detected by sample visualization (Fig. 6).

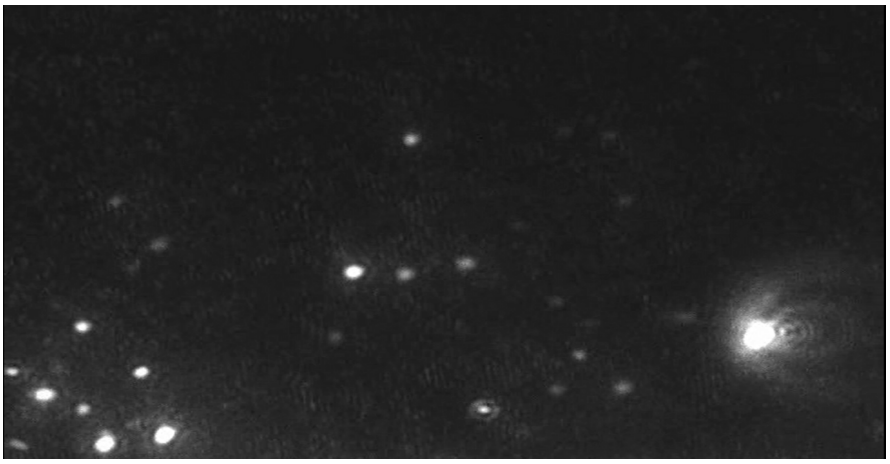

**Figure 6**. Nanoparticle tracking analysis video frame of Ova-6-*O*-CMCS Nps.

According to a previous study [52] this is related to the difficult of the DLS software to fit the data of an autocorrelation curve of a sample with has particle populations with different sizes, resulting in a single peak. Additionally, factors such as dilution, opalescence and user experience can affect the distributions of sub-micron [53, 54]. The AFM image (Fig. 7) shows that the nanoparticles have a pseudo-spherical shape.


**Figure 7**. Atomic force microscopy of Ova-6-*O*-CMCS Nps. The nanoparticles were imaged with tapping mode AFM.

Ionic crosslinking is a simple and mild procedure. In contrast to covalent crosslinking, no auxiliary molecules such as catalysts are required, which is of great interest for medical or pharmaceutical applications. The ionic crosslinking can be carried out by the classical method of preparing a crosslinked network, namely by the addition of the solubilized cross-linker to the chitosan or its derivatives solution. This method allows the formation of a homogenous network by a random crosslinking reaction [42, 43, 44].

The properties of pH-dependent chitosan or its derivatives-based drug delivery systems can be controlled by the reaction conditions during synthesis. In general, they exhibit pH-sensitive swelling and drug release by diffusion through their porous structure. However, in ionically crosslinked networks the crosslinking density is further modified by external conditions after administration, mainly by the pH of the application medium [42, 46, 47, 48]. It influences the global charge of carboxymethyl chitosan, which directly determine the crosslinking density, interactions and swelling. If the pH decreases, swelling is favored by the protonation and repulsion of carboxymethyl chitosan ammonium groups. If the pH decrease is too large, the dissociation of the ionic linkages and dissolution of the network can occur due to the protonation of carboxyl groups, leading to a fast drug release [48]. Therefore, if the crosslinking density becomes too small, interactions are no longer strong enough to avoid dissolution and the ionic cross-linker is then released [44, 50]. In addition to its pH-sensitivity, swelling is also ion-sensitive since the presence of ions weakens ionic interactions through a shielding effect, increasing swelling and delivery [42, 44, 51]. Furthermore, a decrease of the polymer chain molecular weight lowers swelling and favors dissolution [46].

Ionically crosslinked carboxymethyl chitosan networks are formed in the presence of positively charged entities, which form bridges between the negatively charged carboxymethyl chitosan chains. Therefore, ionic interactions between the positive charges of $Ca^{2+}$ and negatively charged groups $COO^-$ of carboxymethyl chitosan seems to be the dominating force involved in the formation of the nanoparticles (Fig. 8). However, additional interactions can occur inside the network, such as hydrophobic interactions, favored by the decrease of the deacetylation degree of chitosan, or interchain H-bonds due to the reduced electrostatic repulsion after neutralization of the negatively charged groups $COO^-$ of carboxymethyl chitosan by the cross-linker [42, 43, 45].

It was reported that the carboxylic groups of carboxymethyl chitosan ($pK_a$ = 3.40) are completely deprotonated in pH > 5.6 and the amount of $Ca^{2+}$ required for nanoparticles formation should be approximately constant if the interaction between $Ca^{2+}$ and carboxylic groups would be the main force towards the formation of the nanoparticles. But since the amount of $Ca^{2+}$ required for the nanoparticles increases as a function of pH, it was suggested that the interaction between $COO^-$ and $NH_3^+$ groups play an important role in the formation of nanoparticles [34]. The fraction of protonated amino groups ($pK_a$ = 7.15) decreases almost linearly between pH 7 and 8.25 and the required amount of $Ca^{2+}$ ions increases to compensate the decreasing interaction between $COO^-$ and $NH_3^+$ groups.

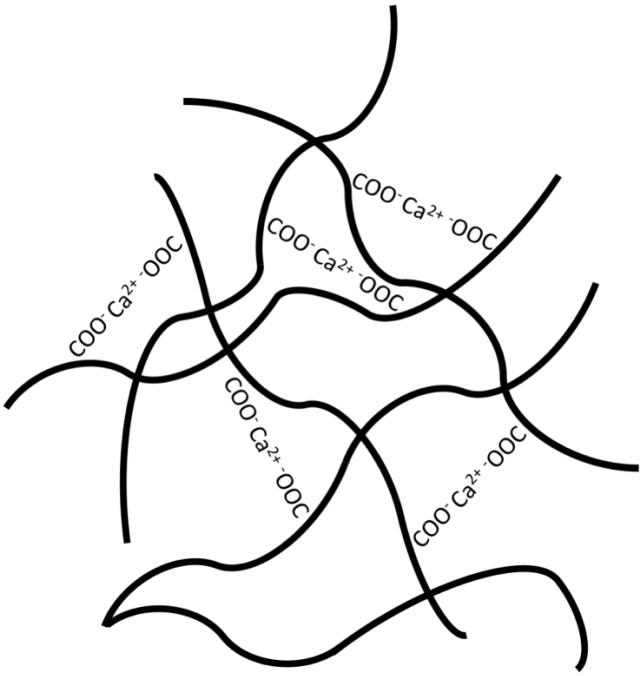


**Figure 8.** Structure of 6-*O*-CMCS Nps formed by ionic crosslinking between CMCS chains mediated by $Ca^{2+}$.

## 4.7. Ovalbumin loading

The loading efficacy of ovalbumin into 6-*O*-CMCS nanoparticles was found to be 17%. Increase in ovalbumin concentration resulted in poor encapsulation efficiency. This can be ascribed to the isoelectric point of ovalbumin (4.7), negatively charged under the preparation conditions (~pH 7). Therefore, in the aqueous neutral system, ovalbumin and 6-*O*-CMCS have the same charge, which generates an electrical repulsion between ovalbumin and 6-*O*-CMCS chains under the pH of the synthesis of nanoparticles [57], suggesting that electrostatic interactions are the main factor to form complexes between 6-*O*-CMCS and ovalbumin.

However, hydrophobic interactions could cause chain entanglement between ovalbumin and CMCS towards the formation of nanoparticles, since ovalbumin has hydrophobic residues of tyrosine, phenylalanine and tryptofan,

and CMCS has hydrophobic moieties such as glucosidic rings and acetyl groups. Moreover, the presence of hydrophilic groups such as hydroxyl and amino groups in the polypeptide backbone of ovalbumin and CMCS chains may be another important factor to drive Ova-6-*O*-CMCS Nps formation through hydrogen bonding [22].

### 4.8. Effect of cross-linker concentration, time and stirring on particle size

The size of the nanoparticles formed with different 6-*O*-CMCS:$CaCl_2$ ratios is shown in Fig. 9. Despite the rigidity of the carboxymethyl chitosan chains due to the existence of its bulky sugar rings with strong steric repulsion and potent repulsion between the $COO^-$ groups, the nanoparticles size was increased when $CaCl_2$ was introduced into the dispersion, which indicates that the adsorption of $Ca^{2+}$ to the surface of 6-*O*-CMCS chains brought the molecules into proximity and cross-linked them into nanoparticles, due to the strong electrostatic attraction provided [27].

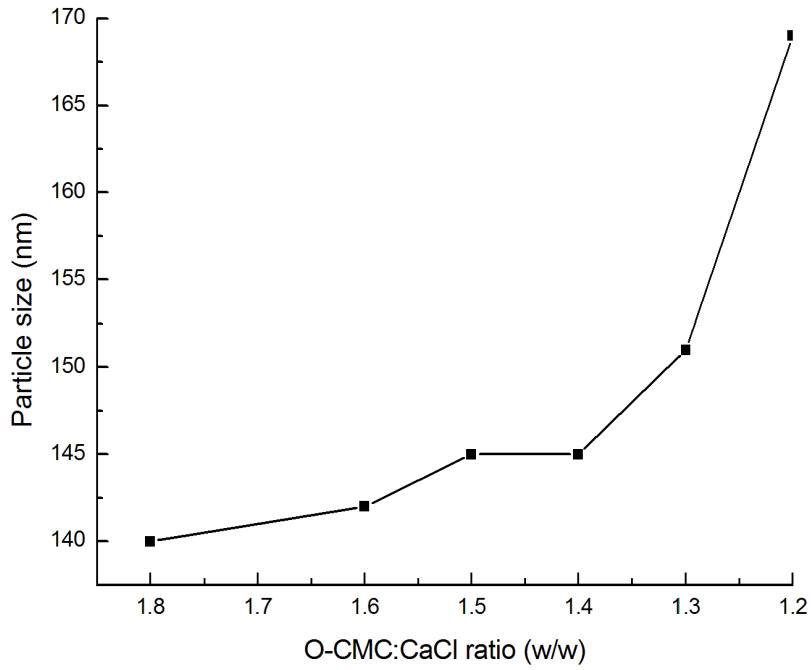


**Figure 9**. Effect of $CaCl_2$ concentration on Ova-6-*O*-CMCs Nps size. The concentration of 6-*O*-CMCS was kept constant at 3 mg/ml.

The stability of the prepared nanoparticles as a function of time is presented in Fig. 10. An increase of size with formation of micrometric aggregates was observed for all samples stored at room temperature after 7 days. It was also observed an increase of size of 24 and 32% after 7 and 28 days respectively, for nanoparticles stored at 4ºC. According to a previous study [55] the size increase during storage is ascribed to factors such as particle aggregation, free polymer molecules that interact with the particle network, swelling with nanoparticle expansion and polymer matrix fracture and syneresis. Storage conditions such as solution temperature, ionic strength and pH also may affect the storage stability. The balance between these factors is the main force regarding the size change [56, 57]. It was reported that the increased stability of CMCS nanoparticles cross-linked with $Ca^{2+}$ in near neutral pH is attributed to the

interaction between -$NH^{3+}$ and -$COO^{-}$ groups in the carboxymethyl chitosan, since the attractive interaction between these groups is stronger in near pH 7 due to the increased amount of protonated -$NH^{3+}$ groups [34].

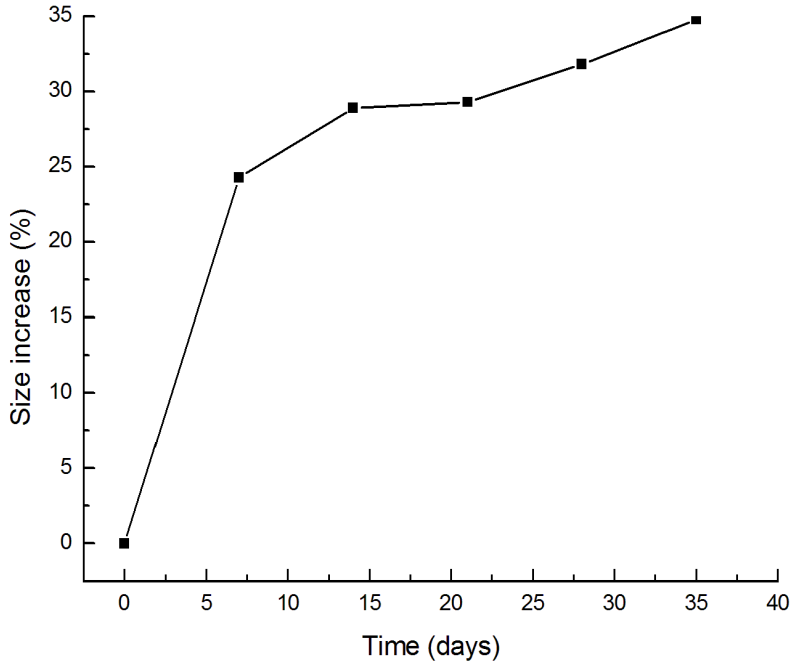


**Figure 10**. Ova-6-*O*-CMCS Nps size as a function of storage time at 4ºC. Size growth is expressed as percentage of size increase.

The changes of nanoparticles sizes are classified into instantaneous, aging, and swelling stages during storage time. While the size reduces rapidly in the instantaneous stage, during the aging the size change is insignificant while in the swelling the size increase significantly [55]. Table 1 shows the changes of mean diameter and polydispersity index of the nanoparticles kept under stirring and left without stirring. These results are similar to a previously reported study [55] and indicated that nanoparticles left without stirring take longer to reach the equilibrium and the size is more variable since the system is slowly looking for the equilibrium.

**Table 1**. Effect of time and stirring on mean diameter of Ova-6-*O*-CMCS Nps.

| Hours after preparation | Stirring | | No stirring | |
|---|---|---|---|---|
| | Size ± SD | PDI | Size ± SD | PDI |
| 0 | 147.2 ± 2.0 | 0.114 | 197.6 ± 18.3 | 0.265 |
| 2 | 150.2 ± 1.3 | 0.115 | 196.8 ± 17.1 | 0.241 |
| 4 | 150.1 ± 0.9 | 0.118 | 199.3 ± 17.9 | 0.248 |
| 8 | 151.2 ± 1.5 | 0.101 | 197.4 ± 15.7 | 0.228 |
| 24 | 155.6 ± 2.2 | 0.109 | 198.6 ± 13.7 | 0.216 |

Additionally, as reported previously [58], nanoparticles prepared with chitosan of high molecular weight have more intermolecular entanglements and consequently the size change of the particles takes longer.

It is worth mentioning that despite of numerous reports on delivery of ovalbumin, such as trimethyl chitosan-ovalbumin conjugate [59], ovalbumin loaded N-trimethyl chitosan nanoparticles [60], ovalbumin chitosan nanoparticles [61], and carboxymethyl starch and chitosan polyelectrolyte complex as an excipient for administration ovalbumin [62], in none of them the *O*-carboxymethylated derivative of chitosan as nanoparticles is used for the delivery of ovalbumin. Importantly, according to our knowledge, little is known about the storage stability of these nanoparticles and how parameters such as stirring, time, and cross-linker concentration affect nanoparticles size. In this paper, we studied the formation, characterization, and stability of *O*-carboxymethyl chitosan nanoparticles as a function of $Ca^{2+}$ concentration, time, and stirring, since all these aspects are aimed at one target: production process reproducibility and product quality consistency.

### 4.9. Confocal microscopy

Fig. 11 shows fluorescently labeled 6-*O*-CMCS nanoparticles after Ova-

FITC loading (Ova-FITC-6-*O*-CMCS Nps), Ova-FITC and unloaded 6-*O*-CMCS nanoparticles (6-*O*-CMCS Nps). The FITC fluorescent labeling was detected in Ova-FITC-6-*O*-CMCS Nps following the structural morphology of 6-*O*-CMCS Nps, while unlabeled 6-*O*-CMCS Nps did not show any fluorescence signal. As expected, the unloaded nanoparticles were imaged only by detection of the laser reflection and no FITC signal was detected. Ova-FITC samples generated only a diffuse fluorescent signal. Because ovalbumin has dimensions of 7.0 nm x 3.6 nm x 3.0 nm [63] and one single labeled molecule detection is under the resolution limits of this equipment, the identification of a diffuse signal indicated that high amounts of Ova-FITC were freely dispersed in the sample drop. When compared to the Ova-FITC-6-*O*-CMCS Nps, the FITC labeling were clearly concentrated and associated to the nanoparticles while Ova-FITC free samples did not present any organization or concentrated signal suggesting that Ova-FITC molecules were indeed associated to the nanoparticles. Due to resolution limits, it was not possible to evaluate whether the Ova-FITC was inside or bordering the nanoparticles.

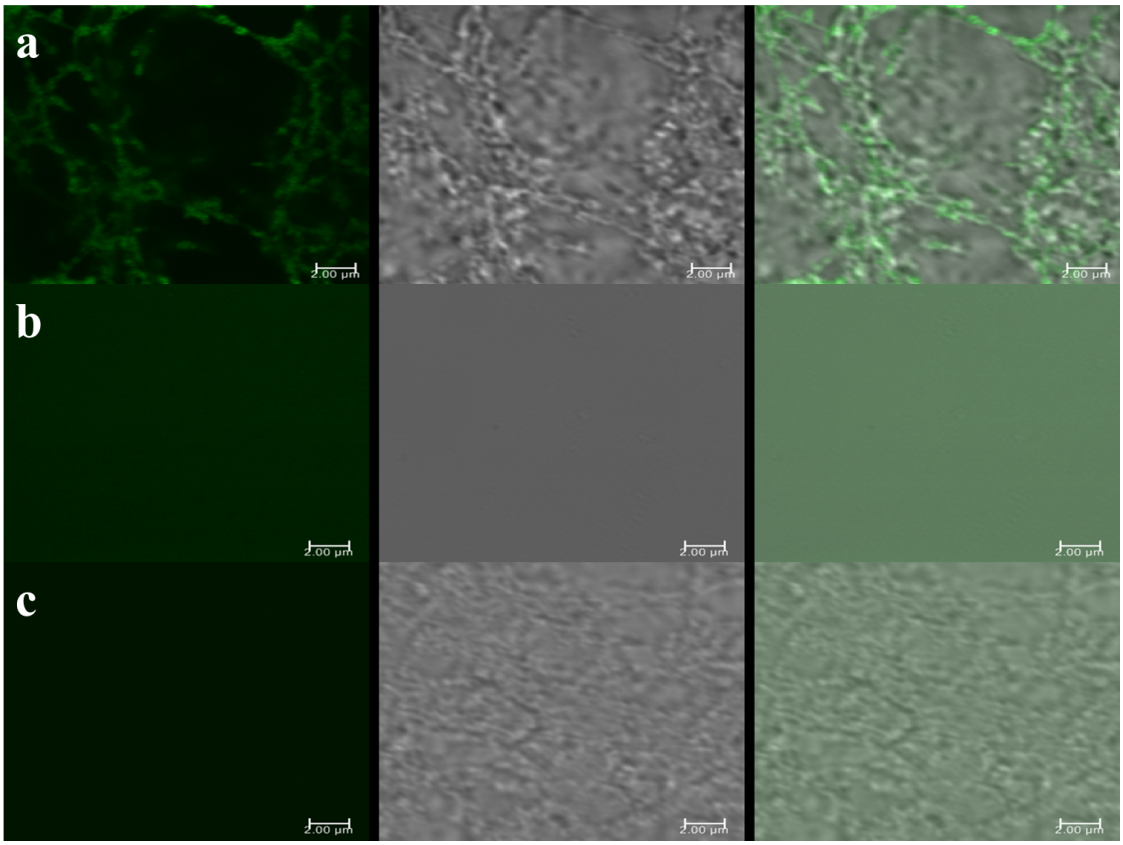


**Figure 11**. Confocal laser scanning microscopy of (a) Ova-FITC-6-*O*-CMCS Nps, (b) Ova-FITC, (c) 6-*O*-CMCS Nps. Left column shows the images obtained under detection of the FITC signal (green), middle column shows images of the laser reflection mode and right column shows the merged images from right and middle column.

## 5. CONCLUSION

Ovalbumin loaded 6-*O*-CMCS nanoparticles were successfully synthetized using a carboxymethylated derivative of chitosan and $Ca^{2+}$ as a cross-linker by ionic gelation. The nanoparticles exhibited an average size of approximately 169 nm and presented a pseudo-spherical shape. The presence of different populations was clearly detected by sample visualization through NTA analysis. The loading efficiency of ovalbumin was found to be 17% and it was attributed to its negative charge under the preparation conditions (~pH 7).

Confocal microscopy studies clearly showed the association between ovalbumin and CMCS chains into nanoparticles. Importantly, the nanoparticles size increased according to the addition of calcium chloride due to the strong electrostatic attraction. During storage the nanoparticles size increased was attributed to aggregation, free polymer molecules interaction with the particle network, swelling with nanoparticle expansion, polymer matrix fracture and syneresis. In addition, nanoparticles left without stirring took longer to reach the equilibrium with a more variable size. Moreover, because nanoparticles prepared with high molecular weight chitosan have more intermolecular entanglements, the size change of the particles takes longer. Thus, this study not only provides detailed information regarding the formation and characterization of Ova-6-*O*-CMCS Nps, but also focuses on the production process reproducibility through all the stability experiments performed, which ultimately aims at product quality consistency. Therefore, we suggest that *O*-CMCS nanoparticles can be considered as an attractive and promising carrier candidate for peptides, proteins, and antigens. At this moment, we are carrying out in vivo experiments using rabies virus loaded carboxymethyl chitosan nanoparticles. It is expected from animal models that the CMCS-based delivery system can be able to provide controlled release, improved efficacy and high/long-lasting mucosal and humoral immune responses to the antigen.

## 6. REFERENCES

1. Casettari L, Vllasaliu D, Castagnino, E, Stolnik S, Howdle S, Illum L. PEGylated chitosan derivatives: synthesis, characterizations and pharmaceutical applications. *Prog Polym Sci.* 2012;37:659–685.

2. Mishra D, Bhunia B, Banerjee I, Datta P, Dhara S, Maiti TK. Enzymatically crosslinked carboxymethyl-chitosan/gelatin/nano-hydroxyapatite injectable gels for in situ bone tissue engineering application. *Mater Sci Eng C.* 2011;31:1295–1304.
3. De Campos AM, Diebold Y, Carvalho EL, Sánchez A, Alonso MJ. Chitosan nanoparticles as new ocular drug delivery systems: in vitro stability, in vivo fate, and cellular toxicity. *Pharm Res.* 2004;21:803–810.
4. Prego C, Paolicelli P, Díaz B, Vicente S, Sánchez A, González-Fernández A. Chitosan-based nanoparticles for improving immunization against hepatitis B infection. *Vaccine*. 2010;28:2607–2614.
5. Upadhyaya L, Singh J, Agarwal V, Tewari RP. The implications of recent advances in carboxymethyl chitosan based targeted drug delivery and tissue engineering applications. *J Control Release.* 2014;86:54–87.
6. Upadhyaya L, Singh J, Agarwal V, Tewari RP. Biomedical applications of carboxymethyl chitosans. *Carbohydr Polym.* 2013;91:452–466.
7. Chen XG, Park HJ. Chemical characteristics of *O*-carboxymethyl chitosans related to the preparation conditions. *Carbohydr Polym.* 2003;53:355–359.
8. Chen SC, Wu YC, Mi FL, Lin YH, Yu LC, Sung HW. A novel pH-sensitive hydrogel composed of *N,O*-carboxymethyl chitosan and alginate cross-linked by genipin for protein drug delivery. *J Control Release.* 2004;6:285–300.
9. Singh J, Dutta PK. Preparation, circular dichroism induced helical conformation and optical property of chitosan acid salt complexes for biomedical applications. *Int J Biol Macromol.* 2009;45:384–392.

10. Zhao D, Huang J, Hu S, Mao J, Mei L. Biochemical activities of *N,O*-carboxymethyl chitosan from squid cartilage. *Carbohydr Polym.* 2011;85:832–837.
11. Liu XF, Guan YL, Yang DZ, Li Z, Yao DY. Antibacterial action of chitosan and carboxymethylated chitosan. *J Appl Polym Sci.* 2001;79:1324–1335.
12. Seyfarth F, Schliemann S, Elsner P, Hipler UC. Antifungal effect of high- and low-molecular-weight chitosan hydrochloride, carboxymethyl chitosan, chitosan oligosaccharide and *N*-acetyl-D-glucosamine against Candida albicans, Candida krusei and Candida glabrata. *Int J Pharm.* 2008;352:139–148.
13. El-Sherbiny IM. Enhanced pH-responsive carrier system based on alginate and chemically modified carboxymethyl chitosan for oral delivery of protein drugs: preparation and in-vitro assessment. *Carbohydr Polym.* 2010;80:1125–1136.
14. Fu D, Han B, Dong W, Yang Z, Lv Y, Liu W. Effects of carboxymethyl chitosan on the blood system of rats. *Biochem Biophys Res Commun.* 2011;408:110–114.
15. Zheng M, Han B, Yang Y, Liu W. Synthesis, characterization and biological safety of *O*-carboxymethyl chitosan used to treat Sarcoma 180 tumor. *Carbohydr Polym.* 2011;86:231–238.
16. Dong W, Han B, Feng Y, Song F, Chang J, Jiang H. Pharmacokinetics and biodegradation mechanisms of a versatile carboxymethyl derivative of chitosan in rats: in vivo and in vitro evaluation. *Biomacromolecules.* 2010;11:527–1533.

17. Andrews GP, Laverty TP, Jones, SD. Mucoadhesive polymeric platforms for controlled drug delivery. *Eur J Pharm Biopharm* 2009;71:505–518.
18. Des Rieux A, Fievez V, Garinot M, Schneider YJ, Préat V. Nanoparticles as potential oral delivery systems of proteins and vaccines: a mechanistic approach. *J Control Release.* 2006;116:1–27.
19. Prego C, Garcia M, Torres D, Alonso MJ. Transmucosal macromolecular drug delivery. *J Control Release.* 2005;101:151–162.
20. Zhang L, Gu FX, Chan JM, Wang AZ, Langer RS, Farokhzad OC. Nanoparticles in medicine: therapeutic applications and developments. *Clin Pharmacol Ther.* 2008;83:761–769.
21. Torchilin V. Tumor delivery of macromolecular drugs based on the EPR effect. *Adv Drug Deliv Rev.* 2011;63:131–135.
22. Wu H, Zhu A, Yuan L. Interactions between *O*-carboxymethylchitosan and bovine serum albumin. *Mater Chem Phys.* 2008;112:41–46.
23. Sayın B, Somavarapu S, Li XW, Sesardic D, Senel S, Alpar OH. TMC–MCC (*N*-trimethyl chitosan–mono-*N*-carboxymethyl chitosan) nanocomplexes for mucosal delivery of vaccines. *Eur J Pharm Sci.* 2009;38:362–369.
24. Upadhyaya L, Singh J, Agarwal V, Pandey AC, Verma SP, Das P, Tewari RP. Efficient water soluble nanostructured ZnO grafted O-carboxymethyl chitosan/curcumin-nanocomposite for cancer therapy. *Process Biochem.* 2015;50:678–688.
25. D'Agostini-Junior O. Petkowicz CL, Couto AG, De Andrade SF, Freitas RA. Simultaneous in situ monitoring of acrylic acid polymerization reaction on *N*-carboxymethyl chitosan using multidetectors: formation of a new bioadhesive and gastroprotective hybrid particle. *Mater Sci Eng C.* 2011;31:677–682.

26. Rosa TRO, Debrassi A, Silva RML, Bressan C, Freitas RA, Rodrigues CA. Synthesis of *N*-benzyl-*O*-carboxymethyl chitosan and application in the solubilization enhancement of a poorly water-soluble drug (triamcinolone). *J Appl Polym Sci.* 2012;24:4206–4212.
27. Luo Y, Teng Z, Wang Q. Carboxymethyl chitosan-soy protein complex nanoparticles for the encapsulation and controlled release of vitamin D3. *Food Chem.* 2013;141:524–532.
28. Sayın B, Somavarapu S, Li XW, Thanou M, Sesardi D, Alpar HO, Senel S. Mono-*N*-carboxymethyl chitosan (MCC) and *N*-trimethyl chitosan (TMC) nanoparticles for non-invasive vaccine delivery. *Int J Pharm.* 2008;363:139–148.
29. Wang HD, Yang Q, Niu CH. Functionalization of nanodiamond particles with *N,O*-carboxymethyl chitosan. *Diam Relat Mat.* 2010;19:441–444.
30. Smitha KT, Sreelakshmi M, Nisha N, Jayakumar R, Biswas R. Amidase encapsulated *O*-carboxymethyl chitosan nanoparticles for vaccine delivery. *Int J Biol Macromol.* 2014;63:154–157.
31. Yu SH, Wu SJ, Tang DW, Ho YC, Mi FL, Kuo TH. Stimuli-responsive materials prepared from carboxymethyl chitosan and poly(l-glutamic acid) for protein delivery. *Carbohydr Polym.* 2012;87:531–536.
32. Abreu FR, Campana-Filho SP. Characteristics and properties of carboxymethylchitosan. *Carbohydr Polym.* 2009;75:214–221.
33. Ragnhild JN, Hjerde KM, Varum H. Grasdalen, S. Tokura, O. Smidsrod Chemical composition of *O*-(carboxymethyl)-chitins in relation to lysozyme degradation rates. *Carbohydr Polym.* 1997;34:131–139.

34. Kalliola S, Repo E, Srivastava V, Heiskanen JP, Sirvio JÁ, Liimatainen H, Sillanpaa M. The pH sensitive properties of carboxymethyl chitosan nanoparticles cross-linked with calcium ions. *Colloids Surf B Biointerfaces.* 2017;153:229–236.
35. Abdelwahed W, Degobert G, Fessi H. Investigational of nanoparticles stabilization by amorphous excipients during freeze-drying and storage. *Eur J Pharm Biopharm.* 2006;63:87–94.
36. Pyne A, Surana R, Suryanarayanan R. Crystallization of manitol below Tg' during freeze-drying in binary and ternary aqueous systems. *Pharm Res.* 2002;19:900–908.
37. Passot S, Fonseca F, Alarcon-Lorca M, Rolland D, Marin M. Physical characterization of formulations for the development of two stable freeze-dried proteins during both dried and liquid storage. *Eur J Pharm Biopharm.* 2005;60:335–348.
38. Ge H-C, Luo D-K. Preparation of carboxymethyl chitosan in aqueous solution under microwave irradiation. *Carbohydr Res.* 2005;340:1351–1356.
39. Xie W, Xu P, Wang W, Liu Q. Preparation and antibacterial activity of a water-soluble chitosan derivative. *Carbohydr Polym.* 2002;50:35–40.
40. Jiang Z, Han B, Li H, Yang Y, Liu W. Preparation of carboxymethyl chitosan in aqueous solution under microwave irradiation. *Carbohydr Polym.* 2015;129:1–8.
41. Weinghold MX, Sauvageau JCM, Keddig N, Matzke M, Tartsch B, Grunwald I, Kübel C, Jastorff B, Thöming J. Strategy to improve the characterization of chitosan for sustainable biomedical applications: SAR guided multi-dimensional analysis. *Green Chem.* 2009;11:498–509.

42. Shu XZ, Zhu KJ, Song W. Novel pH-sensitive citrate cross-linked chitosan film for drug-controlled release. *Int J Pharm.* 2001;212:19–28.

43. Ruel-Gariépy E, Chenite A, Chaput C, Guirguis S, Leroux J-C. Characterization of thermosensitive chitosan gels for the sustained delivery of drugs. *Int J Pharm.* 200;203:89–98.

44. Draget KI, Varum KM, Moen E, Gynnild H, Smidsrod O. Chitosan cross-linked with Mo (VI) polyoxyanions: a new gelling system. *Biomaterials.* 1992;3:635–638.

45. Brack HP, Tirmizi SA, Risen WMA. A spectroscopic and viscosimetric study of the metal ion-induced gelation of the biopolymer chitosan. *Polymer.* 1997;38:2351–2362.

46. Mi FL, Shyu SS, Wong TB, Jang SF, Lee ST, Lu KT. Chitosan polyelectrolyte complexation for the preparation of gel beads and controlled release of anticancer drug. II. Effect of pH- dependent ionic crosslinking or interpolymer complex using tripolyphosphate or polyphosphate as reagent. *J Appl Polym Sci.* 1999;74:1093–1107.

47. Kubota N, Kikuchi Y. Preparation and properties of macromolecular complexes consisting of chitosan derivatives and potassium metaphosphate. *Makromol Chem.* 1992:193:559–566.

48. Vazquez B, Gurruchaga M, Goni I. Hydrogels based on graft copolymerization of HEMA/BMA mixtures onto soluble gelatin: swelling behavior. *Polymer.* 1995;36:2311–2314.

49. Berger J, Reist M, Mayer JM, Felt O, Peppas NA, Gurny R. Structure and interactions in covalently and ionically crosslinked chitosan hydrogels for biomedical applications. *Eur J Pharm Biopharm.* 2004;57:19–34.

50. Mi FL, Chen CT, Tseng YC, Kuan CY, Shyu SS. Iron(III)-carboxymethylchitin microsphere for the pH-sensitive release of 6-mercaptopurine. *J Control Release.* 1997;44:19–32.
51. Shu XZ, Zhu KJ. Controlled drug release properties of ionically cross-linked chitosan beads: the influence of anion structure. *Int J Pharm.* 2002;233:217–225.
52. Filipe V, Hawe A, Jiskoot W. Critical evaluation of nanoparticle tracking analysis (NTA) by Nanosight for the measurement of nanoparticles and protein aggregates. *Pharm Res.* 2010;27:796–810.
53. Gruia F, Parupudi A, Polozova A. Practical considerations for detection and characterization of sub-micron particles in protein solutions by nanoparticle tracking analysis. *PDA J Pharm Sci Technol.* 2016;69:427–439.
54. Gross J, Sayle S, Karow AR, Bakowsky U, Garidel P. Nanoparticle tracking analysis of particle size and concentration detection in suspensions of polymer and protein samples: influence of experimental and data evaluation parameters. *Eur J Pharm Biopharm.* 2016;104:30–41.
55. Tsai M-L, Chen R-H, Bai S-W, Chen W-Y. The storage stability of chitosan/tripolyphosphate nanoparticles in a phosphate buffer. *Carbohydr Polym.* 2001;84:756–761.
56. López-León T, Carvalho ELS, Seijo B, Ortega-Vinuesa JL, Bastos-González D. Physicochemical characterization of chitosan nanoparticles: electrokinetic and stability behavior. *J Colloid Interface Sci.* 2005;283:344–351.
57. Tang ESK, Huang M, Lim LY. Ultrasonication of chitosan and chitosan nanoparticles. *Int J Pharm.* 2003;265:103–114.

58. Rampino A, Borgogna M, Blasi P, Bellich B, Cesàro A. Chitosan nanoparticles: preparation, size evolution and stability. *Int J Pharm.* 2013;455:219–228.

59. Slutter B, Soema PC, Ding Z, Verheul R, Hennink W, Jiskoot W. Conjugation of ovalbumin to trimethyl chitosan improves immunogenicity of the antigen. *J Contr Rel*. 2010;143:207–214

60. Slutter B, Jiskoot W. Dual role of CpG as immune modulator and physical crosslinker in ovalbumin loaded *N*-trimethyl chitosan (TMC) nanoparticles for nasal vaccination. *J Contr Rel*. 2010;148:117–121.

61. Wen Z-S, Xu Y-L, Zou X-T, Xu Z-R. Chitosan nanoparticles act as an adjuvant to promote both Th1 and Th2 immune responses induced by ovalbumin in mice. *Mar Drugs*. 2011;9:1038–1055.

62. Assaad E, Blemur L, Lessard M, Mateescu MA. Polyelectrolyte complex of carboxymethyl starch and chitosan as protein carrier: oral administration of ovalbumin. *J Biomater Sci*. 2012;23:1713–1728.

63. Erickson HP. Size and shape of protein molecules at the nanometer level determined by sedimentation, gel filtration, and electron microscopy. *Biol Proced* Oline. 2009;11:32–51.

# CHAPTER 2

# Freeze-Drying of Ovalbumin Loaded Carboxymethyl Chitosan Nanocapsules: Impact of Freezing and Annealing Procedures on Physico-Chemical Properties of the Formulation During Dried Storage

## 1. INTRODUCTION

Nanometric colloidal vectors have gained a considerable interest in the last few years because of their ability to ensure a specific drug targeting [1,2]. Among these carriers, liposomes and nanoparticles have special advantages with regard to the modulation of an active ingredient distribution within the human body [3].

Nanoparticles are solid colloidal drug delivery systems in a size range between 10 and 1000 nm. Nanoparticles can be classified into nanospheres and nanocapsules. Nanocapsules are vesicular systems in which the drug is confined to an aqueous or oily cavity surrounded by a polymeric layer while nanospheres are matrix systems in which the drug is physically and uniformly dispersed [3]. For the preparation of nanoparticles, different macromolecular materials such as synthetic or natural polymers can be used.

Polymeric nanoparticles have received increasing attention in pharmaceutical applications for the development of many different colloidal vehicles for colon or mucosal delivery of vaccines and proteins [4–8].

The advantages of this kind of system include its capacity to cross biological barriers, to delivery drugs or macromolecules in a controlled manner, and to prevent peptides, proteins, oligonucleotides, and genes from decomposition in biological media [9]. Association of the vaccines with particulate systems may stimulate the antigen transport to the Peyer's patches and increasing immune response after its administration through mucosal route [10,11,12]. The potential of nanoparticles as a vaccine delivery system has been shown in various studies [4–7].

Although a wide range of materials such as synthetic polymers, surfactants, and lipids, have been used to prepare nanocarriers, polysaccharides have

attracted great attention due to their impressive biological and physical properties [12]. Because of its low cost, biodegradability, biocompatibility, high mucoadhesive, and immuno- adjuvant properties, chitosan, the deacetylated form of chitin (poly-β-(1 → 4)-*N*-acetyl-D-glucosamin) has been used as a carrier for protein delivery by mucosal surfaces [5,8]. Chitosan nanoparticles has shown effective endocytotic uptake and low cytotoxicity through different cell culture models [13,14]. Due to similar properties, promising antigen delivery systems based on chitosan derivatives have also been reported [6,7].

The major challenge that limits the use of such carriers is their instability in an aqueous medium. Aggregation and particle fusion are frequently noticed after a long period of storage of these systems. Furthermore, polymer hydrolysis and drug leakage out of the nanocapsules can happen. Thus, the stabilization of colloidal vectors is deeply explored to reach a shelf-life of several years [15].

For stabilization of nanoparticles, freeze-drying is a commonly used process, and is considered to be an attractive way to achieve long-term storage stability with the advantage of easy handling [15–17]. Also termed lyophilization, freeze-drying is an industrial process of drying by freezing and sublimation of ice under vacuum and it is used to convert solutions of labile materials into solids of sufficient stability for distribution and storage [18].

During the freezing, the first step of lyophilization, the liquid suspension is cooled, and ice of water are formed. Throughout the freezing process more water contained in the liquid phase freezes. The freezing is considered the most aggressive and stressful step of freeze-drying, because this step may cause destruction or aggregation of the nanocapsules [18].

An annealing step is often introduced into the freezing protocol to allow larger ice crystals to grow at the expense of small ones in a process denoted as “Ostwald ripening.” Larger ice crystals leave larger pores, thereby allowing water vapor to flow through the sample easier. Annealing is an isothermal step in which samples are maintained at a specific temperature above the glass transition temperature for a period of time. This thermal treatment has dramatic effects on the size of ice crystals and therefore on the primary drying by increasing pores diameter in the freeze-dried matrix which were occupied by ice crystals before the sublimation step [17]. Annealing procedure is also used to facilitate the crystallization of bulking agents, such as mannitol and glycine [19].

However, there is so far no systematic study about freeze-drying of carboxymethyl chitosan-based nanocapsules. Therefore, the goal of the present study was to investigate the factors which can influence the carboxymethyl chitosan-based nanocapsules stability using different freeze-drying protocols and to analyze the influence of various excipients on the freeze-drying process as well as on the short-term storage of the freeze-dried formulations. The storage of lyophilized formulations was performed at both refrigerated as well as room temperature.

During the lyophilization suitable excipients are required to ensure adequate tonicity, reconstitution and stability [15–17,20]. Bulking agents could serve as tonicifier and are used to achieve an elegant and stable non-collapsed cake. Collapse and loosening of porous structure can happen when the product is heated above Tc during the sublimation step. The onset of collapse or the microcollapse is characterized by the presence of small holes in the dried portion of frozen matrix [16].

Sugars or sugar alcohols such as lactose, sorbitol, sucrose and mannitol are typically used as bulking agents. Non-reducing compounds such as mannitol and sucrose are preferred for protein-based formulations to avoid Maillard reaction of the protein with the excipient. Amino acids can also be used as bulking agents, such as histidine, glycine, and arginine. Mannitol may crystallize partially during lyophilization and crystallization may continue after freeze-drying as a result of moisture and heat [21]. Mannitol hemihydrate and the polymorphs α, β, and δ have been observed in freeze-dried products [22].

Due to release of hydrate water upon its conversion into the anhydrous crystal forms the presence of mannitol hemihydrate may lead to stability problems during storage. It has been found that the presence of some excipients especially salts, which are added as buffer components or stabilizers, lyoprotectants or proteins can inhibit mannitol crystallization [22].

Mannitol only can serve as a lyoprotectant in the amorphous form though it predominantly exists in the crystalline state in lyophiles. Only in the amorphous state mannitol can stabilize proteins. Mannitol crystallization may be inhibited by the presence of additives, high cooling rates, or primary drying at low temperature. However, there are situations where it is desirable to have crystalline mannitol as a bulking agent in a freeze-dried product, since the existence of crystalline mannitol in the final lyophile yields elegant cakes. Therefore, the more promising approach is the usage of mannitol in combination with an amorphous lyoprotector [22].

Due to the high eutectic temperature of the mannitol–water system (– 2.2°C) mannitol crystallizes readily in aqueous frozen solutions. This enables to perform the primary drying at elevated temperatures, shortening the lyophilization cycle

time. To maximize mannitol crystallization, an annealing step is often incorporated into freeze-drying process [19,22–27].

Different theories have been proposed about how these excipients stabilize protein-based formulations in freeze-dried products, and these theories may be useful for the lyophilization of the nanocapsules suspensions. The dehydration steps involve the removing of ice and unfrozen water that remains dissolved or adsorbed on the solid phase. Once such process may destabilize the nanoparticles, excipients should be added to serve as lyoprotectants. Such compounds are able to form hydrogen bonds at specific sites on the surface of proteins, and water that is lost during drying is “replaced” by these additives. These lyoprotectants preserve the native structure of nanocapsules by serving as water substitutes, which can keep nanocapsules in a pseudo-hydrated state. Therefore, any stabilization mechanism requires that some of mannitol remain dispersed in the amorphous phase [15,16].

However, a different theory proposes that stabilization is related to immobilization of the protein in a rigid and inert glass matrix, and therefore the protein molecules would remain preserved in their original state [18]. Probably both mechanisms are involved in the stabilization of protein-based formulations, and, may be important during freeze-drying of nanoparticulated systems.

## 2. OBJECTIVES

In our study, mannitol, sucrose, glucose, lactose, and a combination of mannitol with different polymers were investigated in concentrations of 5% and 10% (w/v) as potential excipients and stabilizers during freeze drying of nanocapsules suspensions. Whereas sucrose, glucose, and lactose are known

as stabilizers in freeze-dried protein formulations, mannitol mainly used as a bulking agent. Since the residual humidity content of the freeze-dried formulations may also influence the stability, this parameter was also determined. To determine the robustness of the formulations, different freeze-drying protocols was performed in additional experiments. We were also interested in the impact of annealing procedure during lyophilization process on physicochemical and thermal properties of mannitol nanocapsules-based formulations, mainly with respect to the mannitol crystallization. Finally, the relationship between properties of the lyophilized mannitol formulations and morphology was also evaluated. Scanning electron microscopy (SEM) was used to characterize morphology. In addition, the degree of crystallinity of mannitol was characterized by power X-ray diffraction (XRD).

## 3. MATERIALS AND METHODS

### 3.1. Materials

Chitosan (deacetylation degree: 80%, molecular weight: ~700 kDa) in powder form was purchased from Farma Service Bioextract (Brazil). Ovalbumin, mannitol, sucrose, glucose, lactose, polyvinylpyrrolidone (PVP) (average molecular weight of 25,000 Da), polyvinyl alcohol (PVA) (88% hydrolyzed Mw 31,000 g/mol), poloxamer 407, and polyethylene glycol (PEG 4000) were obtained from Sigma-Aldrich (Brazil). Monochloroacetic acid, acetic acid, sodium hydroxide pellets, calcium chloride, and all the other chemicals used were purchased from Synth and were of analytical grade. The water was purified by Alpha-Q ultra-pure water system (Milipore, Ireland).

### 3.2. Chitosan carboxymethylation

The 6-*O*-carboxymethyl chitosan (6-*O*-CMCS) was prepared based on the procedure described for Abreu and Campana-Filho [28] with some modifications. Briefly, 3 g chitosan were added into 65 ml of 2-propanol to swell and after 20 min of mechanic stirring at room temperature, 23 g of aqueous NaOH (40%) was added drop-wise for 10 min. Then 17.5 g monochloroacetic acid/2-propanol solution (1:1, w/w) were added to the suspension. The reaction proceeded for 12h (at room temperature and the solid was filtered out, rinsed with methanol and neutralized with glacial acetic acid. Then the product was dried at room temperature. After dialyzing against frequent changes of ultra-pure water (every 12 h) for 5 days, the solution was freeze-drying (Dura-Stop MP Dura-Top MP Tray Dryer MNL-031- A, New York, USA) to obtain the cotton-like product. The degree of carboxymethylation of the product was 0.70 as was determined by a previously reported by $^{1}$H NMR method [29–31].

### 3.3. Preparation of Ovalbumin-loaded 6-*O*-CMCS nanocapsules

6-*O*-carboxymethyl chitosan nanocapsules were prepared by ionic gelation using $CaCl_2$ as the cross-linker. Ovalbumin loaded 6-*O*-CMCS nanocapsules (Ova-6-*O*-CMCS Ncs) were prepared by adding ovalbumin solution with calcium chloride (10 mg/ml) drop wise to 6-*O*-CMCS solution (3 mg/ml) under constant stirring for 1 h at 900 rpm resulting in the formation of turbid suspension. The final concentration of ovalbumin was 132 µg/ml.

### 3.4. Particle size measurement

Particle size distribution of Ova-6-*O*-CMCS nanocapsules both before and after lyophilization was deter- mined by dynamic light scattering (DLS Malvern Particle analyzer, England) and nanoparticle tracking analysis (NTA NanoSight NS300, NanoSight, Amesbury, UK). The software used for capturing and analyzing the data was the NTA 3.1 Build 3.1.45. Each measurement was performed in triplicate at 25°C.

### 3.5. Loading efficacy

Ova-6-*O*-CMCS nanocapsules was centrifuged at 12,000 rpm for 30 min and the supernatant was collected. The encapsulation efficiency of ovalbumin in 6-*O*-CMC nanocapsules was determined by fluorescence spectroscopy using ova-FITC.

The loading efficiency (LE) was determined as [7]:

$$LE\ (\%) = \frac{\text{total amount of Ova-FITC} - \text{free Ova-FITC supernatant} \times 100}{\text{total amount of Ova-FITC added}}$$

### 3.6. Freeze-drying cycle

The lyophilization of nanocapsules was performed using a pilot freeze-dryer Dura-Stop MP Dura-Top MP Tray Dryer MNL-031-A (New York, USA). The 2 ml of the formulations were dispensed into 10ml freeze-drying moulded vials. The conditions applied during the present study were: (1) freezing to –50°C with a temperature ramp of 2.5°C/min and holding for 30 min; (2) primary drying performed at –40°C for 6 h and finally (3) secondary drying was performed at a

shelf temperature of 20°C for 4 h. When the annealing procedure was applied, the suspensions were frozen at –50°C (cooling rate of 1°C/min), and then annealing was performed at different temperatures: –5, –10, –15, and –25°C for 1 h. Finally, the samples were cooled again to –50°C and lyophilized under the conditions mentioned above. To determine the end of the sublimation step, the partial pressure of water in the freeze-drying chamber was measured by a hygrometer. The chamber pressure was maintained at 10 mTorr during the drying process and a thermocouple was placed into a vial to monitor the sample temperature. At the end of the lyophilization the vials were stoppered under vacuum which is subsequently broken by injection of nitrogen gas.

### 3.7. Freeze-drying microscopy

The collapse temperature ($T_c$) was measured by a freeze-drying microscope (Linkam Scientific Instruments, Surrey, UK) equipped by a video camera, a computer to capture the collapse image (optical window), a nitrogen cooling system, a vacuum pump, and a small freeze-drying chamber with a temperature controller. Direct observation of the freeze-dried sample was done using a polarized microscope (Nikon Elipse E600, Nikon, Japan)

The samples were cooled at a controlled rate (2.5–20°C/min) to –50°C, held for 1 min and then heated to 25°C at 5°C/min. When the annealing procedure was applied, an annealing step at –5, –10, –15, and –25°C for 5 min was added after the freezing step. The collapse temperature ($T_c$) corresponds to the lowest temperature of overall loss of the initial frozen structure during freeze-drying.

### 3.8. Differential scanning calorimetry (DSC)

Thermal analysis of solutions and freeze-dried samples was performed by a differential scanning calorimeter (DSC) (model Pyris 1; Perkin Elmer LLC, Norwallk, CT, USA) equipped with a cooling system (CryoFill, Perkim Elmer). It was calibrated using indium, mercury, and distilled water as standards. Approximately 15 μl of suspension or 10 mg of dried sample were used in an aluminum pan and sealed. An empty pan was used as the reference. Cooling and heating rates of 2.5–20 and 10–20°C/ min were applied throughout the analysis, respectively.

The suspensions were cooled at a controlled rate (2.5–20°C/min) to –50°C, held for 1 min and then heated to 25°C at 10°C/min. When the annealing procedure was applied, an annealing step at –5, –10, –15, and –25°C for 5 min was added after the freezing step. The second heating scan (to 25°C) was used to determine the characteristic glass transition temperature ($T'_{g\ 2}$). Freeze-dried samples were cooled to –50°C at 2.5°C/min and held for 1 min. The samples were then heated to 250°C at 20°C/min.

### 3.9. X-ray diffraction (XRD)

X-ray diffraction of the lyophilized formulations was performed in a Rigako Diffratometer model Ultima III (Tokyo, Japan). The X-ray diffraction patterns with Cu Kα radiation (*λ* 1⁄4 1.54 Å) at 40 kV and 30 mA were recorded in the range of 2*θ* 1⁄4 4–50°, with steps of 0.05° 2*θ* and a duration of 4 s per step.

### 3.10. Scanning electronic microscopy (SEM)

For observation of porous structure the freeze-dried cakes were extracted from the glass vials and rapidly cut into pieces. The pieces were attached using carbon paint to SEM specimen mounts. The specimens were coated with gold through a sputter coater Desk II Denton Vacuum (Kansas, USA). Imaging was performed on a Jeol JSM-6460LV SEM (Massachusetts, USA) at an accelerating voltage of 15 kV.

### 3.11. Water content analysis

The residual moisture of the lyophilized formulations was measured by Computrac® VAPOR PRO® (Arizona, USA) a green alternative to Karl Fisher method. Approximately 170 mg of powder was used to check that the water content was sufficiently low to ensure good stability during storage.

### 3.12. Stability study

Sealed vials of freeze-dried products stabilized with mannitol 10% (w/v) were stored for 3 months at 4 and 25°C. Every month, the size and the polidispersivity index of rehydrated nanocapsules were determined by DLS. In addition, the residual moisture in freeze-dried products was measured by Computrac® VAPOR PRO® (Arizona, USA).

## 4. RESULTS AND DISCUSSION

### 4.1. Ova-6-*O*-CMC preparation and characterizations

Ova-6-*O*-CMCS nanocapsules were obtained by ionic gelation between carboxyl groups of 6-*O*-carboxymethylchitosan chains and $Ca^{2+}$ from $CaCl_2$ as

cross-linker. DLS analysis resulted in a size average of 169 nm and the polydispersity index was found to be 0.126 ± 0.020 for Ova-6-*O*-CMCS which indicates a monodisperse distribution of nanocapsules suspension. The mean size and distribution of nanoparticles were also analyzed by NTA (Fig. 1), that enables sample visualization and provides approximate particle concentrations. The mean size value obtained by NTA was 124nm, which is about 50nm smaller than the size average given by DLS. Besides, the presence of different populations was clearly detected by sample visualization (Fig. 2).

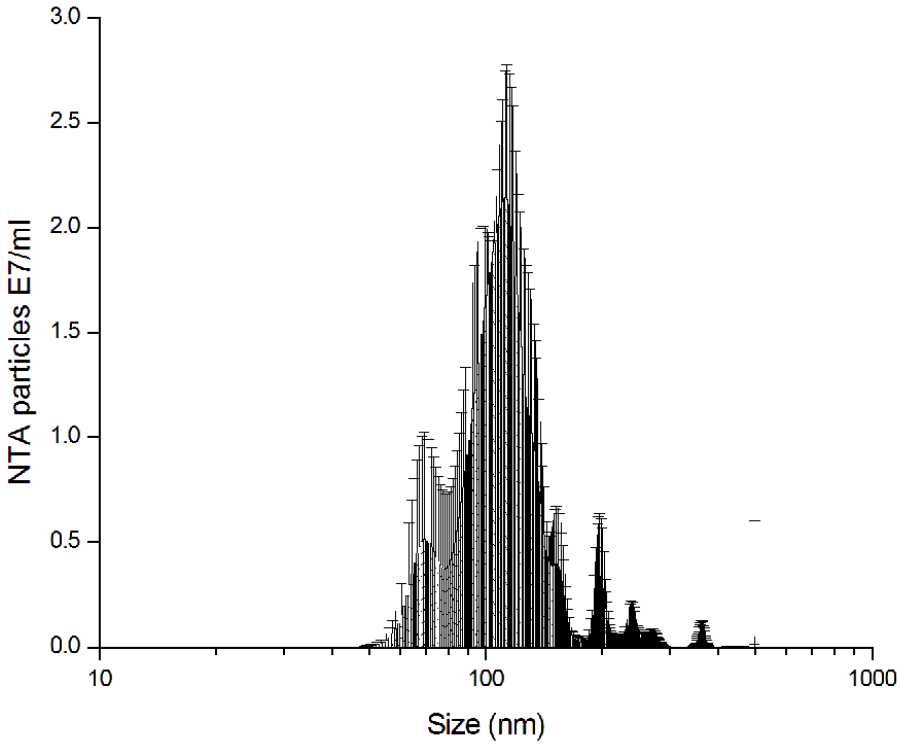


**Figure 1**. Nanoparticle tracking analysis (NTA) size distribution from Ova-6-*O*-CMC nanocapsules.

According to Filipe et al. [32] this is related to the difficult of the DLS software to fit the data of an autocorrelation curve of a sample with has particle populations

with different sizes, resulting in a single peak. In addition, factors such as dilution, opalescence and user experience can affect the distributions of submicron particles [33, 34].

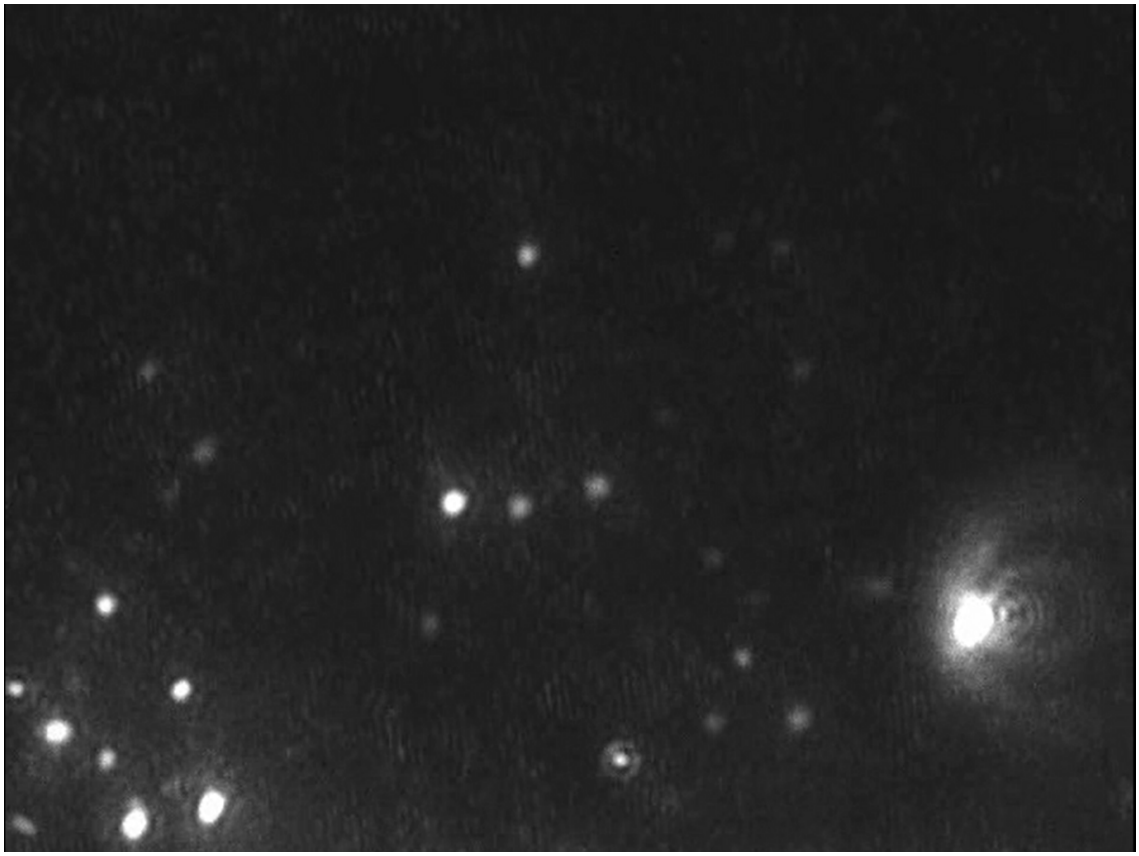

**Figure 2**. Nanoparticle tracking analysis (NTA) video frame from Ova-6-O-CMCS nanocapsules.

The encapsulation efficiency of ovalbumin was found to be 17%. The increase in ovalbumin solution concentration (above 132 µg/ml) keeping constant 6-*O*-CMC concentration resulted in poor encapsulation efficiency. This can be ascribed to the isoelectric point of ovalbumin (4.7) negatively charged under the preparation conditions (~pH 7). This generates an electrical repulsion between ovalbumin and carboxymethyl chitosan also negatively charged under the pH of the synthesis of nanoparticles [35].

### 4.2. Freeze-drying of nanocapsules

The synthetized nanocapsules were then lyophilized with different type of cryoprotectants: lactose, sucrose (disaccharide), glucose (monosaccharide), lactose (disaccharide), mannitol (polyol), and mannitol with polymers (polyvinylpyrrolidone, polyvinyl alcohol poloxamer and polyethylene glycol).

In the case of mannitol 10% (w/v) the conservation of nanocapsules was confirmed after reconstitution of the freeze-dried formulations by diameter measurement, polydispersity index (PI), ratio of nanocapsules size after and before lyophilization ($S_F/S_I$), aspect, reconstitution time and residual humidity (RH) (Table 1). However, for nanocapsules freeze-dried without any cryoprotectant the size of the nanocapsules could not be measured due to the formation of macroscopic aggregates. The lyophilizates obtained using sucrose, glucose, lactose, and mannitol with polymers were collapsed or partially collapse with an important shrinkage of their volume.

Freeze-dried cake with mannitol 10% (w/v) observed by SEM showed the conservation of porous structures and demonstrated a successful freeze-drying of nanocapsules suspension.

**Table 1**. Characterization of Ova-6-*O*-CMCS nanocapsules suspension before and after freeze-drying in presence of different cryoprotectants.

| Cryoprotectant | Concentration (%) | Size ± SD (nm) | | PI ± SD | | $S_F/S_I$ | Aspect | Time (s) | RH (%) |
|---|---|---|---|---|---|---|---|---|---|
| | | Before freeze-drying | After freeze-drying | Before freeze-drying | After freeze-drying | After freeze-drying | | | |
| without cryoprotectant | - | 169.0 ± 1.0 | *** | 0.126 ± 0.020 | *** | *** | Collapsed | *** | 4.10 |
| Mannitol | 5 | 167.9 ± 1.9 | 238.9 ± 10.1 | 0.171 ± 0.003 | 0.240 ± 0.010 | 1.40 | Correct | Immediate | 1.13 |
| Mannitol | 10 | 195.4 ± 1.2 | 212.2 ± 2.6 | 0.176 ± 0.020 | 0.207 ± 0.007 | 1.08 | Correct | Immediate | 1.30 |
| Sucrose | 5 | 160.9 ± 0.5 | 203.2 ± 0.8 | 0.149 ± 0.006 | 0.178 ± 0.014 | 1.26 | Partially collapsed | Immediate | 1.01 |
| Sucrose | 10 | 182.0 ± 1.8 | 262.0 ± 0.4 | 0.151 ± 0.005 | 0.228 ± 0.014 | 1.44 | Partially collapsed | Immediate | 2.31 |
| Glucose | 5 | 161.2 ± 1.6 | 212.9 ± 1.8 | 0.164 ± 0.013 | 0.296 ± 0.018 | 1.32 | Collapsed | 60 s | 1.21 |
| Glucose | 10 | 180.9 ± 1.2 | 201.1 ± 11.3 | 0.169 ± 0.013 | 0.252 ± 0.023 | 1.11 | Collapsed | 240 s | 2.63 |
| Lactose | 5 | 160.9 ± 1.6 | 253.6 ± 1.9 | 0.152 ± 0.019 | 0.188 ± 0.014 | 1.58 | Partially collapsed | Immediate | 4.09 |
| Lactose | 10 | 181.1 ± 0.8 | 203.3 ± 1.1 | 0.152 ± 0.008 | 0.154 ± 0.013 | 1.12 | Partially collapsed | Immediate | 5.98 |
| Mannitol-PVP | 10-1.25 | 865.5 ± 55.1 | 1355.3 ± 24.0 | 0.511 ± 0.025 | 0.377 ± 0.077 | 1.56 | Collapsed | Immediate | 0.64 |
| Mannitol-PVA | 10-1.25 | 483.9 ± 8.8 | 384.6 ± 19.1 | 0.575 ± 0.053 | 0.727 ± 0.060 | 0.79 | Correct | Immediate | 11.60 |
| Mannitol-Poloxamer | 10-1.25 | 141.7 ± 2.7 | 104.6 ± 6.7 | 0.752 ± 0.015 | 0.998 ± 0.002 | 0.74 | Correct | Immediate | 1.92 |
| Mannitol-PEG 4000 | 10-1.25 | 291.2 ± 4.6 | 562.7 ± 7.5 | 0.175 ± 0.020 | 0.294 ± 0.008 | 1.93 | Correct | Immediate | 12.62 |

*** Aggregated suspension
The results of nanocapsules size and polydispersity index are means of three measurements ± SD

### 4.3. Stabilization of nanocapsules during the dehydration step

Nanocapsules were freeze-dried with different excipients: sucrose, lactose, glucose, mannitol, and mannitol with polymers (PVA, PVP, PEG 4000, poloxamer 407). The measurement of the collapse temperature $T_c$ by freeze drying microscopy showed that the different formulations have different collapse temperatures (Table 2).

**Table 2**. Experimental determinations of collapse temperature (*Tc*), glass transition temperature (*Tg'*), and crystallization temperature (*Tcr*) of Ova-6-*O*-CMC nanocapsules suspension in presence of different cryoprotectants.

| Cryoprotectant | Concentration (%) | *Tc*[a] (°C) | *Tg'* [b](°C) | *Tcr*[b] (°C) |
|---|---|---|---|---|
| without cryoprotectant | - | -53.50 | -55.13 | - |
| Mannitol | 5 | -27.90 | -34.90 | -21.10 |
| Mannitol | 10 | -26.10 | -33.94 | -19.50 |
| Sucrose | 5 | -26.40 | -35.89 | - |
| Sucrose | 10 | -26.60 | -34.77 | - |
| Glucose | 5 | -41.80 | -39.53 | - |
| Glucose | 10 | -39.18 | -38.83 | - |
| Lactose | 5 | -31.40 | -43.84 | - |
| Lactose | 10 | -31.80 | -37.62 | - |
| Poloxamer | 2.5 | -30.80 | -21.54 | - |
| PEG 4000 | 2.5 | -34.90 | -20.20 | - |
| PVP | 2.5 | -30.80 | -30.45 | - |
| PVA | 2.5 | -10.50 | -27.00 | - |
| Mannitol-PVP | 10-2.5 | -5.10 | -33.70 | -20.80 |
| Mannitol-PVA | 10-2.5 | -2.40 | -32.93 | -21.00 |
| Mannitol-Poloxamer | 10-2.5 | -26.00 | -34.52 | -23.70 |
| Mannitol-PEG 4000 | 10-2.5 | -26.00 | -34.58 | -25.80 |

a Determined by freeze-drying microscopy
b Determined by DSC

Figure 3 shows the observation of a sample of nanocapsules with mannitol 10% (w/v). In Fig. 3a, the drying is performed at – 50°C and the sublimation front advances within the frozen matrix. In Fig. 3b, the sample is heated to – 23.9°C and the small holes begin to appear in the dried portion signaling the

microcollapse of the sample. In Fig. 3c, the completed collapse can be observed upon heating to – 21.4°C.

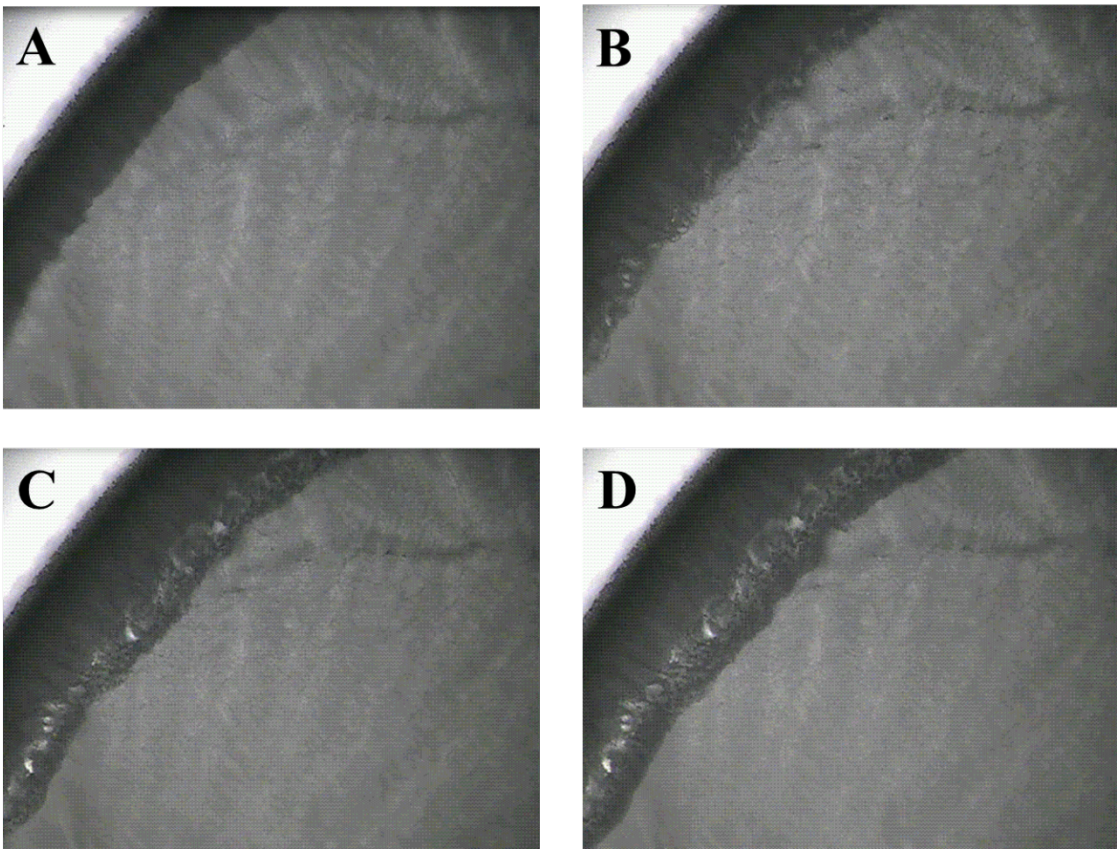


**Figure 3**. Determination of collapse temperature of Ova-6-*O*-CMCS nanocapsules suspension with mannitol at 10% (w/v). (A) Frozen and dried region (B) Micro collapse (C) Onset of overall collapse (D) overall collapse.

The highest $T_c$ corresponds to the nanocapsules freeze-dried with mannitol and PVA (–2.40°C) whereas the nanocapsules freeze-dried without cryoprotectant has the lowest one (– 53.50°C) which can explain the completed collapse observed for this formulation under our freeze-drying condition. The comparison between glass transition temperature $T_g'$ and $T_c$ values for different formulations pointed out two behaviors depending on the nature of the bulking

agent used. These results are in agreement with Passot et al. [20] that found widely lower $T_g'$ values for formulations involving any crystalized solute such as glycine or mannitol. According to Passot et al., [20] the collapse temperature can be defined as a more relevant parameter than $T_g'$ for freeze-drying development and optimization, once formulations involving crystalline bulking agents where freeze-dried at a product temperature higher than $T_g'$ but lower than $T_c$ and provided high storage stability. In addition, the primary drying time could be significantly reduced if the $T_c$ is used to fix the product temperature during the sublimation step. Pikal and Shah [ 36] found a 13% reduction of sublimation time when the product temperature was increased by 1°C.

The residual moisture of the lyophilized formulations was measured by Computrac® VAPOR PRO® (Arizona, USA) a green alternative to Karl Fisher method. The nanocapsules suspensions freeze-dried with mannitol 10% (w/v) showed a residual humidity of 1.30% whereas the collapsed formulation without cryoprotectant had a residual humidity of 4.10% (Table 1). When the product is heated above $T_c$ the pore structures are lost in the dried region and the increase in residual water and reconstitution times are common consequences of collapsed formulations. Figure 4 shows scanning electron micrographs of freeze-dried Ova-6-O-CMCS nanocapsules suspension without cryoprotectant and with mannitol at 10% (w/v). Microscopy demonstrates that mannitol formulations had a leafy amorphous appearance with an irregular array of pores whereas formulations without cryoprotectant presents holes in the structure which indicates the collapse of the dried product.

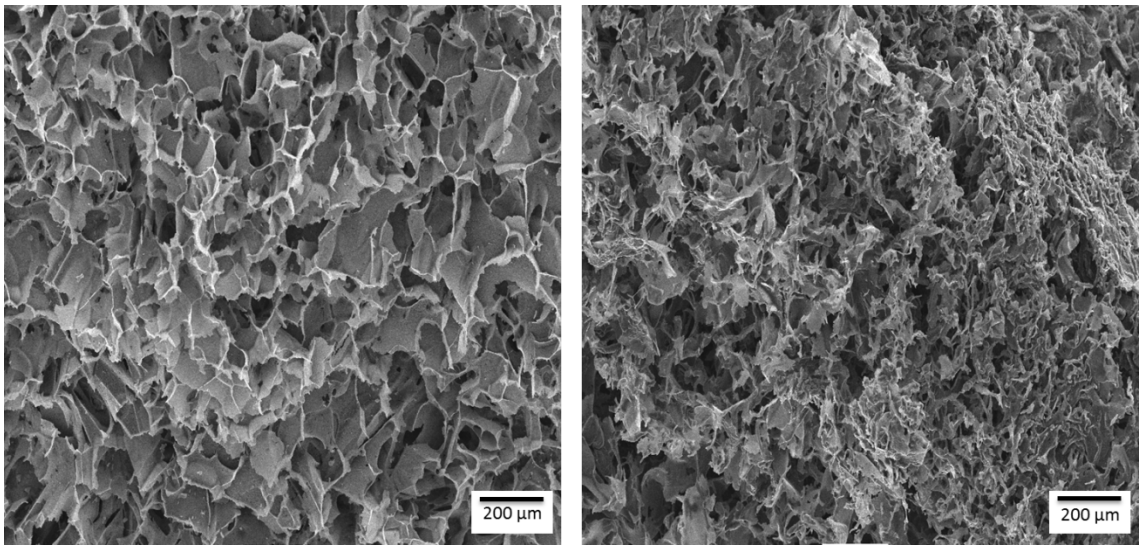


**Figure 4**. Structure of freeze-dried Ova-6-*O*-CMCS nanocapsules suspension without cryoprotectant (right) and with mannitol at 10% (w/v) (left). Note the collapse of the formulation without cryoprotectant and the presence of holes in the structure whereas the plates of formulation with mannitol are intact (magnification 75X).

After freeze-drying the Ova-6-*O*-CMCS nanocapsules size was increased with glucose, lactose and mannitol 5% (w/v) which indicates that the collapse of cryoprotectant matrix during lyophilization did not induce nanocapsules aggregation, once the nanocapsules suspension freeze-dried with mannitol 10% (w/v) did not collapse. According to Abdelwahed et al., [16] on the timescale of processing the nanocapsules aggregation could be extremely slow. However, such collapse increased the residual humidity for formulations freeze-dried with sucrose, glucose, and lactose which can impact the product quality.

### 4.4. Thermal analysis of mannitol frozen formulations: Influence of rates of cooling and temperatures of annealing

Table 2 shows the collapse and the glass transition temperatures depending on the cyoprotectant used in each of the formulations. Such results indicate that during the freezing step the nanocapsules can be within the vitrified matrix of the cryoprotectants. During the freezing step, there is a phase separation that occurs into the cryo-concentrated solution and the ice. Such cryo-concentration solution can vitrify at a certain temperature defined as glass transition temperature of maximally cryo-concentrated solutions and denoted $T'_g$. When the nanocapsules are immobilized within this glassy phase of the cryoprotectant the aggregation is prevented and the nanocapsules are protected against mechanical stress due to the growth of ice crystals [15].

The thermal analysis of the formulation with mannitol 10% (w/v) is show in Fig. 5. Nanocapsules suspensions with mannitol 10% (w/v) were first cooled from room temperature to –50°C at 2.5°C/min. The suspensions were then heated to 25°C at 10°C/min. From DSC heating curve, several thermal events were observed: (1) the glass transition of the amorphous freeze-concentrate occurred at approximately –35°C; The glass transition temperature of the maximally freeze-concentrated mannitol has been reported to be approximately –32°C. (2) An exothermic event attributed to the crystallization of mannitol and the unfrozen water. According to Cavatur et al. [26] the very rapid crystallization may be due to the high molecular mobility of the amorphous freeze-concentrate above the glass transition. (3) An endotherm due to eutectic melting of mannitol and ice [37].

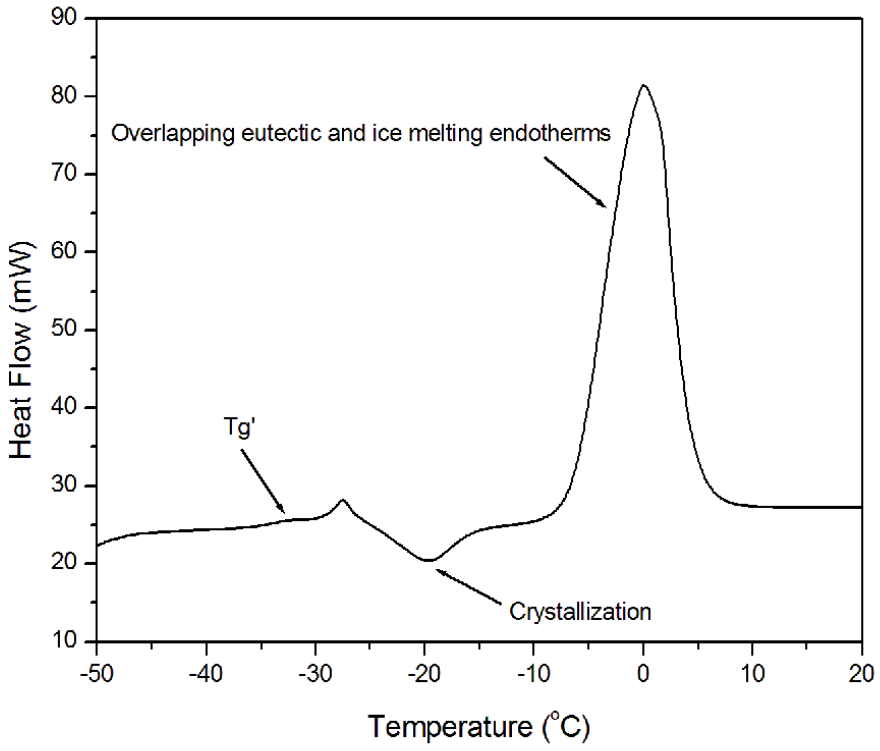


**Figure 5**. DSC heating profile of frozen Ova-6-*O*-CMCS nanocapsules suspension with mannitol 10% (w/v). The suspension was cooled from room temperature to -50ºC at 2.5ºC/min. It was held at -50ºC for 1 min and heated to room temperature at 10ºC/min.

The literature reports the occurrence of two glass transition events for mannitol solutions, with the second glass transition at around –25°C. According to the literature this higher temperature can be attributed to an interfacial interaction between the amorphous phase and ice. Ablett et al. [38] and Izzard et al. [39] concluded that the second glass transition is due to the onset of ice melting. Additionally, there is an experimental artifact related to the overlap of the second glass transition with the crystallization event that makes the interpretation of the heating curves complicated.

Comparing the $T_g'$ values obtained at different cooling rates (Table 3) we found that this thermal event occurred at approximately –35°C. It was observed

that the occurrence of the crystallization exothermic event during heating scan despite all the cooling rates used which indicates that during cooling there was only a partial crystallization of mannitol (Fig. 6).

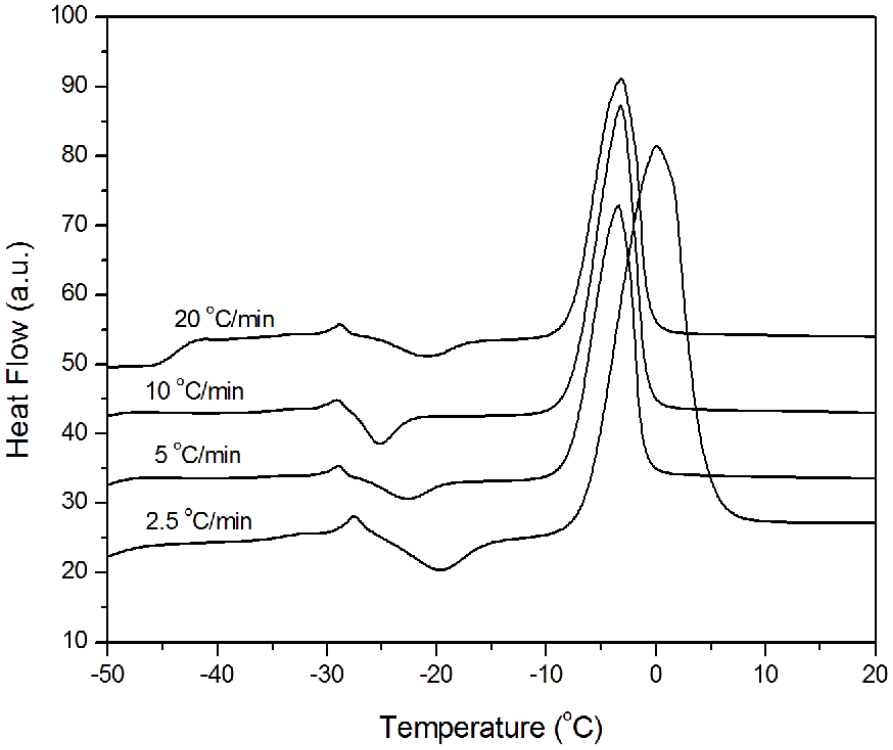


**Figure 6**. DSC heating profile of frozen Ova-6-*O*-CMC nanocapsules suspension with mannitol at 10% (w/v). The suspension was cooled from room temperature to -50°C at 2.5, 5, 10 or 20°C/min. It was held at -50°C for 1 min and heated to room temperature at 10°C/min.

**Table 3**. Experimental determinations of collapse temperature (*Tc*), glass transition temperature (*Tg'*), and crystallization temperature (*Tcr*) of Ova-6-*O*-CMCS nanocapsules prepared with mannitol 10% (w/v) with different rates of cooling

| Rates of cooling (°C/min) | *Tc*[a] (°C) | *Tg'*[b] (°C) | *Tcr*[b] (°C) | ΔH (J/g) |
|---|---|---|---|---|
| 2.5 | -26.10 | -35.13 | -19.00 | 6.68 |
| 5.0 | -25.80 | -35.24 | -22.68 | 7.97 |
| 10.0 | -25.90 | -35.05 | -25.31 | 8.95 |
| 20.0 | -25.90 | -35.65 | -21.03 | 10.95 |

a Determined by freeze-drying microscopy
b Determined by DSC

Even at the slow cooling rates (e.g., 1°C/min) that are typically used during freeze-drying, mannitol crystalizes only partially during cooling, leading to additional crystallization during heating [40]. To demonstrate how cooling rates could influence the crystallization behavior of mannitol, the nanocapsules suspension was cooled at 2.5, 5, 10, and 20°C/min and heated at 10°C/min. At the cooling rate 2.5°C/min mannitol 10% (w/v) in nanocapsules suspension had the chance to crystallize during cooling scan. As a consequence, less material crystallized during heating, resulting in a lowered crystallization enthalpy of –6.68 J/g compared with –8.95 J/g at 10°C/min and –10.95 at 20°C/min. According to Williams and Dean [41] the cooling rate has little or no effect on degree of crystallinity of the end product.

During freeze-drying mannitol tends to crystallize in the α, β, δ, or as mannitol hydrate depending on the process conditions applied during freezing, primary and secondary drying and thereby loses the ability to stabilize the protein or nanocapsules within the glassy matrix [22,40].

Interestingly, Pyne et al. [42] found by in situ XRD during freeze drying of aqueous solution of mannitol 5% (w/w) and glycine 4% (w/w) that the solid state of mannitol (δ-mannitol) at the end of the freeze drying were virtually identical for the slowly cooled (2°C/min) and the rapidly cooled (20°C/min) samples, despite the differences in the solid state of the mannitol and glycine at –70°C and at the beginning of the primary drying at –35°C.

However, Nakagawa et al. [43] showed that for 10% (w/v) freeze dried mannitol solutions the amount of stable form (β polymorph) or meta-stable form (α and δ polymorph) depend on the cooling rates and, therefore, the nucleation temperature of ice. According to these authors, the formation of meta-stable

phases is determined in competition with a crystal nucleation rate, a crystal grow rate, and a polymorphic transition rate (from a meta-stable to a more stable form).

From their assumption, a mannitol crystal nucleation rate corresponds to the ice nucleation rate, and therefore, in case of fast ice nucleation rates there would be enough time for the polymorphic transition, so that some amount of α and δ polymorphs will remain in the bulk. They showed that in case of samples prepared at cooling rate of 2°C/min, the ice crystal of the sample nucleated at higher temperature contained more b polymorph than the samples nucleated at lower temperature. Besides, the polymorph phases were vertically distributed in the sample bulk along the direction of the heat flux during the freezing step, with larger amounts of stable crystals at the top position of the sample.

However, mannitol can be used as a bulking agent in the presence of an amorphous lyoprotector once it can crystallize upon storage. In this case it is important to ensure mannitol crystallization during freeze-drying. In formulations containing lower ratios of mannitol an annealing step may be required to completely crystallize. Kim et al. [44] found that there must be more than approximately 30% by weight mannitol for any crystallinity to be seen.

The next objective was to determine the effect of annealing temperature over the range –5 to –25°C. The annealing process caused a pronounced change in the DSC profiles. The glass transition from the second heating scan ($T_g'_2$) occurred at a higher temperature of approximately –24 and –26°C for samples annealed at –10 and –5°C, respectively, compared with –35°C for unannealed samples (Table 4). Similarly, the comparison between collapse temperature values $T_c$ for annealed and unannealed samples showed a difference of

approximately 17°C, with the highest temperature of –8.60°C for samples annealed at –25°C.

**Table 4**. Experimental determinations of collapse temperature (*Tc*), glass transition temperature (*Tg'*), and crystallization temperature (*Tcr*) of Ova-6-*O*-CMCS nanocapsules prepared with 10% (w/v) of mannitol with different temperatures of annealing

| Temperature of annealing (°C) | *Tc*[a] (°C) | *Tg'*$_1$[b](°C) | *Tg'*$_2$[b] (°C) | *Tcr*[b] (°C) | ΔH (J/g) |
|---|---|---|---|---|---|
| -5.0 | -9.20 | -33.95 | -25.96 | -23.88 | -11.07 |
| -10.0 | -9.10 | -34.60 | -23.88 | -23.23 | -11.96 |
| -15.0 | -8.80 | -34.95 | -29.33 | - | - |
| -25.0 | -8.60 | -34.89 | -32.18 | - | - |
| No annealing | -26.10 | -35.13 | -35.13 | -19.00 | -6.68 |

a Determined by freeze-drying microscopy
b Determined by DSC

In addition, it was observed the occurrence of the crystallization exothermic event during the first heating scan for samples annealed at –10 and –5°C, and the enthalpy of crystallization was much higher compared with unannealed samples (Table 4). According to Pyne et al., [27] this is an indirect evidence that annealing procedure resulted in ice crystallization, decreased the unfrozen water content in the amorphous freeze- concentrate, and increased the glass transition temperatures. This observation is in agreement with our results once samples annealed at –15 or –25°C which showed incomplete crystallization, or no crystallization exothermic event had the lowest glass transition temperatures.

After the samples had been annealed for 5 min, the second warming curve exhibited no thermal event in the region of –50 to –10°C, indicating that this procedure induced the crystallization of mannitol (Fig. 7). Ablett et al. [38] and Chang et al. [45] reported that annealing facilitates ice crystallization resulting in supersaturation of mannitol followed by its nucleation. Therefore, the presence of

nuclei in the annealed samples would be responsible for the crystallization exothermic of mannitol at a lower temperature.

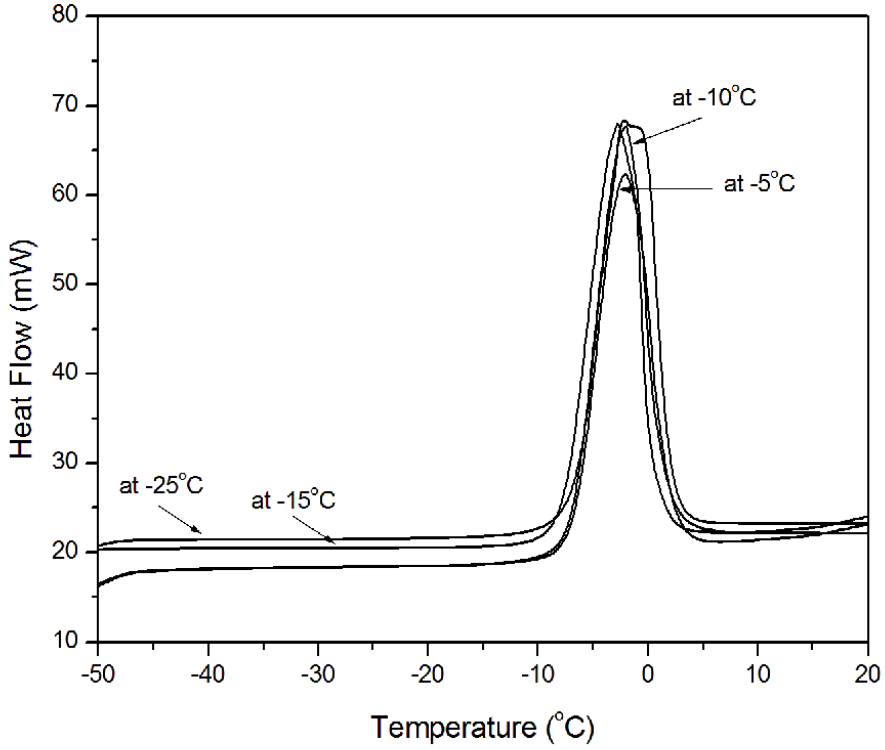


**Figure 7**. DSC heating profile of frozen Ova-6-*O*-CMCS nanocapsules suspension with mannitol at 10% (w/v). The suspensions were cooled from room temperature to -50°C at 2.5 °C/min, heated to the annealing temperature (-25, -15, -10 or -5°C) at 10°C/min, annealed for 5 min, cooled to -50°C, and reheated at 10°C/min. The second heating scans are shown here.

## 4.5. Characterization of the freeze-dried formulations with mannitol

### 4.5.1. Influence of rates of cooling

This preliminary study consisting on freeze-drying of carboxymethyl chitosan nanocapsules with mannitol 10% (w/v), was performed to evaluate the impact of cooling procedure on the size of the nanocapsules prepared by ionotropic gelation. Four cooling procedures were applied on nanocapsules:

immersion in liquid nitrogen, at –196°C, immersion in acetone/dry ice bath at –78°C, and two ramps temperatures of 1 or 2.5°C/min.

The results presented in Table 5 indicates that Ova-6-*O*-CMCS nanocapsules prepared with mannitol 10% (w/v) are very stable during all the freezing procedures performed once the $S_F/S_I$ is very near each other and from 1 confirming the excellent stability. A suggested stabilization mechanism by lyoprotectants is the water replacement hypothesis. This mechanism supposes the formation of hydrogen bonds between polar groups at the nanoparticles surface and a lyoprotectant at the end of the drying process [18]. Therefore, any stabilization mechanism requires that some of mannitol remain dispersed in the amorphous phase [15,16].

### 4.5.2. Influence of temperatures of annealing

This study includes freeze-drying of carboxymethyl chitosan nanocapsules, which was performed to determine the influence of annealing temperature on the size of the nanocapsules. Four freezing protocols were applied: freezing without annealing and freezing with annealing during 1h at four different temperatures –5, –10, –15, and –20°C.

It has been found that annealing at –15°C did not modify significantly nanocapsules sizes and the ratio of nanocapsules sizes after and before annealing ($S_F/S_I$) were about 1. Although for the procedure conducted at –25°C an increase in the nanoparticle size ratio has been observed, the ratio of the nanocapsules polydispersity index after and before annealing was 1.15, that is, the lowest ratio. In addition, for the procedure conducted at –15, –10, and –5°C

it was observed an increase in the ratio of nanocapsules polydispersity index after and before annealing which was 1.68, 1.92, and 2.31, respectively (Table 6).

Such result could be probably explained by regarding the $T_g'$ of this formula prepared with mannitol 10% (w/v) which is about –34°C. This means that three of the four chosen temperatures of annealing (–15, –10, and –5°C) are well above the $T'_g$ of this formulation. The annealing procedure is often used in lyophilization to induce crystallization of excipients, and further this thermal treatment has also dramatic effect on the size distribution of ice crystals within a frozen product [27]. If the annealing temperature is above $T_g'$, ice will melt and smaller ice crystals will melt faster than larger one. It has been found that above $T_g'$ molecular relaxation times decrease exponentially with ($T$ – $T_g'$). Furthermore, this molecular relaxation times and related viscosity and molecular mobility phenomena require a temperature-dependent activation energy > $T_g'$ [15].

**Table 5**. Freeze-drying study of Ova-6-*O*-CMCS nanocapsules prepared at mannitol 10% (w/v) with different rates of cooling

| Cooling procedure | Final temperature (°C) | Size ± SD (nm) | | PI ± SD | | $S_F/S_I$ |
|---|---|---|---|---|---|---|
| | | Before freeze-drying | After freeze-drying | Before freeze-drying | After freeze-drying | After freeze-drying |
| In liquid nitrogen | -196 | 213.2 ± 1.4 | 222.5 ± 1.6 | 0.133 ± 0.011 | 0.184 ± 0.018 | 1.04 |
| Acetone/Dry ice bath | -78 | 210.1 ± 2.8 | 223.7 ± 2.9 | 0.141 ± 0.006 | 0.176 ± 0.004 | 1.06 |
| Freeze dryer shelf | Ramp at 2.5°C/min to -50°C | 205.7 ± 1.3 | 220.5 ± 1.5 | 0.126 ± 0.010 | 0.168 ± 0.010 | 1.07 |
| | Ramp at 1.0°C/min to -50°C | 202.4 ± 1.4 | 217.5 ± 1.9 | 0.132 ± 0.014 | 0.177 ± 0.017 | 1.07 |

The results of nanocapsules size and polydispersity index are means of three measurements ± SD

**Table 6**. Freeze-drying study of Ova-6-*O*-CMCS nanocapsules prepared at mannitol 10% (w/v) with different annealing temperatures

| Temperature of annealing (°C) | Size ± SD (nm) | | P.I ± SD | | $S_F/S_I$ |
|---|---|---|---|---|---|
| | Before freeze-drying | After freeze-drying | Before freeze-drying | After freeze-drying | After freeze-drying |
| -25.0 | 204.5 ± 1.0 | 232.5 ± 2.5 | 0.117 ± 0.012 | 0.135 ± 0.010 | 1.14 |
| -15.0 | 208.4 ± 1.1 | 212.4 ± 1.2 | 0.106 ± 0.010 | 0.178 ± 0.010 | 1.01 |
| -10.0 | 210.3 ± 1.1 | 256.5 ± 3.7 | 0.125 ± 0.012 | 0.240 ± 0.014 | 1.22 |
| -5.0 | 208.0 ± 1.2 | 261.8 ± 9.9 | 0.119 ± 0.017 | 0.276 ± 0.060 | 1.26 |

The results of nanocapsules size and polydispersity index are means of three measurements ± SD

### 4.5.3. Effect of annealing procedure on thermal properties of the freeze-dried formulations with mannitol

For nanocapsules suspensions with mannitol 10% (w/v) the appearance of the freeze-dried samples was identical with or without annealing at –5, –10, –15, or –25°C, and there was no collapse and shrinkage of the dried cake. From X-ray diffraction analysis, the crystalline modification of mannitol in the freeze-dried formulation was identified to be the δ-polymorph regardless of the applied freeze-drying protocol used, which was confirmed by DSC results (Fig. 8).

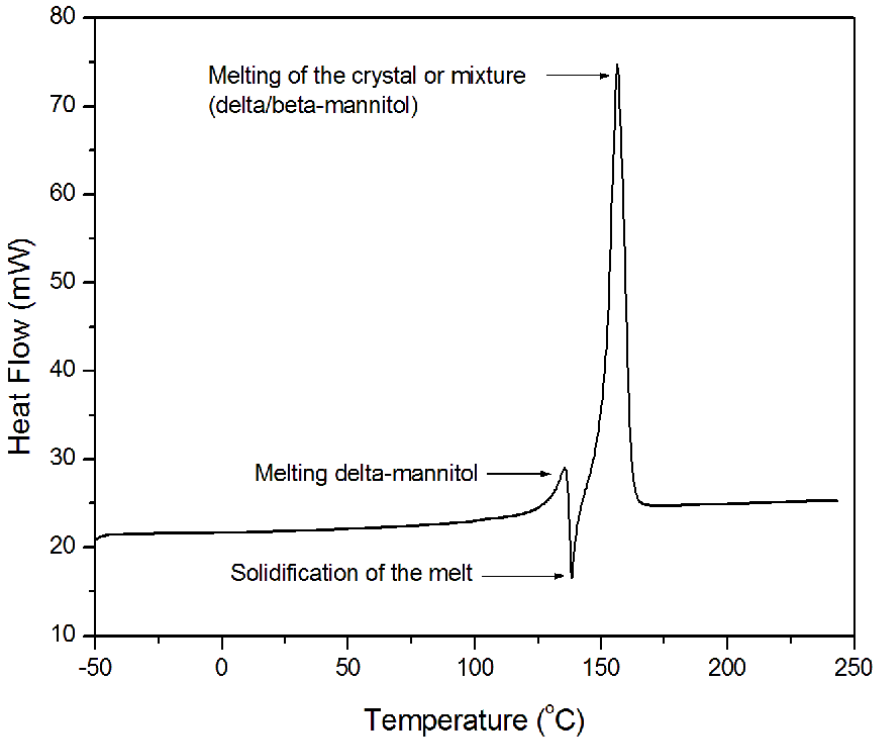


**Figure 8**. DSC heating profile of freeze-dried Ova-6-*O*-CMCS nanocapsules suspension with mannitol 10% (w/v). The dried sample was cooled from room temperature to -50ºC at 2.5ºC/min. It was held at -50ºC for 1 min and heated 250ºC at 20ºC/min

These results are in agreement with that described in literature [46]. According to Burger et al., [47] DSC curves of δ-mannitol shows melting between

150 and 158°C, followed by the solidification of the melt to form β-mannitol and/or α-mannitol and the melting of the respective crystal form or mixture. These authors showed that the transition of δ-mannitol into β-mannitol was induced at approximately 130°C, with a subsequent melting at 150–158°C.

The glass transition temperature (seen as a step change in baseline of heat flow) for samples annealed at –10°C was the highest when compared with samples annealed at –5, –15 or –25°C (Fig. 9) (Table 7). These results are also in agreement with X-ray diffraction analysis that showed the highest crystallinity degree for samples annealed at –10°C.

**Table 7**. Glass transition temperatures (*Tg*) of freeze-dried Ova-6-*O*-CMCS nanocapsules prepared with mannitol 10% (w/v) with different annealing temperatures measured by DSC at 20ºC/min

| Process | Annealing procedure | *Tg* (ºC)[a] |
|---|---|---|
| I | without annealing | 58.84 |
| II | -25.0 | 68.48 |
| III | -15.0 | 68.35 |
| IV | -10.0 | 72.81 |
| V | -5.0 | 61.02 |

a Determined by DSC

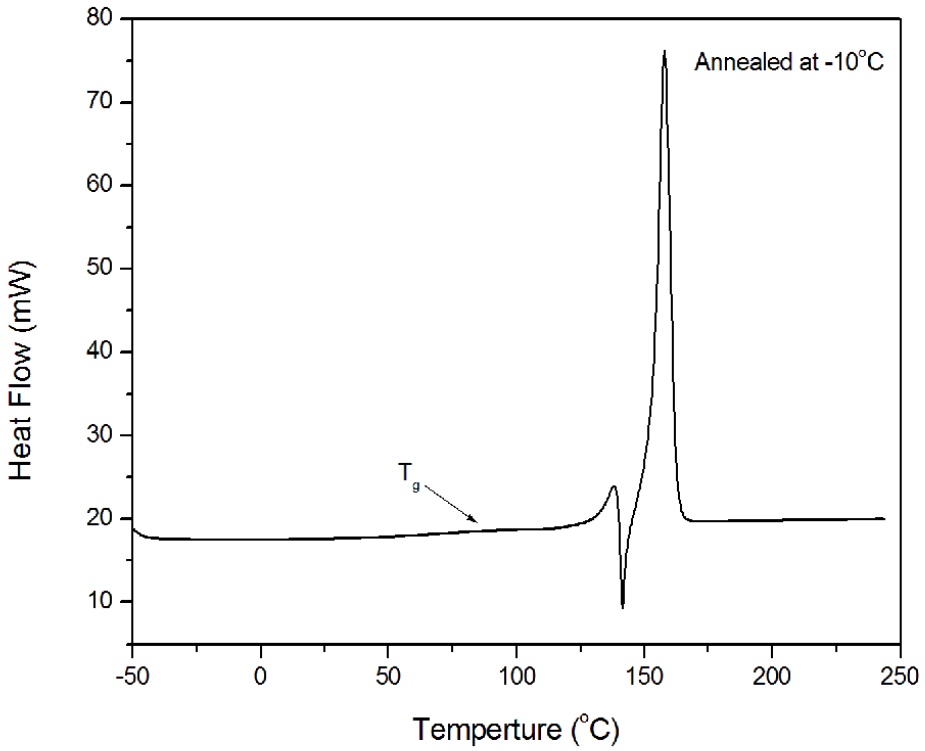


**Figure 9**. DSC heating profile of freeze-dried Ova-6-*O*-CMCS nanocapsules suspension with mannitol 10% (w/v). The dried sample was cooled from room temperature to -50ºC at 2.5ºC/min. It was held at -50ºC for 1 min and heated 250ºC at 20ºC/min.

According to Kim et al. [44] the glass transition temperature of amorphous mannitol was measured as 13°C, meaning that mannitol would be expected to reduce the overall glass transition temperature of the model formulation in this study, which can explain the highest glass transition temperature for highly crystalline samples. Kim et al. [44] studied the glass transition of two-component freeze-dried solids by modulated DSC in the range of mannitol concentration below which crystalline mannitol could be detected by X-ray powder analysis. They reported that the glass transition decreases markedly as the relative concentration of mannitol increases demonstrating the plasticizer effect of mannitol.

Similarly, Dixon et al. [48] reported that for soluble interleukin receptor (sIL-13r) formulations from 0 to 9.2 mg/ml the glass transition temperature of the mobile phase increases as a function of protein concentration. These authors showed that polymorphic crystalline mannitol (a mixture of mannitol hydrate, β-, and δ-mannitol) converts to δ-mannitol for sIL-13r. Comparable results have been identified for human serum albumin (HAS). Hawe and Friess [40] showed that a stable amorphous state can be achieved by increasing the fraction of stabilized-HSA to 1.5%, where mannitol remains amorphous after freeze-drying and 24 months at 25°C/60% RH.

### 4.5.4. XRD of lyophilized formulations produced with different annealing temperatures

The effect of annealing and secondary drying on the formation of crystalline mannitol was investigated for formulations with mannitol 10% (w/v). The annealing step throughout freeze-drying was applied for 1 h at a shelf temperature of –5, –10, –15, or –25°C (Table 8).

**Table 8**. Pore equivalent surface area of Ova-6-*O*-CMCS nanocapsules prepared at mannitol 10% (w/v) of without annealing and at four different annealing temperatures

| Process | Annealing procedure | *A* equivalent (μm) |
|---|---|---|
| I | without annealing | 75.16 ± 26.1 |
| II | -25.0 | 72.72 ± 24.0 |
| III | -15.0 | 71.96 ± 25.0 |
| IIIa | -15.0 | 75.29 ± 24.1 |
| IV | -10.0 | 70.19 ± 25.3* |
| V | -5.0 | 79.29 ± 22.9 |

Data's are present as the mean ± SD (n = 3 for pore surface area determination); *P< 0.05 relative to the corresponding sample without annealing.

Whereas DSC offers information on amorphous and crystalline phases in the frozen state, only XRD can identify and characterize the crystalline phases according to their composition. In case of mannitol it can crystallize in the α-, β-, δ-modification or as mannitol hydrate depending on the applied freezing protocol and the process conditions during primary and secondary drying. It was reported a crystallization of mannitol in a metastable hydrate form during lyophilization and freezing [22,40].

For all lyophilization cycles the presence of δ-mannitol was revealed by XRD experiments (Fig. 10), and when the annealing step was eliminated the diffraction pattern was not affected. In addition, from X-ray powder data of the cake no mannitol hydrate was present which was confirmed by DSC, where the magnitude of an endotherm at 80°C is proportional to the amount of mannitol hydrate (Fig. 8) [42]. On the contrary, whereas Hawe and Frieß [22] reported the characteristic mannitol hydrate peak at 17.4° 2$\theta$ in 4.0% mannitol–1.0% sucrose formulations for all annealing and secondary temperatures tested, Johnson et al. [42] found a mixture of δ-mannitol and β-mannitol in mannitol–sucrose formulations at a ratio of 4:1 only after a secondary drying at 45°C for 18 h.

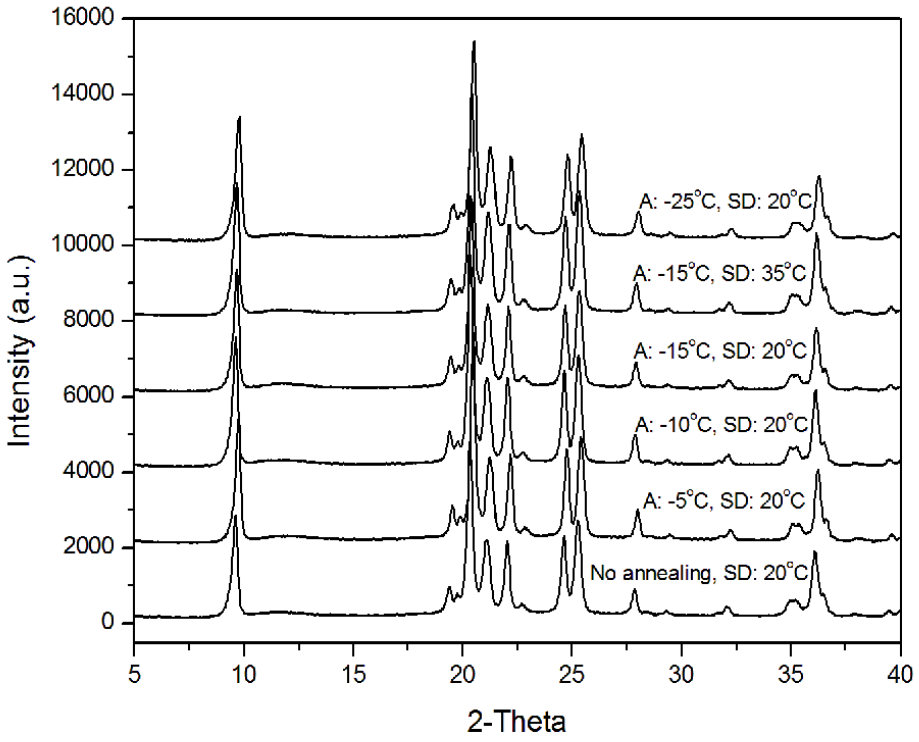


**Figure 10**. XRD of lyophilized Ova-6-*O*-CMCS nanocapsules with mannitol at 10% (w/v) after different annealing (A) and secondary drying (SD) parameters.

Haikala et al. [49] reported that the amount of polysorbate 80 as a surface-active agent increased the crystallinity of mannitol in the lyophilization process and changed the polymorph. According to these authors freeze-dried pure mannitol was a mixture of α-, β-, and δ-polymorphs, and when the concentration of polysorbate 80 was 0.01% (w/v) or more, the fraction of δ-polymorph increased. In our study, all the formulations included this surface-active agent with a concentration above 0.01% (w/v), which can explain the presence of crystalline mannitol only as the delta form after freeze-drying process.

The peak area and the relative intensity of the δ-mannitol at 9.7° 2$\theta$ were used to compare de amount of δ-mannitol formed after different lyophilization

cycles. For the relative intensity, the peak area of the δ-mannitol was compared to the highest peak area of the diffraction pattern, that was set as 100% (Fig. 11).

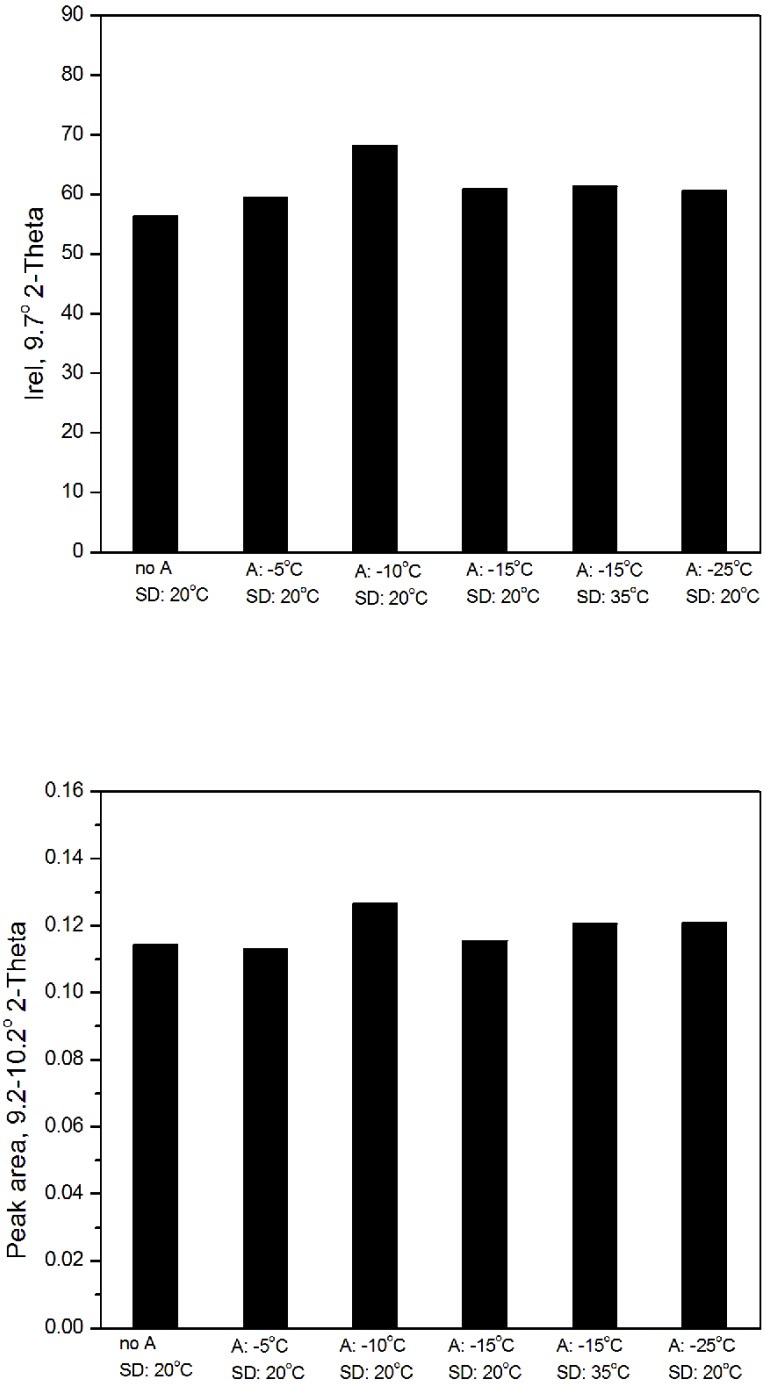


**Figure 11**. Peak area (A) and relative intensity (B) of δ-mannitol peak at 9.7° 2*θ* after lyophilization of Ova-6-*O*-CMCS nanocapsules suspension with mannitol at 10% (w/v) using different annealing (A) and secondary drying (SD) conditions.

The lowest amount of δ-mannitol was found for formulations dried without an annealing step. Comparing the different annealing and secondary drying temperatures the formation of δ-mannitol was more pronounced at –10°C annealing temperature. Compared to the effect of annealing the secondary drying temperature did not have influence on the formation of δ-mannitol when the temperature was increased from 20 to 35°C. Therefore, it seems that conducting lyophilization with an annealing temperature of –10°C is beneficial for the product to achieve the highest mannitol crystallinity which was also confirmed by DSC, where the crystallization enthalpy of –11.96 J/g was the highest for samples annealed at –10°C.

Mehta et al. [23] reported that the physical form of mannitol in the frozen solution and the final lyophile were identical and it was dictated by the temperature of crystallization. They found that crystallization of anhydrous mannitol is favored at temperatures ≥ –10°C, whereas at temperatures ≤ –20°C, mannitol hemihydrate is the preferred physical form when the solutions were cooled from 0°C directly to the desired annealing temperature of –10, –15, or –20°C. When solution was cooled to –50°C, warmed and annealed, either at –10 or at –20°C, only mannitol hemihydrate was observed.

Once it is essential to ensure the mannitol crystallization, the annealing process is often performed for formulations containing mannitol as a bulking agent to maximize mannitol crystallization during the freezing step. In addition, it is well known that the presence of some excipients, such as buffer components, proteins, lyoprotectants. and salts can promote mannitol crystallization. According to Cannon and Trappler, [50] the mixture of mannitol polymorphs

obtained in a freeze-dried product may be sensitive to the details of the formulation and the freeze-drying cycle.

### 4.5.5. Effect of annealing on porosity of freeze-dried product

The morphological characteristics of the freeze-dried cake and the texture of the frozen matrix are strongly impacted by freezing procedure, once the freezing process influence the growth of ice crystals and consequently the primary and secondary steps. Besides, all these stages of the process can influence the porosity and the final cake surface [18].

Figure 12 shows the scanning electron micrographs of freeze-dried Ova-6-*O*-CMCS nanocapsules suspension with mannitol 10% (w/v) without and with annealing at –5°C. Table 9 presents the values of equivalent pore surface area of each sample for different annealing temperatures. These results show that 90% of the porous population has an equivalent area less than 110 μm for a sample freeze-dried without annealing whereas 90% of the population has an equivalent area less than 100 μm for annealed samples. According to these results we can conclude that the annealing procedure decrease the pore surface area in the freeze-dried formulations which can increase the resistance water vapor transfer across the dried mass, resulting in increased primary drying time.

**Table 9**. Freeze-drying conditions used for the production of Ova-6-*O*-CMCS nanocapsules formulations prepared at mannitol 10% (w/v)

| Process | Annealing procedure | Secondary drying shelf temperature |
|---|---|---|
| I | without annealing | 20ºC |
| II | -25.0 | 20ºC |
| III | -15.0 | 20ºC |
| IIIa | -15.0 | 35ºC |
| IV | -10.0 | 20ºC |
| V | -5.0 | 20ºC |

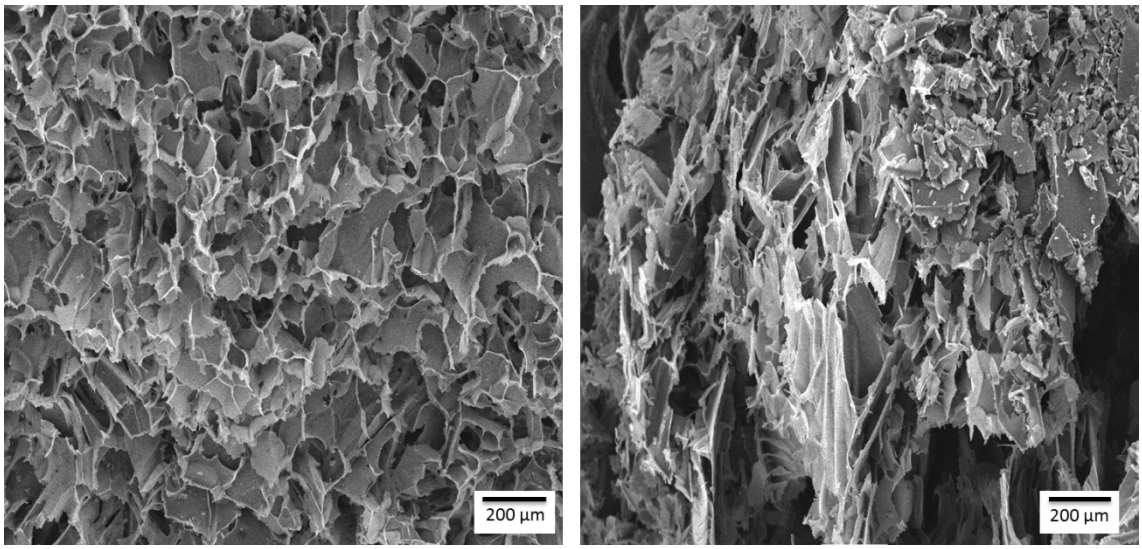


**Figure 12**. Structure of freeze-dried Ova-6-*O*-CMCS nanocapsules suspension without annealing (right) and with annealing at -5ºC (left) (magnification 75X).

Lu and Pikal [19] reported that annealing causes a significant increase in product resistance and primary drying time. They suggest that the crystallization of solute in mannitol-trehalose-sodium chloride-based formulations during annealing and the corresponding reduction of collapse that increases the dry layer resistance. Lu and Pikal [19] showed that only the cake annealed at –23 and –33°C survived freeze-drying with no significant loss of structure, whereas the unannealed cake was a highly porous structure with large and continuous

pathways for water vapor flow. According to these authors for annealed samples the δ-mannitol crystals randomly distributed throughout the cake block the pathways for water vapor diffusion and create a larger resistance to vapor flow, compared with the cake with large connected pores characteristic of the unannealed samples. These findings are perfectly in agreement with our results that reported the lowest pore surface area for samples annealed at –10°C, which in turn exhibit the highest crystallinity degree according to the X-ray diffraction analysis. Moreover, according to Lu and Pikal [19] the rigid crystalline structure of the sugar alcohol provides an excellent matrix to support the cake structure after ice sublimation, avoiding collapse of the cake when the sample temperature exceed the glass transition temperature of the amorphous phase.

However, using a direct characterization method of the ice crystal size, Hottot et al. [51] found that an annealing treatment of 3 h at –10°C increased the average pore diameters (40%) of a protein formulation and decreased the primary drying time (–16%). Abdelwahed et al. [15] reported that annealing of a nanocap- sules suspension could accelerate the sublimation rate without any modification of nanocapsules size in the case of sucrose and PVP as cryoprotectants. According to these authors such acceleration of sublimation rate seems to depend on the annealing temperature. They found that an annealing treatment of 1 h at –10°C increased the average pore diameters of this nanocap- sules formulation by approximately 27%. According to Searles et al., [52] holes on the freeze-dried cake surface form and enlarge by drainage of the amorphous film into adjacent junctions. The thinnest area of the film between the junctions is most susceptible to instabilities, and the rupture would be followed by film

retraction from the edges with large positive curvature to the junctions due to their negative radii of curvature.

Searles et al. [52] showed that after an annealing procedure the drying rate could increase up to 3.5-fold, and with only 30min of annealing a significant rate enhancement could be achieved. These authors hypothesize that annealing could remove some of the drying rate heterogeneity through homogenization of the ice crystal sizes between samples. Because of the heterogeneities in vial condition, particulate content and positional variations within the freeze-drier, samples may nucleate at varying temperatures, resulting heterogeneities in drying rates and therefore in product quality.

Annealing eliminates variation in initial ice crystal size distribution induced by variable temperatures of nucleation and the resulting heterogeneity in drying rates due to the size-dependence of the phase behavior and ripening process. According to Searles et al. [52] annealing increased the ice crystals size by Ostwald repining. If the annealing temperature is above $T_g'$ ice will melt faster than larger ones, and the smallest ice crystals may melt completely. Ostwald ripening (recrystallization) is a phenomenon by which dispersed crystals smaller than a critical size decrease in size whereas those larger ones grow. It can be diffusion or surface-attachment limited. From our results, clearly for samples annealed at –10, –15, and –25°C the decrease in the pore surface area results of structural changes other than Ostwald ripening.

### 4.6. Stabilization of nanocapsules in dried state during the storage

To further evaluate stability of Ova-6-*O*-CMCS nanocapsules not only in connection to the freeze-drying conditions but also regard to short-term stability,

freeze-dried formulations annealed at –15 and –25°C were included in a 3-month stability at 2–8°C (refrigerated conditions) as well as at room temperature (22–25°C). Directly after the freeze-drying process and after periods of, 4, 8, and 12 weeks samples were analyzed with regard to particle diameter and polydispersity index. Residual moisture content of the samples was determined directly after lyophilization and after a storage time of 12 weeks. The results of this study are shown in Tables 10 and 11.

After 3 months of storage there was no collapse and shrinkage of the dried cake. Directly after the freeze- drying process the formulations showed a residual humidity of approximately 0.55% for samples annealed at –15°C and 0.76% for samples annealed at –25°C. After a storage period of 12 weeks samples annealed at –15°C stored at 2–8 and 22–25°C showed no increase of the residual humidity. The samples annealed at –25°C showed an increase of the residual humidity up to 1.05% for samples stored at room temperature and 0.86% for samples stored at refrigerated conditions.

**Table 10**. The size of nanocapsules, the residual humidity RH (%), and the aspects of freeze-dried Ova-6-*O*-CMCS nanocapsules prepared at mannitol 10% (w/v) before and after three months of storage at 25°C

| Temperature of annealing (°C) | Before storage | | | After storage for 3 months at 25°C | | |
|---|---|---|---|---|---|---|
| | Size of NCs (nm) | RH (%) | Aspect | Size of NCs (nm) | RH (%) | Aspect |
| -25 | 211.5 ± 5.3 | 0.76 ± 0.02 | Correct | 287.5 ± 6.8 | 1.05 ± 0.05 | Correct |
| -15 | 217.4 ± 2.6 | 0.55 ± 0.03 | Correct | 279.1 ± 3.4 | 0.63 ± 0.03 | Correct |

The results of nanocapsules size and residual humidity are means of three measurements ± SD

**Table 11**. The size of nanocapsules, the residual humidity RH (%), and the aspects of freeze-dried Ova-6-*O*-CMCS nanocapsules prepared at mannitol 10% (w/v) before and after three months of storage at 4°C

| Temperature of annealing (°C) | Before storage | | | After storage for 3 months at 4°C | | |
|---|---|---|---|---|---|---|
| | Size of NCs (nm) | RH (%) | Aspect | Size of Ncs (nm) | RH (%) | Aspect |
| -25 | 211.5 ± 5.3 | 0.76 ± 0.02 | Correct | 251.9 ± 1.7 | 0.86 ± 0.04 | Correct |
| -15 | 217.4 ± 2.6 | 0.55 ± 0.03 | Correct | 241.6 ± 5.3 | 0.56 ± 0.03 | Correct |

The results of nanocapsules size and residual humidity are means of three measurements ±

Although the residual humidity of the formulations was enhanced for samples annealed at –25°C, the nanocapsules still showed acceptable short-term storage stability with regard to the residual water content. However, the particle diameter and polydispersity index increased over the storage time. Especially for samples stored at room temperature the polydispersity index rose up to 0.292, indicating a heterogeneous particle size distribution (data not shown). Although samples stored at 2–8°C showed a smaller increase of particle diameter (Table 11) and polydispersity index in comparison to the samples stored at room temperature, storage stability was a problem in the presence of mannitol. According to Anhorn et al. [53] the particles became larger and more heterogeneous, the higher the temperature of the storage condition and the longer the storage time in the presence of sugar alcohol.

After freeze-drying process regardless of the applied protocol used, the X-ray diffraction analysis showed the presence of crystalline δ-mannitol which can explain the instability of nanocapsules included within the dried cake. These results are in accordance with the work of Anhorn et al. [53] and Carpenter et al. [54]. According to these authors nanoparticles can be stored for a sufficient period of time with the conservation of their size and polydispersity if an amorphous excipient is present. The crystallization of this bulk lyoprotectant can destabilize the nanoparticles inducing their aggregation. However, adding special additives may delay the nucleation event which start the crystallization process [24,25].

## 5. CONCLUSION

This study demonstrated that Ova-6-*O*-CMCS nanocapsules can be stabilized during freeze-drying process when using adequate concentrations of suitable excipients. The study reported that the lyophilization process has the potential to negatively influence stability if not using suitable excipients during the process. Ova-6-*O*-CMCS nanocapsules stability was evaluated in the presence of mannitol and assessed by particle diameter, polydispersity index and residual humidity. Mannitol in concentration of 10% (w/v) was well suited to preserve nanocapsules from aggregation during lyophilization and subsequent reconstitution. Although mannitol has resulted in elegant freeze-dried cakes, it led to an increase in particle diameter and polydispersity index after short-term storage even at 10% (w/v) most likely due to crystallization of this excipient during the freezing or the desiccation step that can destabilize these fragile nanocapsules. The physical state of mannitol in the freeze-dried products is affected by both formulation and processing parameters and it should be recognized when carrying out process validation studies intended to identify processing variables. As indicated earlier, the presence of mannitol hemihydrate in the final lyophilized product is undesirable because it can dehydrate during product storage and the release water can cause undesirable physical and chemical changes in other formulation components. The freeze-dried formulations contained exclusively δ-mannitol for all studied lyophilization protocols. The addition of an annealing step shifted the $T_g'$ and $T_c$ of mannitol formulations to higher temperatures, which consist of critical parameters for a freeze-drying process with respect to collapse of the lyophilized products. The impact of annealing on porosity of freeze-dried product was studied. The results

showed that annealing has an impact on porosity of freeze-dried cake by nearly complete crystallization of mannitol, once the crystalline matrix prevents the partial collapse and the formation of larger pores observed without annealing. Therefore, the usual observation that annealing increases the pore size due to growth of ice crystal size does not always apply, at least when crystallization of solute is involved.

## 6. REFERENCES


1. Moghimi, S. M.; Hunter, A. C.; Murray, J. C. Nanomedicine: Current Status and Future Prospects. *FASEB J.* **2005**, *19*(3), 311–330.
2. Torchilin, V. P. Target Pharmaceutical Nanocarriers for Cancer Therapy and Imaging. *AAPS J.* **2007**, *9*(2), E128–E14.
3. Soppimath, K. S.; Aminabhavi, T. M.; Kulkarni, A. R.; Rudzinski, W. E. Biodegradable Polymeric Nanoparticles as Drug Delivery Devices. *J. Control. Release* **2001**, *70*(1–2), 1–20.
4. Van der Lubben, I. M.; Kersten, G.; Fretz, M. M.; Beuvery, C.; Verhoef, J. C.; Junginger, H. E. Chitosan Microparticles for Mucosal Vaccination Against Diphtheria: Oral and Nasal Efficacy Studies in Mice. *Vaccine* **2003**, *21*(13–4), 1400–1408.
5. Vila, A.; Sánchez, A.; Janes, K.; Behrens, I.; Kissel, T.; Jato, J. L. V.; Alonso, M. J. Low Molecular Weight Chitosan Nanoparticles as New Carriers for Nasal Vaccine Delivery in Mice. *Eur. J. Pharm. Biopharm.* **2004**, *57*(1), 123–131.
6. Sayin, B.; Somavarapu, S.; Li, X. W.; Thanou, M.; Sesardic, D.; Alpar, H. O.; Senel, S. Mono-*N*-carboxymethyl Chitosan (MCC) and *N*-trimethyl Chitosan

(TMC) Nanoparticles for Non-Invasive Vaccine Delivery. *Int. J. Pharm.* **2008**, *363*(1–2), 139–148.

7. Smitha, K. T.; Sreelakshmi, M.; Nisha, N.; Jayakumar, R.; Biswas, R. Amidase Encapsulated *O*-carboxymethyl Chitosan Nanoparticles for Vaccine Delivery. *Int. J. Biol. Macromolec.* **2014**, *63*, 154–157.
8. Jiang, H.-L.; Park, I.-K.; Shin, N.-R.; Kang, S.-G.; Yoo, H.-S.; Kim, S.-I.; Suh, S.-B.; Akaike, T.; Cho, C.-S. In Vitro Study of the Immune Stimulating Activity of an Athrophic Rhinitis Vaccine Associated to Chitosan Microspheres. *Eur. J. Pharm. Biopharm.* **2004**, *58*(3), 471–476.
9. López-León, T.; Carvalho, E. L. S.; Seijo, B.; Ortega- Vinuesa, J. L.; Bastos-González, D. Physicochemical Characterization of Chitosan Nanoparticles: Electrokinetic and Stability Behavior. *J. Colloid Interface Sci.* **2005**, *283*(2), 344–351.
10. Igartua, M.; Hernandez, R. M.; Esquisabel, A.; Gascon, A. R.; Calvo, M. B.; Pedraz, J. L. Enhanced Immune Response after Subcutaneous and Oral Immunization with Biodegradable PLGA Microspheres. *J. Control. Release* **1998**, *56*(1–3), 63–73.
11. Heritage, P. L.; Underdown, B. J.; Brook, M. A.; Mc Dermott, M. Oral Administration of Polymer-Grafted Starch Microparticles Activates Gut-Associated Lymphocytes and Primes Mice for a Subsequent Systemic Antigen Challenge. *Vaccine* **1998**, *16*(20), 2010–2017.
12. Liu, Z.; Jiao, Y.; Wang, Y.; Zhou, C.; Zhang, Z. Polysaccharides-based Nanoparticles as Drug Delivery Systems. *Adv. Drug Deliv. Rev.* **2008**, *60*(15), 1650–1662.

13. Behrens, I.; Vila-Pena, A. I.; Alonso, M. J.; Kissel, T. Comparative Uptake Studies of Bioadhesive and Non-bioadhesive Nanoparticles in Human Intestinal Cell Lines and Rats: The Effect of Mucus on Particle Absorption and Transport. *Pharm. Res.* **2002**, *19*(8), 1185–1193.
14. Huang, M.; Khor, E.; Lim, L. Y. Uptake and Cytotoxicity of Chitosan Molecules and Nanoparticles: Effects of Molecular Weight and Degree of Deacetylation. *Pharm. Res.* **2004**, *21*(2), 344–353.
15. Abdelwahed, W.; Degobert, G.; Fessi, H. A Pilot Study of Freeze-Drying of Poly(epsilon-caprolactone) Nanocapsules Stabilized by Poly(vinyl alcohol): Formulation and Process Optimization. *Int. J. Pharm.* **2006**, *309*(1–2), 178–188.
16. Abdelwahed, W.; Degobert, G.; Fessi, H. Investigation of Nanocapsules Stabilization by Amorphous Excipients during Freeze-Drying and Storage. *Eur. J. Pharm. Biopharm.* **2006**, *63*(2), 87–94.
17. Abdelwahed, W.; Degobert, G.; Fessi, H. Freeze-drying of Nanocapsules: Impact of Annealing on Drying Process. *Int. J. Pharm.* **2006**, *324*(1), 74–82.
18. Abdelwahed, W.; Degobert, G.; Stainmesse, S.; Fessi, H. 2006c. Freeze-Drying of Nanoparticles: Formulation Process and Storage Considerations. *Adv. Drug Deliv. Rev.* **2006**, *58*(15), 1688–1713.
19. Lu, X.; Pikal, M. Freeze-Drying of Mannitol–Trehalose–Sodium Chloride-Based Formulations: The Impact of Annealing on Dry Layer Resistance to Mass Transfer and Cake Structure. *Pharm. Dev. Technol.* **2004**, *9*(1), 85–95.
20. Passot, S.; Fonseca, F.; Alarcon-Lorca, M.; Rolland, D.; Marin, M. Physical Characterization of Formulations for Development of Two Stable Freeze-

Dried Proteins During Both Dried and Liquid Storage. *Eur. J. Pharm. Biopharm.* **2005**, *60*(3), 335–348.

21. Costantino, H. R. Excipients for Use in Lyophilized Pharmaceutical Peptide, Protein, and other Bioproducts. In *Lyophilization of Biopharmaceuticals*; Costantino, H. R., Pikal, M. J., Eds., American Association of Pharmaceutical Scientists: Arlington, 2004; 139–229.
22. Hawe, A.; Frieß, W. Impact of Freezing Procedure and Annealing on the Physic-Chemical Properties and the Formation of Mannitol Hydrate in Mannitol-Sucrose-NaCl Formulations. *Eur. J. Pharm. Biopharm.* **2006**, *64*(3), 316–325.
23. Mehta, M.; Bhardwaj, S. P.; Suryanarayanan, R. Controlling the Physical Form of Mannitol in Freeze-Dried Systems. *Eur. J. Pharm. Biopharm.* **2013**, *85*(2), 207–213.
24. Telang, C.; Yu, L.; Suryanararyanan, R. Effective Inhibition of Mannitol Crystallization in Frozen Solutions by Sodium Chloride. *Pharm. Res.* **2003**, *20*(4), 660–667.
25. Larsen, H. M. L.; Trnka, H.; Grohganz, H. Formation of Mannitol Hemihydrate in Freeze-Dried Protein Formulations-A Design of Experimental Approach. *Int. J. Pharm.* **2014**, *460*, 45–52.
26. Cavatur, R. K.; Vemuri, N. M.; Pyne, A.; Chrzan, Z.; Toledo-Velsquez, D.; Suryanarayanan, R. Crystallization Behavior of Mannitol in Frozen Aqueous Solutions. *Pharm. Res.* **2002**, *19*(6), 894–900.
27. Pyne, A.; Surana, R.; Suryanararyanan, R. Crystallization of Mannitol Below Tg' During Freeze-Drying in Binary and Ternary Aqueous Systems. *Pharm. Res.* **2002**, *19*(6), 901–908.

28. Abreu, F. R.; Campana-Filho, S. P. Characteristics and Properties of Carboxymethylchitosan. *Carbohydr Polym.* **2009**, *75*(2), 214–221.
29. Ragnhild, J.; Hjerde, N.; Varum, K. M.; Grasdalen, H.; Tokura, S.; Smidsrod, O. Chemical Composition of *O*-(Carboxymethyl)-chitins in Relation to Lysozyme Degradation Rates. *Carbohydr. Polym.* **1997**, *34*(3), 131–139.
30. Chen, X.-G.; Park, H.-J. Chemical Characteristics of *O*-carboxymethyl Chitosans Related to the Preparation Conditions. *Carbohydr. Polym.* **2003**, *53*(4), 355–359.
31. Weinghold, M. X.; Sauvageau, J. C. M.; Keddig, N.; Matzke, M.; Tartsch, B.; Grunwald, I.; Kübel, C.; Jastorff, B.; Thöming, J. Strategy to Improve the Characterization of Chitosan for Sustainable Biomedical Applications: SAR Guided Multi-Dimensional Analysis. *Green Chem.* **2009**, *11*(4), 498–509.
32. Filipe, V.; Hawe, A.; Jiskoot, W. Critical Evaluation of Nanoparticle Tracking Analysis (NTA) by NanoSight for the Measurement of Nanoparticles and Protein Aggregates. *Pharm. Res.* **2010**, *27*(5), 796–810.
33. Gruia, F.; Parupudi, A.; Polozova, A. Practical Considerations for Detection and Characterization of Sub-Micron Particles in Protein Solutions by Nanoparticle Tracking Analysis. *PDA J. Pharm. Sci. Tech.* **2016**, *69*(3), 427–439.
34. Gross, J.; Sayle, S.; Karow, A. R.; Bakowsky, U.; Garidel, P. Nanoparticle Tracking Analysis of Particle Size and Concentration Detection in Suspensions of Polymer and Protein Samples: Influence of Experimental and Data Evaluation Parameters. *Eur. J. Pharm. Biopharm.* **2016**, *104*, 30–41.

35. Rampino, A.; Borgogna, M.; Blasi, P.; Bellich, B.; Cesàro, A. Chitosan Nanoparticles: Preparation, Size Evolution and Stability. *Int. J. Pharm.* **2013**, *455*(1–2), 219–228.
36. Pikal, M. J.; Shah, S. The Collapse Temperature in Freeze Drying: Dependence on Measurement Methodology and Rate of Water Removal from the Glassy Phase. *Int. J. Pharm.* **1990**, *62*(2–3), 165–186.
37. Lueckel, B.; Bodmer, D.; Helk, B.; Leuenberger, H. Formulations of Sugars with Amino Acids or Mannitol-Influence of Concentration Ratio on Properties of the Freeze-Concentrate and the Lyophilizate. *Pharm. Dev. Technol.* **1998**, *3*(3), 325–336.
38. Ablett, S.; Izzard, M. J.; Lillford, P. J. Differencial Scanning Calorimetric Study of Frozen Sucrose and Glycerol Solutions. *J. Chem. Soc., Faraday Trans.* **1992**, *88*, 789–794.
39. Izzard, M. J.; Ablett, S.; Lillford, P. J.; Hill, V. L.; Groves, I. F. A Modulated Differential Scanning Calorimetric Study: Glass Transitions Occurring in Sucrose Solutions. *J. Therm. Anal. Calorim.* **1996**, *47*(5), 1407–1418.
40. Hawe, A., Friess, W. Physicochemical Characterization of the Freezing Behavior of Mannitol-Human Serum Albumin Formulations. *AAPS Pharm. Sci. Tech.* **2006**, *7*(4), E1–E9.
41. Williams, N.; Dean, T. Vial Breakage by Frozen Mannitol Solutions: Correlation with Thermal Characteristics and Effect of Stereoisomerism, Additives and Vial Configuration. *J. Parent. Sci. Technol.* **1991**, *45*(2), 94–100.

42. Pyne, A.; Chatterjee, K.; Suryanarayanan, R. Solute Crystallization in Mannitol-Glycine Systems--Implications on Protein Stabilization in Freeze-Dried Formulations. *J. Pharm. Sci.* **2003**, *92*(11), 2272–2283.
43. Nakagawa, K.; Murakami, W.; Andrieu, J.; Vessot, S. Freezing Step Controls the Mannitol Phase Composition Heterogeneity. *Chem. Eng. Res. Des.* **2009**, *87*, 1017–1027.
44. Kim, A.; Akers, M.; Nail, S. The Physical State of Mannitol after Freeze-Drying: Effect of Mannitol Concentration, Freezing Rate and a Noncrystallizing Cosolute. *J. Pharm. Sci.* **1998**, *87*(8), 931–935.
45. Chang, Z.; Baust, J. G. Physical Aging of the Glassy State: Sub-$T_g$ Ice Nucleation in Aqueous Sorbitol Solution. *J. Non-Cryst. Solids* **1991**, *130*, 198–203.
46. Hawe, A.; Frieß, W. Physico-Chemical Lyophilization Behavior of Mannitol, Human Serum Albumin Formulations. *Eur. J. Pharm. Sci.* **2006**, *28*(3), 224–232.
47. Burger, A.; Henck, J.; Hetz, S.; Rollinger, J.; Weissnicht, A.; Stottner, H. Energy/Temperature Diagram and Compression Behavior of the Polymorphs of D-Mannitol. *J. Pharm. Sci.* **2000**, *89*(4), 457–468.
48. Dixon, D.; Tchessalov, S.; Barry, A.; Warne, N. The Impact of Protein Concentration on Mannitol and Sodium Chloride Crystallinity and Polymorphism upon Lyophilization. *J. Pharm. Sci.* **2009**, *98*(9), 3419–3429.
49. Haikala, R.; Eerola, R.; Tanninen, V. P.; Ylirruusi, J. Polymorphic Change of Mannitol During Freeze- Drying: Effect of Surface-Active Agents. *PDA J. Pharm. Sci. Tech.* **1997**, *51*(2), 96–101.

50. Cannon, A.; Trappler, E. The Influence of Lyophilization on the Polymorphic Behavior of Mannitol. *PDA J. Pharm. Sci. Tech.* **2000**, *54*(1), 13–22.
51. Hottot, A.; Vessot, S.; Andrieu, J. A Direct Characterization Method of the Ice Morphology. Relationship between Mean Crystals Size and Primary Drying Times of Freeze-Drying Processes. *Drying Technol.* **2004**, *22*(8), 2009–2021.
52. Searles, J. A.; Carpenter, J. F.; Randolph, T. W. Annealing to Optimize the Primary Drying Rate, Reduce Freezing-Induced Heterogeneity, and Determine T(g)' in Pharmaceutical Lyophilization. *J. Pharm. Sci.* **2001**, *90*(7), 872–887.
53. Anhorn, M. G.; Mahler, H.-C.; Langer, K. Freeze Drying of Human Serum Albumin (Has) Nanoparticles with Different Excipients. *Int. J. Pharm.* **2008**, *363*(1–2), 162–169.
54. Carpenter, J. F.; Pikal, M. J.; Chang, B. S.; Randolph, T. W. Rational Design of Stable Lyophized Protein Formulations: Some Practical Advice. *Pharm. Res.* **1997**, *14*(8), 969–975.

# CHAPTER 3

# Carboxymethyl Chitosan (CMCS) Nanoparticles for Mucosal Vaccination Against Rabies: Evaluation of the Immune Response Following Oral Immunization Studies in Mice

## 1. INTRODUCTION

Vaccination has been one of the most effective approaches of preventing disease, and it is also the most cost-effective way to prevent morbidity and economic losses caused by infectious diseases [1]. Safety issues, however, like systemic and local adverse effects and possible recombination of a weakened organism into a virulent specie have increased the interest in subunit or inactivated vaccines. On the other hand, a dramatic decrease in the effectiveness of these vaccines is caused by the lack of virulence factors, generating poor immune responses in general, despite of their safety and better pharmaceutical definition [2]. Therefore, vaccine formulation may be instrumental to successful vaccination.

The oral route can be considered as one of the most comfortable ways for vaccines administration. The benefits over parenteral administration includes reduced side effects, ease of administration, and reduced risk of spread of infectious pathogens via contaminated syringes [3]. All these benefits result in better patient compliance and lower costs. However, in case of subunit or inactivated vaccines, the oral route exhibits several inadequacies due to the high acidity of stomach and the enzymatic attack in the intestinal tract [4]. Therefore, in order to obtain high immune responses via oral route, an adjuvant/delivery system is necessary to make oral immunizations more effective.

Encapsulation of the antigen into particulate carrier systems has been explored extensively in recent years and holds great promise as particles can be specifically designed to meet the challenges that oral vaccination offers. The potential of nanoparticles as vaccine delivery systems has been shown in several studies [4, 5, 6, 7].

The advantages of this kind of system include its ability to cross biological barriers to delivery drugs or macromolecules in a controlled manner, and to prevent peptides, proteins, or genes from decomposition in biological media. Association of the vaccines with particulate systems may stimulate antigen transport to the Peyer's patches increasing the immune response after its administration via mucosal route [8].

The mucosal epithelium as well as distal mucosal surfaces of the gut associated lymphoid tissue (GALT) contains antigen specialized antigen-sampling cells known as the M cells. These cells may represent an efficient potential portal for oral vaccine delivery, due to their ability to transport antigens from the mucosal surfaces into the lymphoid tissues. After entering into the mucosal associated lymphoid tissue (MALT), the antigens are processed by antigen presenting cells such as macrophages, dendritic cells, and presented to B cells and T cells located in this tissue [9]. For mucosal immunization, chitosan, alginates and PLGA are used as delivery systems generally [4, 5, 6, 7].

Due to their biocompatibility, biodegradability and non-toxicity, natural polysaccharides are widely being studied as biomaterials for drug delivery applications [10]. Because of its low cost, biodegradability, biocompatibility, mucoadhesivity, and immuno-adjuvant properties, chitosan, the deacetylated form of chitin (poly-β-(1→4)-*N*-acetyl-D-glucosamin) prepared by alkaline *N*-deacetylation of chitin has a great potential to be used as a delivery system for antigens by mucosal surfaces [15, 16]. Chitosan nanoparticles has shown effective endocytotic uptake and low cytotoxicity using different cell models [13, 14].

However, limited colloidal stability, uncontrollable degradability, and the limited solubility in water or at pH higher than chitosan pKa (pH 5.5-6.5) has prevented its full exploitation in the drug delivery field, whereas chitosan derivatives offer a better solubility at neutral pH values [15, 16, 17]. The reactive hydroxyl groups in both chitin and chitosan, and amino groups in chitosan, can be used for synthetizing several derivatives. Carboxyl groups can be introduced to the hydroxyl and/or amino groups of chitosan to enhance its solubility in water at neutral pH [18]. The biological safety of CMCS has been well established in vitro models, blood systems and tumor application [19, 20, 21]. Additionally, the excellent biodegradability of CMCS in vitro and in vivo has been demonstrated experimentally in rats [22]. Furthermore, the inherent absorption enhancing and mucoadhesive properties of chitosan are retained in CMCS which is extremely favorable for delivery applications. Therefore, the positive biopharmaceutical and toxicological profile of CMCS has encouraged its application in the drug delivery field [17].

The major challenge that limits the use of such carriers is their instability in an aqueous medium. Aggregation and particle fusion are frequently noticed after a long period of storage of these systems. Furthermore, polymer hydrolysis and drug leakage out of the particles can happen. Thus, the stabilization of colloidal vectors is deeply explored to reach a shelf-life of several years [23]. For stabilization of nanoparticles, freeze-drying is a commonly used process, and is considered to be an attractive way to achieve long-term stability with the advantage of easy handling [23, 24, 25]. Also termed lyophilization, freeze-drying is an industrial process of drying by freezing and sublimation of ice under vacuum

and it is used to convert solutions of labile materials into solids of sufficient stability for distribution and storage [26].

## 2. OBJECTIVES

The purpose of this study was to develop a stable antigen/protein delivery system for oral immunization using a negatively charged chitosan derivative (CMCS) and assess its efficacy in vivo. Inactivated rabies virus was chosen as the model antigen.

## 3. MATERIALS AND METHODS

### 3.1. Materials

Chitosan (Deacetylation degree > 75 – 90%, Mol. Wt.: 700 kDa) was purchased from Farma Service Bioextract, Brazil. Purified rabies virus (RV) was kindly provided by Instituto Butantan (Sao Paulo, Brazil). It was found that the rabies virus suspension corresponds to approximately 837 ug/ml of protein using bovine serum albumin (BSA) as a reference, in BCA assay (Novagen, USA). All other chemicals were reagent grade chemicals. All animal experiments were approved by the Ethical Committee for Laboratory Animals of Sao Paulo University in Sao Paulo, Brazil.

### 3.2. Synthesis of CMCS

The synthesis of carboxymethyl chitosan was performed as previously reported [27] with minor modifications. Briefly, chitosan (3 g), NaOH 40% (23 g) and solvent (65 ml) were mixed to form slurry and allowed to swell and alkaline at 25$^{o}$C for 10 min. Then, a solution of chloroacetic acid (17.5 g) dissolved in

isopropanol (20 ml) was prepared. The solution of chloroacetic acid was added slurry drop-wise at regular intervals followed by continuous stirring at 25°C for 12 h. The reaction was stopped by adding 70% ethanol to the reaction mixture. The solution was filtered and washed with 70% ethanol four times and dehydrated with absolute alcohol. Finally, the product obtained was dialyzed for 5 days to remove impurity and freeze-dried to obtain the cotton-like product.

### 3.3. Characterization of the chitosan derivative

CMCS was characterized by nuclear magnetic resonance (NMR) spectroscopy, and the degree of substitution was determined by $^{1}H$ NMR on a 600 MHz spectrometer (Bruker, Germany) as previously reported [28]. The degree of carboxymethylation of the chitosan chains was found to be 0.70.

### 3.4. Preparation of CMCS nanoparticles

CMCS nanoparticles were prepared according to a method previously reported [29] based on ionotropic gelation of CMCS with $Ca^{2+}$ cations from CaCl2 as a cross-linker. RV-CMCS Nps were formed spontaneously upon addition of an aqueous solution of $CaCl_2$ (10 mg/ml) to a CMCS solution (3 mg/ml) under magnetic stirring for 1 h at 750 rpm resulting in the formation of a turbid suspension. For association of RV with CMCS nanoparticles, RV was incorporated in the $CaCl_2$ solution to a final concentration of 40 µg/ml. RV-CMCS Nps were isolated by centrifugation at 12000 rpm on a glycerol bed for 30 min. Supernatants were discarded and the pellet was resuspended in MilliQ water to wash the nanoparticles and centrifuged again. After repeating this washing step, the nanoparticles were freeze-dried overnight with mannitol 10% (w/v) [30].

### 3.5. Characterization of nanoparticles

The particle size distribution, polydispersity index, and zeta potential of nanoparticles was measured by using Zetasizer (Malvern Instruments, UK). BCA assay kit (Novagen, USA) was used for the determination of RV surface antigen protein (RVsAg). The loading efficacy was calculated from the difference between the initial amount of protein and the amount present in the supernatant after centrifugation with the BCA assay method. The loading efficacy (LE) was determined as follows:

$$LE\ (\%) = \frac{\text{total amount of RVsAg} - \text{free RVsAg}}{\text{total amount of RVsAg}} \times 100$$

### 3.6. Freeze-drying cycle

The lyophilization of the nanoparticles was performed using a pilot freeze-dryer Dura-Stop MP Dura-Top MP Tray Dryer MNL-031-A (New York, USA). 2 ml of nanoparticles suspension were dispensed into 10 ml freeze-drying molded vials. The conditions applied during the present study were: (1) freezing to –50°C with a temperature ramp of 2.5°C/min and holding for 30 min; (2) primary drying performed at –40°C for 6 h and finally (3) secondary drying was carried out at a shelf temperature of 20°C for 4 h. In addition, an annealing procedure was applied, i.e., the suspensions were frozen at –50°C (cooling rate of 1°C/min), and then annealing was performed at –15°C for 1 h. Finally, the samples were cooled again to –50°C and lyophilized under the conditions mentioned above. To determine the end of the sublimation step, the partial pressure of water in the freeze-drying chamber was measured by a hygrometer. The chamber pressure

was maintained at 10 mTorr during the drying process and a thermocouple was placed into a vial to monitor de sample temperature. At the end of the lyophilization the vials were stoppered under vacuum which was subsequently broken by injection of nitrogen gas. All the conditions performed, including excipients and their concentration, were optimized in a previous study carried out by our research group that sought to obtain parameters that ensure the stability of the formulation [30].

### 3.7. Freeze-drying microscopy

The collapse temperature (Tc) of the nanoparticles suspension was measured by a freeze-drying microscope (Linkam Scientific Instruments, Surrey, UK) equipped by a video camera, a computer to capture the collapse image (optical window), a nitrogen cooling system, a vacuum pump and a small freeze-drying chamber with a temperature controller. Direct observation of the freeze-dried sample was done by using a polarized microscope (Nikon Elipse E600, Nikon, Japan). The samples were cooled at 2.5ºC/min to –50ºC, kept at –50ºC for 1 min, and then heated to 25ºC at 5ºC/min under vacuum at about 0.1 Pa. Additionally, the annealing procedure was applied, i.e., an annealing step at –15°C for 5 min was added after the freezing step. The collapse temperature corresponds to the lowest temperature of overall loss of the initial frozen structure during freeze-drying.

### 3.8. Differential scanning calorimetry

The thermal behavior of the nanoparticles suspension was studied through differential thermal analysis using a Perkim Elmer Pyris DSC model Pyris 1

instrument (Norwallk, CT, USA) equipped with a cooling system (CryoFill, Perkim Elmer). It was calibrated using indium, mercury, and distilled water as standards. Approximately 15 μl of suspension was weighed in an aluminum pan and sealed. An empty pan was used as the reference. The suspension was cooled to –50°C at 2.5°C/min, held for 1 min and then heated to 25°C at 10°C/min. Additionally, the annealing procedure was applied, i.e., an annealing step at –15°C for 5 min was added after the freezing step. The second heating scan (to 25°C) was used to determine the glass transition temperature ($T'_g$).

### 3.9. Immunization studies

#### 3.9.1. Animals

For immunization studies RV loaded CMCS nanoparticles were administered intragastrically (i.g.) to male Balb/c mice aged up to 6-8 weeks and weighing about 25 g. Animals were housed for acclimatization 1 week before the experiments at the animal resource facility of the Faculty in accordance with institutional ethical guidelines. Animals were maintained on a normal diet throughout the study.

#### 3.9.2. Treatment groups

- Group I: CMCS nanoparticles loaded with 10 μg RVsAg (i.g.)
- Group II: Empty CMCS nanoparticles (i.g.)
- Group III: saline solution of 0.9% NaCl (i.g.)
- Group IV: suspension of 10 μg RVsAg intraperitoneally (i.p.)

### 3.9.3. Immunization schedule

The different formulations, corresponding to each treatment group except to group IV were administered intragastrically with a gavage-feeding needle (see section 2.9.2). Mice were vaccinated on days 0, 14, and 21, i.e. on weeks 1, 3, and 4. They received 250 μl volume per week containing 10 μg of the RVsAg, which corresponds to approximately 0.1 UI per dose. The animals were sacrificed 7 days after the last immunization, and a collection of blood from the ophthalmic venous plexus and saliva was carried out for analysis as described in the following section.

### 3.9.4. Collection of samples

To assess immune responses, blood samples taken from the ophthalmic venous plexus were collected on days 21 (week 4) and 28 (week 5). The blood samples were centrifuged at 4°C for 20 min at 10,000 rpm in an eppendorf centrifuge, and the serum was collected and stored at –20°C until analysis for IgG titres. Saliva samples were collected on day 28 in an eppendorf centrifuge containing 10 μl of protease inhibitor cocktail and stored at –20°C until analysis for IgA. The mice were anesthetized with a mixture of 20 mg/kg ketamine-HCl (Cetamin 10%, Syntec do Brasil Ltda., Sao Paulo, Brazil) and 10 mg/kg xylazine-HCl (Sedalex 2%, Laboratorios Vencofarma do Brasil Ltda., Sao Paulo, Brazil) i.p. and then injected with 10 mg/kg pilocarpine-HCl (Pilocarpina 1%, Laboratorios Calbos Ltda., Parana, Brazil) i.p. The saliva secreted into the oral cavity was carefully collected using 200 μl pipette.

### 3.9.5. Enzyme-linked immunoabsorbent assay (ELISA)

RV-specific IgG antibodies were measured by an adapted method enzyme-linked immunosorbent assay (ELISA). RV (50 μg/ml in (0.04 M carbonate buffer, pH 9.6)) was adsorbed to 96-wells plate (Costar 3590 EIA/RIA plates, Corning Incorporated, Corning USA) by overnight incubation at 4°C. The plates were washed twice with PBS containing 0.05% Tween 20 (PBS-T) and were blocked with PBS containing 0.5% milk caseine for 2 h at 25°C (150 μl/well). After washing with PBS-T, serial 2-fold dilutions of test mouse serum in PBS containing 0.05% BSA and 0.05% milk caseine were titrated across the plate, to a final volume of 100 μl/well. Plates were incubated for 2 h at 25°C. At the end of the incubation period, plates were washed with PBS-T and were incubated with 100 μl/well of peroxidase-conjugated goat-anti-mouse IgG (Sigma, USA) diluted 1:1000 with PBS/well, for 2 h at 25°C. Unbound conjugate was removed by washing with PBS-T and enzyme activity was determined by adding 1,2-Phenylenediamine (OPD) (Sigma, USA) and 10 μl of hydrogen peroxide solution (30%, m/v) in 0.1 M citric acid buffer (100 μl/well). After 30 min at 25°C the reaction was stopped by adding 50 μl 3 M $H_2SO_4$ to each well. The absorbance was read at 492 nm on an ELISA reader (BioTek, PowerWave XS2 Microplate Spectrophotometer, USA).

### 3.9.6. Rapid Fluorescent Focus Inhibition Test for Rabies Virus-Neutralizing Antibodies (RFFIT)

The RFFIT procedure [31] is utilized to measure the level of rabies virus neutralizing antibody activity (RVNA) against the challenge virus standard 11 (CVS-11) strain of rabies virus in human serum samples. Five-fold serial dilutions

of heat-inactivated serum samples were incubated with the CVS-11 strain in 8-well tissue culture chamber slides for 90 min at 37°C. Baby hamster kidney (BHK)-21C13 cells were then added to the serum-virus mixture and incubated for an additional 20 to 24 h at 37°C with 2 to 5% $CO_2$. Slides were then acetone fixed and stained with an anti-rabies N-FITC conjugate (Biorad, USA). Twenty distinct microscopic fields per well were examined using a fluorescence microscope at x160 magnification to score the virus-infected cells (foci). The number of positive fields with rabies-infected cells per well was recorded. The neutralization endpoint titer was defined as the highest sample dilution at which 50% of the observed microscopic fields contain one or more infected cells. The RVNA titers are mathematically interpolated using the Reed and Muench method or a Reed and Muench chart for assigning a RFFIT titer [32]. The endpoint neutralization titer of the test serum is then transformed into international units (IU)/ml values by calibration against the endpoint neutralization titer of the Standard Rabies Immune Globulin (SRIG) (30 IU; second WHO International Standard), which was measured in the same assay run, with an assigned potency value of 2.0 IU/ml.

### 3.10. Statistical analysis

Statistical significance was assessed using one-way ANOVA following Dunnett's post-test using GraphPad Prism 4 software. Differences were considered significant when $p < 0.001$. It is noteworthy that ELISA results were statistically analyzed by the Effective Dose (ED) method. In this method, a positive reference serum is used to construct a dose-response curve to which the dose-response curve of the test sera is then compared. The major distinction between the ED and the titration method is that the difference between two sera

is expressed by the log of the difference in the dilution at the linear part of the sigmoidal curves, where sensitivity is maximal instead of at the flattening part of the curve [33]. Advantages of this method are the improvement in the reproducibility of the test, which renders possible the detection of subtle seroconversions, and the linear proportionality between the ED results and titres. The results are expressed in Brigg's logs (e.g., for acute phase serum, ED = - 80; for convalescent phase serum ED = 1.07). This method also assumes parallelism of the dose-response curves. In a similar approach, adopted by Soula et al. [34], the titer is expressed as ELISA (50%), obtained after transformation of the sigmoidal curve into a linear response curve.

## 4. RESULTS AND DISCUSSION

### 4.1. Characterization of nanoparticles

Nanoparticles were obtained by ionic crosslinking of carboxyl groups of CMCS chains and $Ca^{2+}$ cations from $CaCl_2$. DLS analysis resulted in a size average of 219 ± 3.8 nm and polydispersity index around 0.137 ± 0.090, which indicates a monodisperse distribution of the nanoparticles with a negative surface charge (–12 mV). The loading efficacy (LE) of RV into CMCS nanoparticles was found to be 17%, and this can be ascribed to the lipid composition (cholesterol/phospholipids) of RV. Studies have demonstrated an elevated level of phosphatidylinositol and phosphatidylserine in RV membrane (27% of total phospholipids), and both types of lipids carry a negative charge. Since the remaining lipid components are either zwitterionic or charge neutral, the high percentage of negative lipids negatively charged confers a negative net charge to the viral surface [ref]. Additionally, the viral envelope is covered by knob-like

spikes composed of trimers of G-glycoprotein, which has a theoretical isoelectric point (pI) of 7.38, i.e., it is negatively charged under the preparation conditions (pH 7). Therefore, in the aqueous neutral system, RV and CMCS have the same charge, which generates an electrical repulsion between RV and CMCS chains under the pH of the synthesis of nanoparticles [ref], suggesting that electrostatic interactions are the main factor to form complexes between CMCS and RV. However, hydrophobic interactions could cause chain entanglement between G-glycoprotein and CMCS towards the formation of nanoparticles, since G-glycoprotein has hydrophobic residues of tyrosine, phenylalanine and tryptofan, and CMCS has hydrophobic moieties such as glucosidic rings and acetyl groups. Moreover, the presence of hydrophilic groups such as hydroxyl and amino groups in the polypeptide backbone of G-glycoprotein and CMCS chains may be another important factor to drive RV loaded CMCS nanoparticles formation through hydrogen bonding [36].

### 4.2. Freeze-drying microscopy

The collapse temperature ($T_c$), defined as the maximum allowable product temperature during primary drying, was found to be around –8$^{o}$C. Collapse and loosening of porous structure can happen when the product is heated above $T_c$ during primary drying step. Figure 1 shows the observation of a sample of CMCS nanoparticles containing mannitol 10% (w/v).

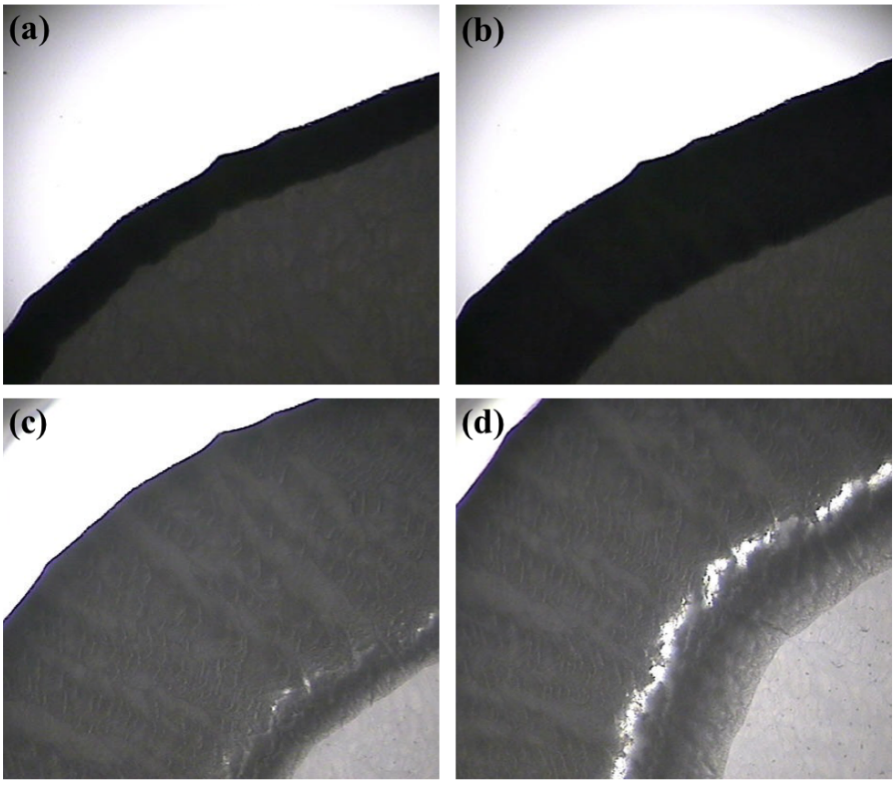


**Figure 1**. Determination of collapse temperature ($T_c$) of RV loaded CMCS nanoparticles suspension with mannitol at 10% (w/v). (a) Frozen and dried region, (b) micro collapse, (c) onset of overall collapse, and (d) overall collapse.

In Fig. 1a and 1b, the drying is performed at –50°C and the sublimation front advances within the frozen matrix. In Fig 1c, the sample is heated to –5.8°C and the small holes begin to appear in the dried portion signaling the microcollapse of the sample. The complete collapse can be observed upon heating to –4.6°C in Fig. 1d. The collapse during the sublimation step can prolong the reconstitution time and increase the residual humidity affecting the product quality [30].

### 4.3. Differential scanning calorimetry

The glass transition temperature ($T'_g$) obtained by DSC was found at –29.46°C. The primary drying, the most time-consuming stage of the

lyophilization process, should be performed at a maximum allowable temperature. The comparison between $T'_g$ and $T_c$ values pointed out to a behavior dependent on the nature of the bulking agent used. These results are in agreement with Passot et al., [37] that found widely lower $T'_g$ values for formulations involving any crystallized solute. According to Passot et al., $T_c$ can be defined as a more relevant parameter than $T'_g$ for freeze-drying development and optimization, once formulations involving crystalline bulking agents such as glycine or mannitol where freeze-dried at a product temperature higher than $T'_g$ but lower than $T_c$ and provided high storage stability. Additionally, the primary drying time could be significantly reduced if the $T_c$ is used to fix the product temperature during the sublimation step. Pikal and Shah [38] found a 13% reduction of sublimation time when the product temperature was increased by 1°C.

### 4.4. *In vivo* studies

The purpose of this study was to develop an antigen delivery system for oral immunization using a chitosan carboxymethylated derivative (CMCS) and assess its efficacy *in vivo*. Inactivated rabies virus was used as the model antigen. It has been suggested that the immune response to antigens administered by oral route is initiated in the gut locally, and then disseminated to the lymph nodes and spleen, while others suggest activation of antigen-specific T cells after feeding the antigen to the animals [39]. Thus, it was investigated if a short intragastric vaccination scheme was able to elicit not only systemic but also a mucosal immune response.

The first vaccination experiment was performed to investigate if RV loaded CMCS nanoparticles are able to induce systemic immune response following intragastric administration to mice, and also to establish if CMCS by itself (i.e. empty nanoparticles) interferes with RV specific IgG immune responses.

Increased RV specific serum IgG effective doses 50% were obtained with RV loaded CMCS Nps (Group I) administered intragastrically to mice compared to control groups (II and III), i.e., suspension of empty CMCS nanoparticles and saline solution of 0.9% NaCl respectively. Following intragastric administration of RV loaded CMCS nanoparticles, low RV specific serum IgG effective doses 50% could be found in weeks 1 – 4 (Fig. 2).

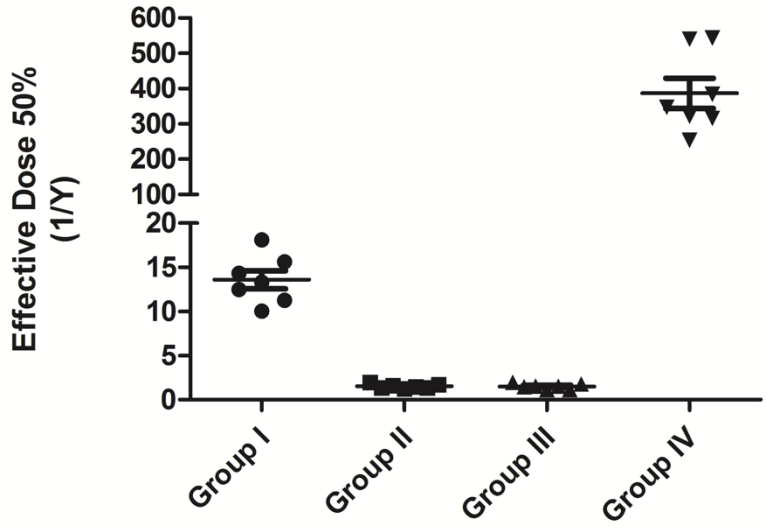


**Figure 2**. RV specific serum IgG effective dose 50% 7 days after the second boosting dose (week 4) following intragastric vaccination with suspension of CMCS nanoparticles loaded with 10 μg RVsAg (Group I), suspension of empty CMCS nanoparticles (Group II), saline solution of 0.9% NaCl (Group III), and suspension of 10 μg RVsAg intraperitoneally (Group IV), in mice. Effective doses 50% are expressed as mean ± SEM. ****P*< 0.05 Group I, II, and III vs. suspension of 10 μg RVsAg (i.p.) (ANOVA following Bonferroni's Multiple Comparison Test).

However, highly elevated serum IgG effective dose 50% was measured in week 5 (Fig 3). These t effective doses 50% were 50-times higher than the negative controls. Therefore, it seems that the immune response started only after the third boosting (week 4), indicating the formation of memory cells after the second bosting dose (week 3). Similarly, following boosting, enhanced immune responses for various other antigens were reported with chitosan and its carboxymethylated derivatives-based formulations [4, 5, 6, 7, 40].

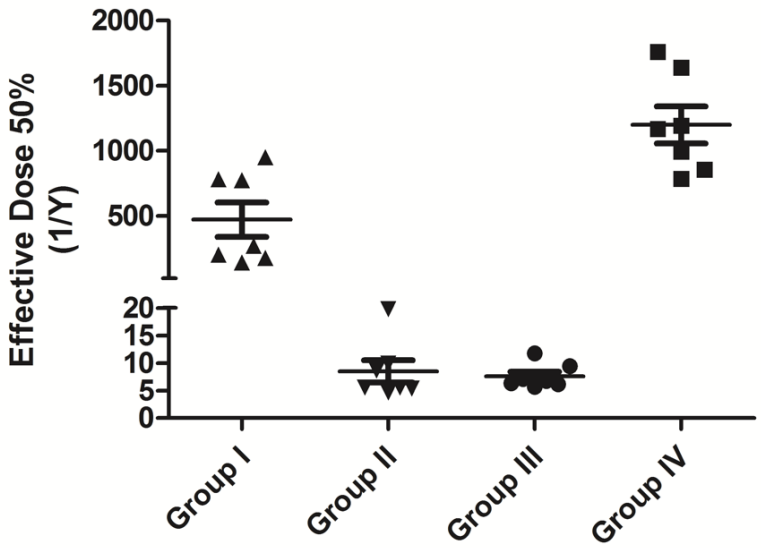


**Figure 3**. RV specific serum IgG effective dose 50% 7 days after the third boosting dose (week 5) following intragastric vaccination with suspension of CMCS nanoparticles loaded with 10 μg RVsAg (Group I), suspension of empty CMCS nanoparticles (Group II), saline solution of 0.9% NaCl (i.g.) (Group III), and suspension of 10 μg RVsAg intraperitoneally (Group IV), in mice. Effective doses 50% are expressed as mean ± SEM. ****P*< 0.05 Group I, II, and III vs. suspension of 10 μg RVsAg (i.p.), **P*< 0.05 Group I vs. suspension of empty CMCS nanoparticles, and **P*< 0.05 Group I vs. saline solution of 0.9% NaCl (ANOVA following Bonferroni's Multiple Comparison Test).

The higher humoral immune responses elicited by antigen-loaded nanoparticles are most likely based on cellular uptake of the nanoparticles in the mucosal epithelium and GALT and subsequent access of the antigen to submucosal lymphoid tissues [41]. RV loaded CMCS Nps resulted in significantly higher levels ($p < 0.05$) of serum IgG effective doses 50% than that obtained with empty CMCS nanoparticles, although a minor IgG effective dose 50% was observed with empty nanoparticles. It was demonstrated that besides enhancing the immune responses by opening the tight junctions or stimulating the uptake by M-cells, chitosan may also specifically stimulate the immune system [42]. Bacon et al. [43] found that chitosan in solution (PBS) significantly enhances the systemic and also the local immune response against influenza virus after nasal co-administration with a solution of chitosan. Similarly, Jabbal-Gill et al. [44] showed that a mixture of *Bordetella pertussis* filamentous haemagglutinin (FHA) and recombinant pertussis toxin, (rPT) in combination with chitosan induced systemic and also mucosal responses for both antigens in mice intranasally immunized. Both the systemic and mucosal responses were higher than those produced with a mixture of rPT and FHA administered nasally without chitosan.

Nasal vaccines can be directly target to the mucosal surfaces, therefore, it was expected that these formulations would be efficient in the enhancement of immune responses by the simply mixture of the antigens with a chitosan solution. However, with the present CMCS formulation, increased specific IgG anti-RV titers were obtained in mice intragastrically immunized demonstrating that CMCS-based nanoparticles may be very potent as an oral delivery system.

It is noteworthy that in case of intragastric delivery, the vaccines are exposed to the acidic environment in the stomach and enzymes in the gut and

therefore are more susceptible to degradation. Additionally, they need to be taken by the M-cells of the follicle-associated epithelium, which covers the Peyer's patches [45]. Furthermore, while the negatively charged glycocalyx on the apical membrane of mucosal cells can strongly interact with positively charged biopolymers such as chitosan, this cannot take place with the negatively charged CMCS nanoparticles, which can be explained by a bioadhesion mechanism, since the molecular interactions such as the electrostatic, hydrophobic interactions, hydrogen bonding forces, and van der Waals can affect the interactions between the mucin network and the bioadhesive polymer. In addition, the repulsive electrostatic forces would reduce the overall mucoadhesive strength [40].

The use of chitosan derivatives such as CMCS as a strategy to improve the response the response to intragastrically antigens is likely to be governed mainly by its immunostimulant and absorption enhancer effect improving the contact of the antigen with intraepithelial and submucosal lymphocytes independent of any pH effects. The crucial interactions that contribute to the formation and stability of CMCS nanoparticles are the interactions between $-NH_3^+$ and $-COO^-$ groups, and between carboxyl groups and $Ca^{2+}$ ions, and the increased stability in near neutral pH (as-synthesized solutions) is attributed to the interactions between $-NH_3^+$ and $-COO^-$ groups in CMCS, which is stronger in neutral pH due to the increased amount of protonated $-NH_3^+$, resulting in more stable nanoparticles. Therefore, the nanoparticles are fundamentally unstable in solution, if the pH deviates from (7-9) that is used in the synthesis of the nanoparticles [46].

The suspension of 10 μg RVsAg administered intraperitoneally (Group IV) was found to induce a higher systemic immune response than the group

vaccinated intragastrically with RV loaded CMCS Nps. In spite of the fact that an enhanced systemic antibody response was obtained with RVsAg administered intraperitoneally, this was not observed for the local antibody levels. Local sIgA antibodies analyzed in saliva 7 days after the third boosting dose (week 5) were found to be significantly higher ($p < 0.05$) with RV loaded CMCS Nps following intragastric administration (Fig. 4).

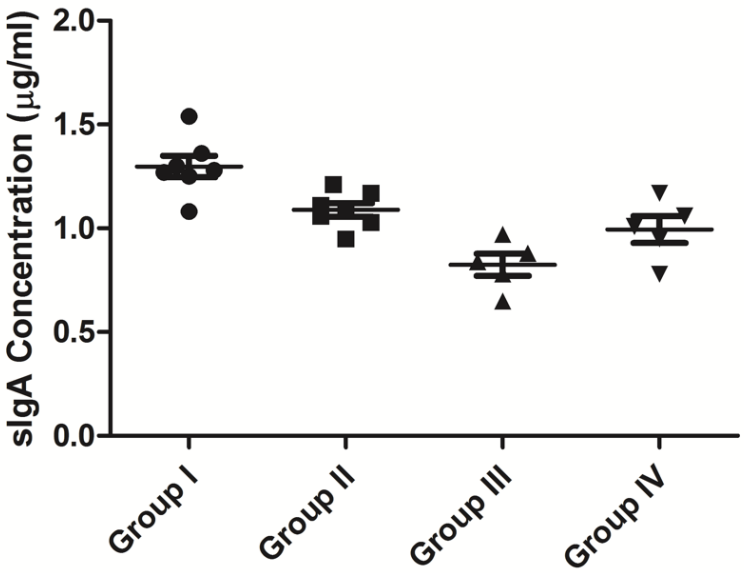


**Figure 4**. sIgA concentrations in saliva 7 days after the third boosting dose (week 5) following intragastric vaccination with suspension of CMCS nanoparticles loaded with 10 μg RVsAg (Group I), suspension of empty CMCS nanoparticles (Group II), saline solution of 0.9% NaCl (Group III), and suspension of 10 μg RVsAg intraperitoneally (Group IV), in mice. sIgA concentrations are expressed as mean ± SEM. ****P*< 0.05 Group I vs. saline solution of 0.9% NaCl, ***P*< 0.05 Group I vs. suspension of 10 μg RVsAg (i.p.), ***P*< 0.05 Group II vs saline solution of 0.9% NaCl, and **P*< 0.05 Group I vs. suspension of empty CMCS nanoparticles, (ANOVA following Bonferroni's Multiple Comparison Test).

On the other hand, Kim et al. [5] showed that VP6-specific IgA was detected in culture supernatants of mesenteric lymph nodes (LN) from mice immunized intraperitoneally with either VP6-IFA (porcine rotavirus recombinant protein in incomplete Freud's adjuvant) or with PRV-IFA (live porcine rotavirus in incomplete Freud's adjuvant). Moreover, the VP6-specific fecal IgA antibody was boosted by a secondary intraperitoneal immunization with VP6 in mice previously immunized orally with VP6 encapsulated in alginate microspheres. The authors suggest that intraperitoneal injection of porcine rotavirus or native protein drains to the mesenteric lymph node, inducing IgA responses in this site, and then that effector lymphocytes would disseminate to the intestinal tract, explaining the detection of IgA in animal feces.

Besides reduction of costs, especially those related to the cold chain transport, since the present formulation is lyophilized and can therefore be stored at room temperature [30], and increased patient compliance, the induction of a local immune response is an important feature of CMCS nanoparticles as oral vaccine carriers, since pathogens can be neutralized during the invasion through the mucosae because of the production of IgA at mucosal sites. Although for a rabies virus vaccine delivery, the main aim is to enhance the systemic immune response, the formulation developed using CMCS could bring advantages when used as a delivery system for vaccines against pathogens that affect the gastrointestinal tract such as *Corynebacterium diphtheriae*, rotavirus, *Clostridium botulinum*, *Staphylococcus aureus*, and *Samonella spp*.

Interestingly, Izaguirre-Hernández et al. [47] found that chitosan nanoparticles simply mixed with BSA or E protein from Dengue virus serotype 2 (E protein DENV2) elicited robust specific primary and secondary humoral

responses comparable to alum, in mice immunized intraperitoneally. Moreover, for both antigens, the simply combination with chitosan nanoparticles polarized the response to a Th2-like profile, which is characterized mainly by the production of the IgG1 isotype, confirming that chitosan nanoparticles can enhance and also modulate the humoral immune responses against different antigens with no need of physicochemical conjugation.

The RFFIT procedure was performed to determine if the anti-RV IgG in serum is effective in neutralizing the actual rabies virus. Mice intragastrically vaccinated with RV associated to CMCS nanoparticles and mice intraperitoneally vaccinated with RV suspension produced high concentrations of RV neutralizing antibodies (Fig. 5).

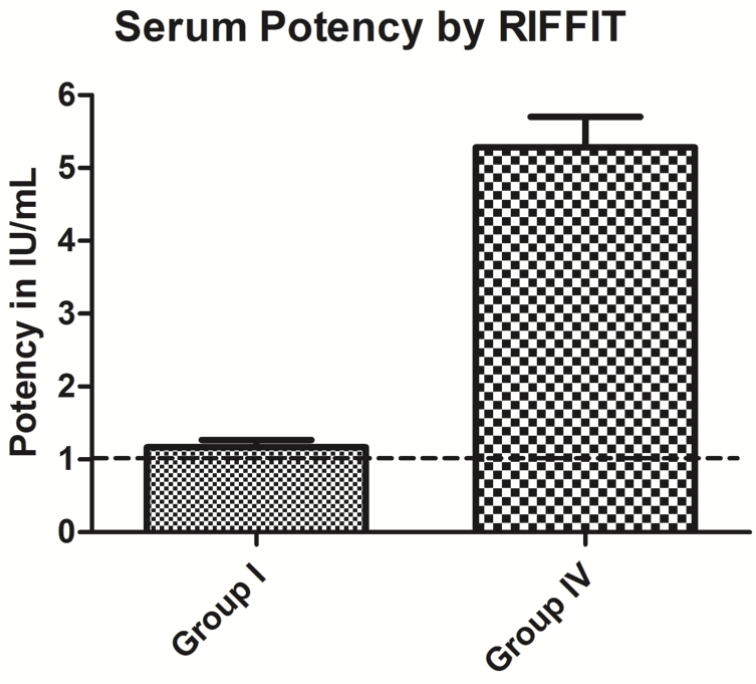


**Figure 5**. Rabies virus neutralizing antibodies concentration in serum 7 days after the third boosting dose (week 5) following intragastric vaccination with suspension of CMCS nanoparticles

loaded with 10 μg RVsAg (Group I) and suspension of 10 μg RVsAg intraperitoneally (Group IV), in mice. Serum potencies are expressed as mean ± SD.

No anti-RV could be measured in mice vaccinated intragastrically with empty CMCS nanoparticles or with saline solution of 0.9% NaCl. Since all mice vaccinated with RV associated to CMCS nanoparticles produced enough neutralizing antibodies (not less than 1.0 IU per dose on OIE recommendation) to be protect against the deleterious effects of the rabies virus, it is concluded that RV associated to the present vaccine carrier system not only enhances immune responses, but also protects during actual infections.

Encapsulation of RV into CMCS nanoparticles would protect the antigen from the potential undesired environment at the gastrointestinal tract and also prevent the loss of antigen before reaching the M-cells within the delivery system. Moreover, the longer retention time of the nanoparticles would allow efficient uptake of antigen through the mucosa thus improving the immune response. Besides, preparation of chitosan and its derivatives such as CMCS do not need any organic solvents making these nanovehicles more attractive and safer compared to those produced with polymers that require organic solvents for fabrication. In addition, there is no need for protein stabilizers.

## 5. CONCLUSION

In this study, RV loaded nanoparticles were prepared using the chitosan derivative CMCS and their potential as a delivery system for mucosal immunization was investigated *in vivo*. The nanoparticle system prepared by CMCS can be stabilized during freeze-drying process using mannitol 10% (w/v) and was found to enhance both systemic (IgG) and local (IgA) immune responses

against RV after oral delivery in mice. Furthermore, enough neutralizing antibodies was produced to be protected against the harmful effects of the rabies virus. It is therefore concluded, that the CMCS nanoparticles formulated in this study, are suitable for oral vaccine delivery, and can be suggested as a promising delivery system for a diverse range of antigens as well as a gene/protein delivery system, especially for those positively charged, for a better loading efficacy.

## 6. REFERENCES


1. Wack A, Rappouli R. Vaccinology at the beginning of the 21st century. Curr Opin Immunol 2005;17:411–8.
2. Huang DB, Wu JJ, Tyring SK. A review of licensed viral vaccines, some of their safety concerns, and the advances in the development of investigacional viral vaccines. J Infect 2004;49:179–209.
3. Ryan EJ, Daly LM, Mills KHG. Immunomodulators and delivery systems for vaccination by mucosal routes. Trends Biotechnol 2001;19:293–304.
4. Hori M, Onishi H, Machida Y. Evaluation of Eudragit-coated chitosan microparticles as an oral immune delivery system. Int J Pharm 2005;297:223–34.
5. Kim B, Bowersock T, Griebel P, Kidane A, Babiuk LA, Sanches M, et al. Mucosal immune responses following oral immunization with rotavirus antigens encapsulated in alginate microspheres. J Control Rel 2002;85:191–202.
6. van der Lubben IM, Kersten G, Fretz MM, Beuvery C, Verhoef JC, Junginger HE. Chitosan microparticles for mucosal vaccination against diphtheria: oral and nasal efficacy studies in mice. Vaccine 2003;21:1400–8.

7. Borges O, Tavares J, de Souza A, Borchard G, Junginger HE, Cordeiro-da-Silva A. Evaluation of the immune response following a short oral vaccination schedule with hepatitis B antigen encapsulated into alginate-coated chitosan nanoparticles. Eur J Pharm Sci 2007;32:278–290.
8. Borges O, Cordeiro-da-Silva A, Romeijin SG, Amidi M, de Souza A, Borchard G, Junginger HE. Uptake studies in rat Peyer's patches, cytotoxicity and release studies of alginate coated chitosan nanoparticles for mucosal vaccination. J Control Rel 2006;114:348–358.
9. Frey A, Neutra MR. Targeting of mucosal vaccines to Peyer's patch M cells. Behring Inst Mitt 1997;98:376–389.
10. Liu Z, Jiao Y, Wang Y, Zhou C, Zhang Z. Polysaccharides-based nanoparticles as drug delivery systems. Adv Drug Deliv Rev 2008;60:1650–62.
11. Vila A, Sánchez A, Janes K, Behrens I, Kissel T, Jato JLV, Alonso MJ. Low molecular weight chitosan nanoparticles as new carriers for nasal vaccine delivery in mice. European Journal of Pharmaceutics and Biopharmarmaceutics 2004;57:123–131.
12. Jiang H-L, Park I-K, Shin N-R, Kang S-G, Yoo H-S, Kim S-I, et al. In vitro study of the immune stimulating activity of an athrophic rhinitis vaccine associated to chitosan microspheres. Eur J Pharm Biopharm 2004;58:471–6.
13. Behrens I, Vila-Pena AI, Alonso MJ, Kissel T. Comparative uptake studies of bioadhesive and non-bioadhesive nanoparticles in human intestinal cell lines and rats: the effect of mucus on particle absorption and transport. Pharm Res 2002;19:1185–93.

14. Huang M, Khor E, Lim LY. Uptake and cytotoxicity of chitosan molecules and nanoparticles: effects of molecular weight and degree of deacetylation. Pharm Res 2004;21:344–53.
15. de Campos AM, Diebold Y, Carvalho EL, Sánchez A, Alonso MJ. Chitosan nanoparticles as new ocular drug delivery systems: in vitro stability, in vivo fate, and cellular toxicity. Pharm. Res. 2004;21:803–10.
16. Prego C, Paolicelli P, Díaz B, Vicente S, Sánchez A, González-Fernández A. Chitosan-based nanoparticles for improving immunization against hepatitis B infection. Vaccine 2010;28:2607–14.
17. Upadhyaya L, Singh J, Agarwal V, Tewari RP. The implications of recent advances in carboxymethyl chitosan based targeted drug delivery and tissue engineering applications. J Control Release 2014;86:54–87.
18. Upadhyaya L, Singh J, Agarwal V, Tewari RP. Biomedical applications of carboxymethyl chitosans. Carbohydr Polym 2013;91:452–66.
19. El-Sherbiny IM. Enhanced pH-responsive carrier system based on alginate and chemically modified carboxymethyl chitosan for oral delivery of protein drugs: preparation and in-vitro assessment. Carbohydr Polym 2010; 80:1125–36.
20. Fu D, Han B, Dong W, Yang Z, Lv Y, Liu W. Effects of carboxymethyl chitosan on the blood system of rats. Biochem Biophys Res Commun 2011;408:110–4.
21. Zheng M, Han B, Yang Y, Liu W. Synthesis, characterization and biological safety of O-carboxymethyl chitosan used to treat Sarcoma 180 tumor. Carbohydr Polym 2011;86:231–8.

22. Dong W, Han B, Feng Y, Song F, Chang J, Jiang H. Pharmacokinetics and bio- degradation mechanisms of a versatile carboxymethyl derivative of chitosan in rats: in vivo and in vitro evaluation. Biomacromolecules 2010;11:527–33.
23. Abdelwahed W, Degobert G, Fessi H. A pilot study of freeze-drying of poly(epsilon-caprolactone) nanocapsules stabilized by poly(vinyl alcohol): formulation and process optimization. Int J Pharm 2006;309:178–88.
24. Abdelwahed W, Degobert G, Fessi H. Investigation of nanocapsules stabilization by amorphous excipients during freeze-drying and storage. Eur J Pharm Biopharm 2006;63:87–94.
25. Abdelwahed W, Degobert G, Fessi, H. Freeze-drying of nanocapsules: impact of annealing on drying process. Int J Pharm 2006;324:74–82.
26. Abdelwahed W, Degobert G, Stainmesse S, Fessi, H. Freeze-drying of nanoparticles: formulation, process and storage considerations. Adv Drug Deliv Rev 2006;58:1688–1713.
27. Abreu FR, Campana-Filho SP. Characteristics and properties of carboxymethylchitosan. Carbohydr Polym 2009;75:214–21.
28. Chen XG, Park HJ. Chemical characteristics of O-carboxymethyl chitosans related to the preparation conditions. Carbohydr Polym 2003;53:355–59.
29. Kalliola S, Repo E, Srivastava V, Heiskanen JP, Sirvio JA, Liimatainen H, Sillanpaa M. The pH sensitive properties of carboxymethyl chitosan nanoparticles cross-linked with calcium ions. Colloids Surf B Biointerfaces 2017;153:229–36.
30. Bexiga NM, Bloise AC, Alencar AM, Stephano MA. Freeze-drying of ovalbumin-loaded carboxymethyl chitosan nanocapsules: impact of freezing

and annealing procedures on physicochemical properties of the formulation during dried storage. Drying Technol 2018;36:400–17.

31. Smith JS, Yager PA, Baer GM. A rapid reproducible test for determining rabies neutralizing antibody. Bull World Health Organ 1973;48:535–41.
32. Habel K. Habel test for potency. In: Meslin FX, Kaplan MM, Koprowski H (ed), Laboratory techniques in rabies, 4th ed. World Health Organization, Geneva, Switzerland; 1996, p. 369–73.
33. Leinikki PO, Passila S. Evaluation of some of the parameters of the enzyme-linked immunosorbent assay. J Infect Dis 1977;136 (Suppl):294–299.
34. Soula A, Laurent N, Tixier G, Moreau Y. [ELISA of IBR (infectious bovine rhinotracheitis)--an expression of a 50 percent ELISA titer]. Develop Biol Stand 1982;52:147–57.
35. GuichaMrd P, Krell T, Chevalier M, Vaysse C, Adam O, Ronzon F, Marco S. Threedimensional morphology of rabies virus studied by cryo-electron tomography. J Struct Biol 2011;176:32–40.
36. Bastida-González F, Celaya-Trejo Y, Correa-Basurto J, Zárate-Segura P. Predicted 3D model of the rabies virus glycoprotein trimer. Biomed Res Int 2016;2016:1674580.
37. Passot S, Fonseca F, Alarcon-Lorca M, Rolland D, Marin M. Physical characterization of formulations for development of two stable freeze-dried proteins during both dried and liquid storage. Eur J Pharm Biopharm 2005;60:335–48.
38. Pikal MJ, Shah S. The collapse temperature in freeze drying: dependence on measurement methodology and rate of water removal from the glassy phase. Int J Pharm 1990;62:165–86.

39. Smith KM, Davidson JM, Garside P. T-cell activation occurs simultaneously in local and peripheral lymphoid tissue following oral administration of a range of doses of immunogenic or tolerogenic antigen although tolerized T cells display a defect in cell division. Immunology 2002;106:144–158.
40. Sayın B, Somavarapu S, Li XW, Thanou M, Sesardic D, Alpar HO, Senel S. Mono-*N*-carboxymethyl chitosan (MCC) and *N*-trimethyl chitosan (TMC) nanoparticles for non-invasive vaccine delivery. Int J Pharm 2008;363:139-48.
41. Jabbal-Gill I. Nasal vaccines. DD&S 2001;1:89–94.
42. Van der Lubben IM, Verhoef JC, Borchard G, Junginger HE. Chitosan and its derivatives in mucosal drug and vaccine delivery. Eur J Pharm Sci 2001;14:201–7.
43. Bacon A, Makin J, Sizer PJ, Jabbal-Gill I, Hinchcliffe M, Illum L, et al. Carbohydrate biopolymers enhance antibody responses to mucosally delivered vaccine antigens. Infect Immun 2000;68:5764–70.
44. Jabbal-Gill I, Fischer AN, Rappuoli R, Davis SS, Illum L. Stimulation of mucosal and systemic responses against Bordetella pertussis filamentous haemagglutinin and recombinant pertussis toxin after nasal administration with chitosan in mice. Vaccine 1998;16:2039–46.
45. Kalliola S, Repo E, Srivastava V, Heiskanen JP, Sirvio JA, Liimatainen H, Sillanpaa, M. The pH sensitive properties of carboxymethyl chitosan nanoparticles cross-linked with calcium ions. Colloids Surf B Biointerfaces 2017;153:229–36.
46. Lydyard P, Grossi C. The lymphoid system. In: Roitt I, Brostoff J, Male, D. editors. Immunology. London: Mosby; 1998. p. 31–42.

47. Izaguirre-Hernández IY, Mellado-Sánchez G, Mondragón-Vásquez Z, Thomas-Dupont P, Sánchez-Vargas LA, Hernández-Flores KG, et al. Non-conjugated chitosan-based nanoparticles to proteic antigens elicit similar humoral immune responses to those obtained with alum. J Nanosci Nanotechnol 2017;17:846–52.

# CHAPTER 4

# Interleukin 10 modifies the hyper-contractile state of isolated human airway smooth muscle cells: a new avenue for immunotherapy in obstructive lung disease?

## 1. INTRODUCTION

Patients with asthma typically experience periodic or persistent decreases in airflow from bronchospasm, and virtually all patients exhibit an exaggerated bronchoconstrictive response to exogenously administered agents such as histamine and methacholine, termed airway hyperresponsiveness (AHR). Clinically, AHR may represent the physiological outcome of an enhanced shortening of muscle fibers around the bronchial walls, which can lead to asthma exacerbations from a variety of stimuli [1]. The current view stipulates that the hyper-contractility of human airway smooth muscle (HASM) in asthma is a direct result of airway inflammation. However, the precise nature of the immunologic phenotype and the resulting mechanical phenotype associated with disease presentation, including AHR, remain unclear.

Type-2 cytokines recruit and activate inflammatory cells, leading to airway remodeling. This remodeling is then thought to affect the structural cells in the airways, including HASM cells, contributing to bronchial obstruction. A growing body of evidence, however, supports the hypothesis that cytokines mainly those produced by $T_H2$ cells, can also act directly on HASM cells promoting AHR to contractile agonists and attenuating HASM relaxation to $\beta$-adrenoreceptor stimulation [2,3]. Exogenous administration of IL-13 to the lungs or overexpression of IL-13 in the lungs, for example, results in increased airway responsiveness [3]. In culture HASM cells, IL-13 increases intracellular calcium $[Ca^{2+}]_i$ induced by bradykinin, histamine and acetylcholine. IL-13 also augments leukotriene-D4 ($LTD_4$)-induced changes in cell stiffness [4]. Strikingly, mice lacking $\alpha v\beta 8$ integrin expressed on dendritic cells are protected from AHR as a result of impaired IL-17A signaling without changes in inflammatory cell numbers

in response to sensitization and challenge with OVA demonstrating that IL-17A can contribute to AHR through its direct effects on smooth muscle, with no modulation on airway inflammation [5].

## 2. OBJECTIVES

Since several approaches show that effective intervention in airway allergic inflammation can be achieved with allergen-activated interleukin-10-secreting cells, here we assessed whether interleukin 10 (IL-10) and interleukin 22 (IL-22), a member of IL-10 cytokine family, have the ability to directly affect HASM cell contractility upon histamine stimulation using magnetic twisting cytometry (MTC). We further investigate whether IL-10 loaded chitosan nanoparticles (IL-10-CSNPs) could be used as a possible inhalable therapeutic tool for preventing exacerbations in asthmatic patients.

## 3. MATERIALS AND METHODS

### 3.1. Materials

All reagents were obtained from Sigma-Aldrich with exception of Dulbecco modified Eagle's medium (DMEM)-Ham's F-12 (1:1), which was purchased from GIBCO (Grand Island, NY, USA). The synthetic arginine-glycine-aspartic acid (RGD) containing peptide was purchased from American Peptide (Sunnyvale, CA, USA). Interleukins 10 and 22 were purchased from R&D Systems (Minneapolis, MN, USA).

### 3.2. HASM cell culture

HASM cells were obtained from airways from deceased asthmatic individuals obtained from the National Disease Research Interchange (Philadelphia, PA). HASM cell culture was performed as previously described [6]. Briefly, the cells at passages 3 through 5 were maintained in HASM's F-12 medium with 10% fetal bovine serum, 1% penicillin and streptomycin, 1% L-glutamine, 1.7 mM $CaCl_2$, 12 mM NaOH, and 25 mM HEPES. Cells were maintained in serum-free media for 24 hours at 37$^{o}$C in humidified air containing 5% $CO_2$ before study. These conditions have been optimized for seeding cultured cells on collagen matrix and for assessing their mechanical properties [7]. Serum-deprived post-confluent cells were plated at 30,000 cells/cm$^2$ on plastic wells.

### 3.3. Magnetic twisting cytometry (MTC)

Dynamic changes in cell stiffness were measured as an indicator of the contraction of isolated HASM cells using magnetic twisting cytometry (MTC), as described by our laboratory in detail elsewhere [8]. In brief, RGD-coated ferrimagnetic microbeads bound to the surface of adherent HASM cells were magnetized horizontally and then twisted in a vertically aligned homogenous magnetic field that was varying sinusoidally in time. This sinusoidal twisting magnetic field caused both a rotation and a pivoting displacement of the bead: as the bead moves, the cell develops internal stresses, which, in turn, resist bead motions [9]. Lateral bead displacements in response to the resulting oscillatory torque were detected with a spatial resolution of 5 nm, and the ratio of specific torque to bead displacements was computed and expressed here as the cell stiffness in units of Pascal per nanometer (Pa/nm).

In this study, adherent HASM cells were pre-treated with individual cytokines for 72 h. For each individual cell, baseline stiffness was measured for the first 60 s and after histamine addition at 1 μM, stiffness was measured continuously for the next 240s.

### 3.4. Preparation of the IL-10 loaded chitosan nanoparticles

The IL-10 loaded chitosan nanoparticles (IL-10-CSNPs) were prepared following a procedure previously described [10]. A 2 mg/ml chitosan solution was prepared by dissolving chitosan in a 0.05% (v/v) acetic acid solution and leaving under stirring for 24 h. The pH was adjusted to 5 with 1 M sodium hydroxide solution. TPP was dissolved in deionize water to a final concentration of 1 mg/ml. TPP and chitosan solutions were filtered through a 0.22 and 0.45 μm membrane respectively (Merck Milipore, Burlington, MA, USA). Then, the TPP solution containing IL-10 was added to the chitosan solution drop wise under vigorous magnetic stirring at room temperature. The resulting suspension was left to gelify for 1 h.

### 3.5. Determination of IL-10 loading efficiency

The loading efficiency was obtained indirectly by determining the concentration of IL-10 in the supernatant using Human IL-10 ELISA Kit (Thermo Fisher Scientific, Carlsbad, CA, USA). The amount of IL-10 loaded in the CSNPs was calculated as the difference between the target loading and the protein recovered in the supernatant. Loading efficiency (LE) was calculated using the following equation:

$$LE\ (\%) = \frac{\text{target loading} - \text{unloaded IL-10}}{\text{target loading}} \times 100$$

### 3.6. *In vitro* release studies

The nanoparticles were suspended, in triplicate, in individual Eppendorf tubes containing 1 ml of phosphate buffer saline (PBS) at pH 7.4. Sample tubes were incubated at 37$^{o}$C with continuous agitation. To sample the released IL-10, the tubes were centrifuged and the supernatant was collected for assessment. The tubes were then replenished with 1 ml of fresh PBS and placed back at 37$^{o}$C under agitation. Samples were periodically taken at specific time intervals. To estimate the amount of IL-10 released from nanoparticles ELISA were performed using Human IL-10 ELISA Kit (Thermo Fisher Scientific, Carlsbad, CA, USA).

### 3.7. Fluorescence microscopy

Uptake of nanoparticles was visualized under a fluorescence microscope (Leica Microsystems, Chicago, IL, USA). HASM cells were grown on glass cover slips in 6-well plates at a seeding density of 50,000 cells in 1.5 ml of culture medium. After 24 h, the spent medium was removed and the cells were exposed to BSA-FITC loaded CSNPs (BSA-FITC-CSNPs) for 24 h. The cells were washed once with PBS (1 ml) before fixation with 4% paraformaldehyde. The cell nucleus was stained for nucleic acids with 4', 6-Diamidino-2-phenylindone dihydrochloride (DAPI, 2 mM). Cells in culture medium were used as the control. To differentiate between fluorescence attributed to internalized BSA-FITC-CSNPs with that associated with NPs attached to the cell membrane, the extracellular fluorescence was quenched by post-uptake incubation of the HASM cells with

trypan blue solution for 1 min [11]. The dye was removed by thorough washing of the cells with PBS before visualization under a fluorescence microscope.

### 3.8. Cytotoxicity studies

The cell viability was measured using Cell Counting Kit-8 (Sigma-Aldrich, St. Louis, MO, USA) according to the manufacturer's instruction. Briefly, HASM cells were seeded at a density of 5,000 cells/well into a 96 well plate, kept under standard culturing conditions and allowed to attach for 24 h before exposure to NPs suspensions. After reaching 90% confluency, HASM cells were incubated with different concentrations of the NPs for a period of 24 h. Cells in media alone (untreated cells) were used as a negative control. Subsequently, 10 μl of CCK-8 solution was added to each well and cells were incubated for 4 h at 37$^{o}$C. Optical density at 450 nm was monitored using a microplate reader (Molecular Devices LLC, Sunnyvale, CA, USA) according to the manufacture's protocol. Triplicate samples were analyzed for each experiment.

### 3.9. Statistical analysis

Data are shown as mean ± SEM. Analysis of experiments was performed using unpaired Student's *t* test, or one-way ANOVA with Dunnett's multiple comparisons. The GraphPad Prism statistical software program was used for the analyses. *P < 0.05; **P < 0.01; ***P <0.001 were regarded as statistically significant.

# 4. RESULTS AND DISCUSSION

## 4.1. Magnetic twisting cytometry

### *4.1.1. Interleukin 10*

IL-10 is an anti-inflammatory cytokine, produced by T cells (mainly type 1 Treg cells), monocytes, macrophages, DCs, B cells (mainly Breg cells) and a small fraction of NK cells. Mast cells can also secrete IL-10, limiting the rate of leukocyte infiltration, inflammation, and some skin disorders such as contact dermatitis [12]. It is well known that IL-10 modulates many types of cells and effector functions associated with allergic disease (including mast-cell and eosinophil function, IgG to IgE ratios, and $T_H2$-cell activation), and a recent study also indicates that the occurrence of allergic disease itself reflects an imbalance between $T_H2$ cells and IL-10-secreting regulatory T cells [13]. New evidence, however, suggests that cytokines can also act directly on airway smooth muscle, leading to increased responses to contractile agonists [2-5].

To ascertain whether IL-10 has an inflammation-independent effect on airway smooth muscle, we measured dynamic changes in cytoskeleton stiffness using HASM cells derived from 3 asthmatic donor lungs. We evaluated the effect of three doses (0.1, 1, or 10 ng/ml) of IL-10 on asthmatic HASM cells in response to histamine (1 $\mu$M). Our results show that previous exposure to IL-10 for 72 hours at 10 ng/ml caused a significant decrease in baseline cell stiffness and cell stiffening responses to histamine for all asthmatic donors **(Fig. 1A, B and C, D and E, F)**.

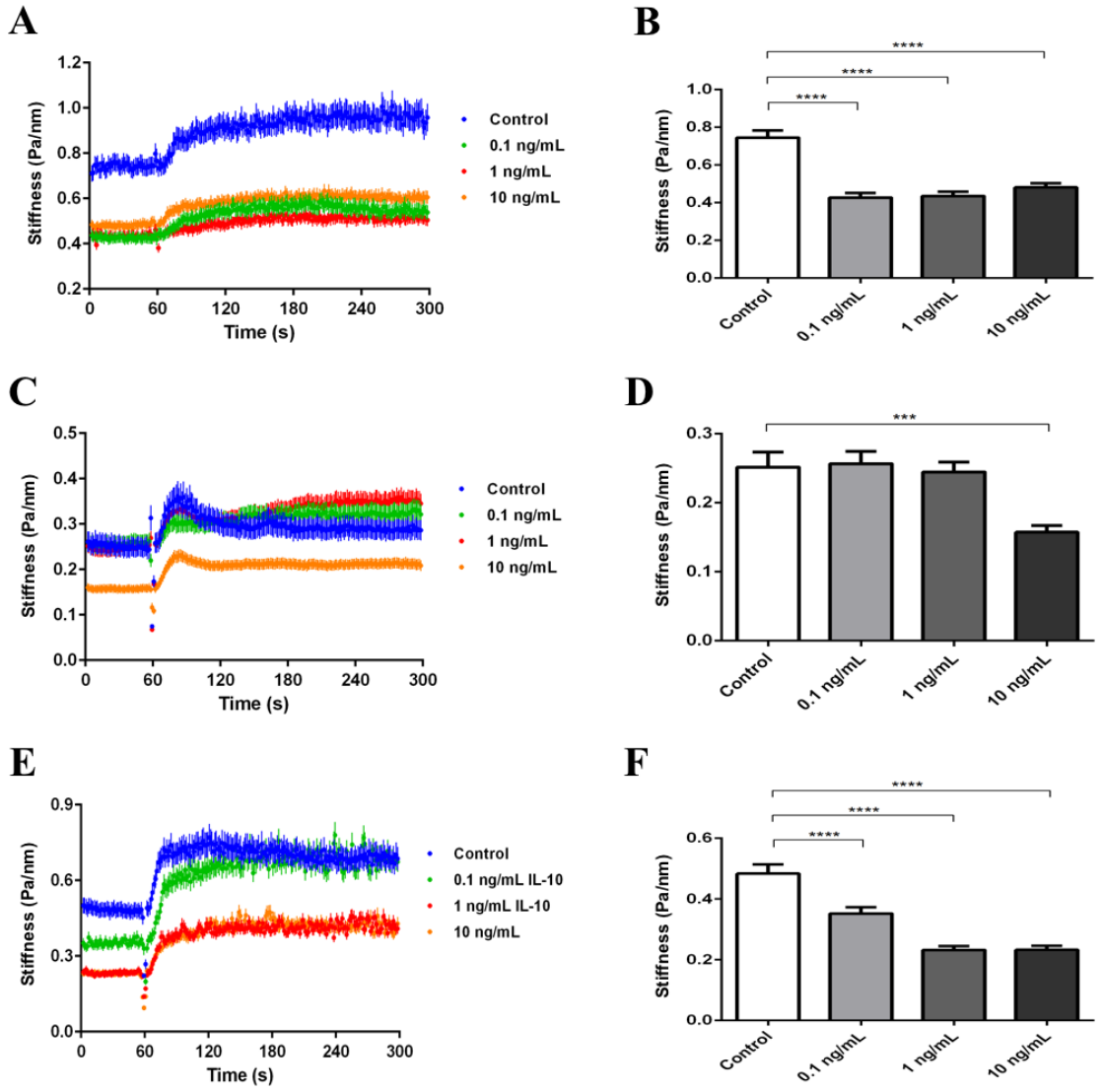


**Figure 1**. Dynamic changes in cell stiffness of HASM cells derived from individual lung donors (A and B), (C and D), and (E and F) pre-treated with IL-10 for 72 h in response to 1 μM histamine. For each individual human HASM cell, baseline stiffness was measured for the first 60 seconds, and after histamine addition stiffness was measured continuously for the next 240 seconds.

These results establish that IL-10 exerts an inflammation-independent effect on HASM cells from asthmatic individuals contracted with histamine and contributes to the HASM cells responsiveness by acting directly on the ASM itself. Thus, we suggest that IL-10 play a major role in the airway function, and this is

not only a consequence of its well-known anti-inflammatory and suppressive effects on $T_H1$ responses.

Chung et al. (1999) [14] reported that human airway smooth muscle cells in culture can be induced to express eotaxin mRNA and to release eotaxin protein when incubated with TNF-$\alpha$ or IL-1$\beta$. IL-10 significantly inhibited eotaxin release while corticosteroids had no effect. In addition, John et al. (1997; 1998) [15,16] found that IL-10 inhibited the stimulated release of IL-8, RANTES and eotaxin from airway smooth muscle cells, although IL-10 did not suppress eotaxin mRNA, indicating that IL-10 may interfere with a post-transcriptional regulation mechanism of eotaxin.

Although clinical trials of the treatment of autoimmune disease with recombinant IL-10 show that it is well tolerated, the disadvantage of using IL-10 as a therapeutic is its relatively short half-life *in vivo* [17,18]. Therefore, we examined IL-10 loaded chitosan nanoparticles (IL-10-CSNPs) as a possible inhalable therapeutic tool for preventing exacerbations in asthmatic patients. Chitosan is a cationic biopolymer with well-known mucoadhesive properties and has been shown to promote adsorption, uptake, and retention of therapeutic compounds in different cell types, including epithelial cells [19].

We hypothetized that IL-10-CSNPs delivered directly to the lungs would be able to attenuate histamine-induced AHR through its direct effect on HASM cells. However, our results show that previous exposure to IL-10-CSNPs (internalization by HASM cells was confirmed by fluorescence microscopy) at any concentration had no significant effect in cell-stiffening response compared to cells from control group **(Fig. 2A, B and C, D and E, F)**, confirming that the

significant decrease in cell-stiffening caused by previous exposure to IL-10 is mediated by IL-10 receptors on the cell surface of HASM cells [20].

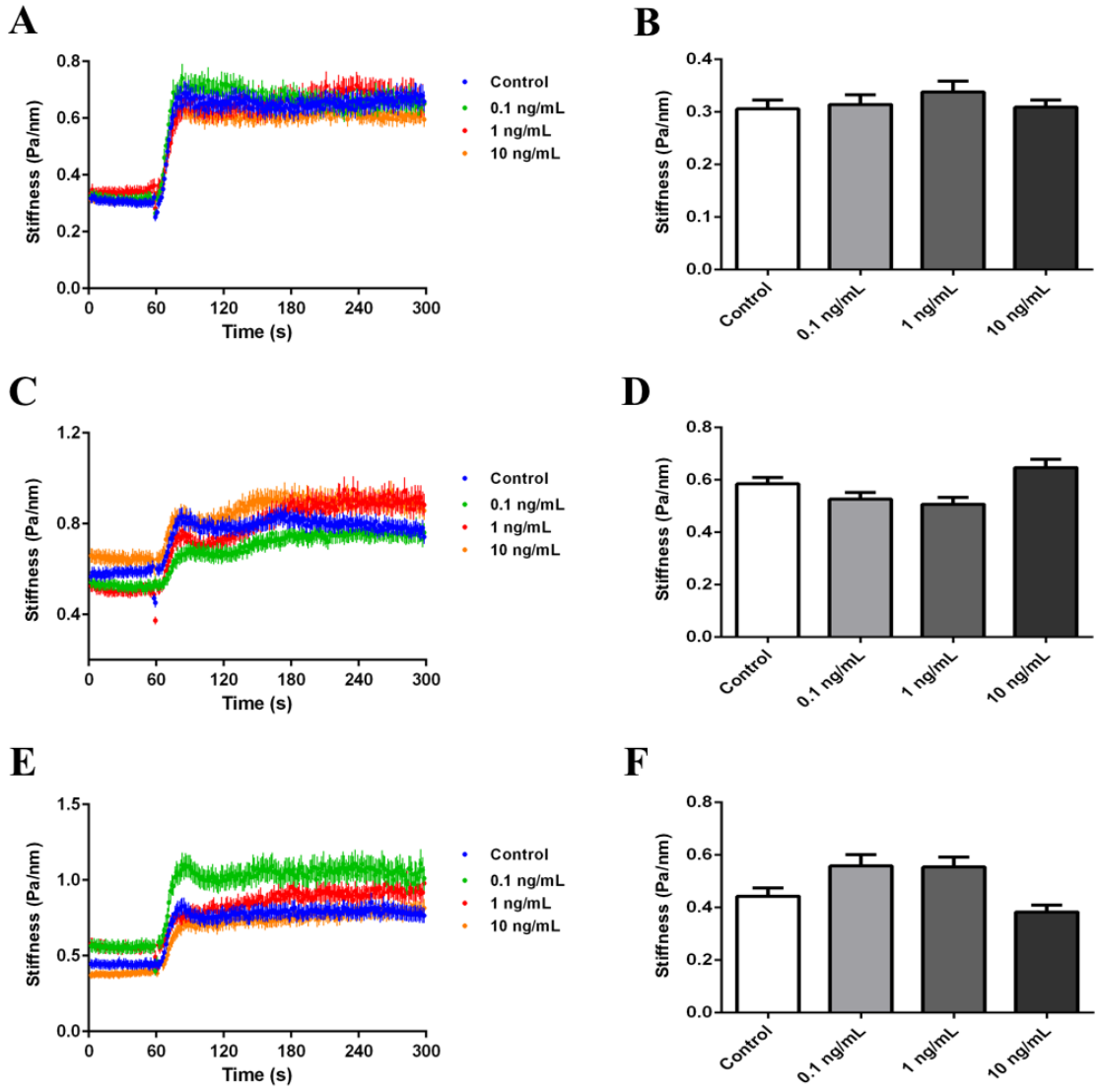


**Figure 2**. Dynamic changes in cell stiffness of HASM cells derived from individual lung donors (A and B), (C and D), and (E and F) pre-treated with IL-10-CSNPs for 72 h in response to 1 μM histamine. For each individual human HASM cell, baseline stiffness was measured for the first 60 seconds, and after histamine addition stiffness was measured continuously for the next 240 seconds.

IL-10 cellular responses require the specific recognition and assembly of a heterodimeric cell surface complex comprised of IL-10R1 and IL-10R2 chains, and mutations in IL-10, IL-10R1, and IL-10R2 that disrupt IL-10 signaling have been identified in children who suffer from early inflammatory bowel disease [21-23]. While IL-10R1 and IL-10R2 extracellular domains bind IL-10, the intracellular domains are associated with JAK1 and Tyk2 kinases, respectively, which phosphorylates themselves and IL-10R1 intracellular domain tyrosines. The phosphotyrosines provide docking sites that activate the transcription factors STAT3, STAT1 and STAT5. Upon phosphorylation, STAT1 and STAT3 homo/heterodimerise and translocate to the nucleus where they bind with high affinity to STAT-binding elements in the promoters of several IL-10-responsive genes [24,25].

The local delivery of IL-10 to inflamed sites remains a major challenge, and some interesting experimental approaches are being undertaken in this field. Recently, a rIL-10 gene has been fused to the Type III secretion apparatus of *Shigella* and the secreted IL-10 seemed to inhibit bacterially induced inflammatory reactions [26]. Other approaches have included the delivery of genes to specific sites of the gastrointestinal tract via the oral administration of gelatin nanoparticles, where the IL-10 gene expression was detected by reverse transcriptase PCR. This approach resulted in suppression of inflammatory responses in a murine acute colitis model [27].

Alternatively, a more attractive strategy is the local delivery of inhibitory signals through the induction of allergen-activated IL-10-secreting regulatory T cells, with IL-10 production occurring only following activation after exposure to allergen, eliminating potential fibrogenic effects associated with its continuing

presence and TGF-β that is also produced [28]. Generally, the allergen is given subcutaneously (SCIT), but it can be administered intranasally or sublingually (SLIT) [29-32].

Studies in animal models have used several approaches to show that effective intervention in allergic inflammation can be achieved with allergen-activated IL-10-secreting cells [33-36]. Akbari and colleagues[35] showed that tolerance that is induced by respiratory exposure to allergen delivered intranasally using a model of allergic airway disease, inhibited the development of AHR and caused the induction of IL-10-secreting regulatory T cells by pulmonary DCs. Various current strategies have been investigated to improve allergen immunotherapy by reducing adverse reactions, such as the use of engineered or recombinant allergens preparations to provide purer allergens with reduced allergenicity and therefore, increased safety and specificity [37].

Immunostimulatory CpG motifs, which are present in bacterial DNA, are recognized by the pattern-recognition receptor Toll-like receptor 9 (TLR9) [38,39]. These motifs function as adjuvants to promote $T_H1$ responses through their effects on DCs [40,41], and this property has been exploited with conjugates of allergen and CpG-containing oligodeoxynucleotides (CpG ODNs) in studies in rabbits, monkeys and mice that clearly show that these conjugates stimulate $T_H1$ responses in both the peripheral blood and nasal tissue [42]. Sabatel et al. (2017) [43] found that CpG is able to expand the interstitial macrophage population from splenic and local reservoir monocytes and, by producing IL-10, these cells were able to confer protection against allergic inflammation even when mice were sensitized and challenged with house dust mice, revealing a role for these regulatory macrophages in the context of CpG exposure in allergic airway

inflammation. They suggest that similar mechanisms might be related to the reduced risk of asthma development that is associated with exposure to a microbe-abundant environment

Other approaches have been adopted *in vitro* and *in vivo* models supporting a therapeutic role of IL-10 synthesizing T cells in attenuating allergic symptoms, as showed in a recent study that demonstrate that $CD4^+$ cells engineered to express IL-10 prevent inflammation and $T_H2$-driven airway hyperresponsiveness [34]. Strategies that modify APC function such as the use of pathogens or their components has also been shown to promote IL-10-secreting T cells which in turn had the capacity to confer protection against airway inflammation [44]. Collectively, these data suggest that immunotherapy is a potential therapeutic approach for the treatment of asthma and for the prevention of development asthma.

It is noteworthy that if left untreated, patients with nasal allergies have a 19% chance of developing asthma [45], however, the early administration of immunotherapy has the potential to prevent new sensitivities development, improve asthma if present at the time of treatment initiation, and prevent future asthma, so it is reasonable to provide specific immunotherapy to stabilize and revert the inflammation that may eventually leads to asthma. Very young children have been treated successfully with SLIT [46].

Thereby, it might be possible to combine non-specific treatments. It was reported that administration of a large dose of glucocorticoids at the same time or immediately before immunotherapy would be predicted to induce IL-10 production, which in turn, would induce antigen-specific IL-10-secreting regulatory T cells and regulate APC function [47]. Although all these treatments

function non-specifically, this knowledge might also increase the likelihood of restoration of the impaired regulatory activity in patients with glucocorticoid-resistant asthma [48].

### 4.2. Preparation and characterization of IL-10 loaded chitosan nanoparticles (IL-10-CSNPs)

Chitosan nanoparticles were prepared by the ionic cross linking between amino groups of chitosan with phosphate groups of tripolyphosphate (TPP) with the dropwise addition of TPP to a chitosan solution (concentration 2 mg/ml). Preliminary experiments were addressed in order to select the optimal ratios for the formation of nanoparticles. The major factors that had critical effects on nanoparticle formation include concentration of the polymer and cross linker and stirring speed. The appearance of opalescence was used as an indicator of nanoparticle formation, which was also confirmed by means of dynamic light scattering.

IL-10-CSNPs prepared with a chitosan/TPP ratio of 3:1 turned out to the be best formulation, with an average size of 195 nm. The presence of IL-10 had a small influence on particle size, increasing it by few nanometers. This can be ascribed to the ionic interaction between positively charged chitosan and negatively charged IL-10 under the preparation conditions (~ pH 6), which generates a reduction of electrical repulsion among them. Besides that, chitosan chains intra and intermolecular cross-links mediated by TPP favors a more compact structure [10].

The polydispersity index (PDI) was found to be 0.160 for IL-10-CSNPs, indicating that a homogeneous dispersion was obtained. The nanoparticle

suspension became more turbid by increasing the amount of TPP, however aggregation occurred rapidly and drastically due to the formation of inter and intramolecular cross-linkages mediated by the anionic molecule which enable chitosan nanoparticles to form larger particles and flocculating aggregates [49]. The optimal formulation was formed in the range between the appearance of the opalescence and flocculation. The zeta potential value for was found to be +17.1 mV.

The entrapment efficiency of IL-10 determined by ELISA was found to be 99.16%. This can be ascribed to the ionic interaction and cross-linking between positively charged chitosan and negatively charged IL-10 (pI = 8.4) under the preparation conditions, since IL-10 was diluted in TPP solution (pH 9) before its addition to the cationic chitosan solution (pH 5). As shown in **Fig. 3A** the IL-10 release profile was biphasic, characterized by an initial protein burst in the first 8 days and followed by a sustaining release up to 28 days.

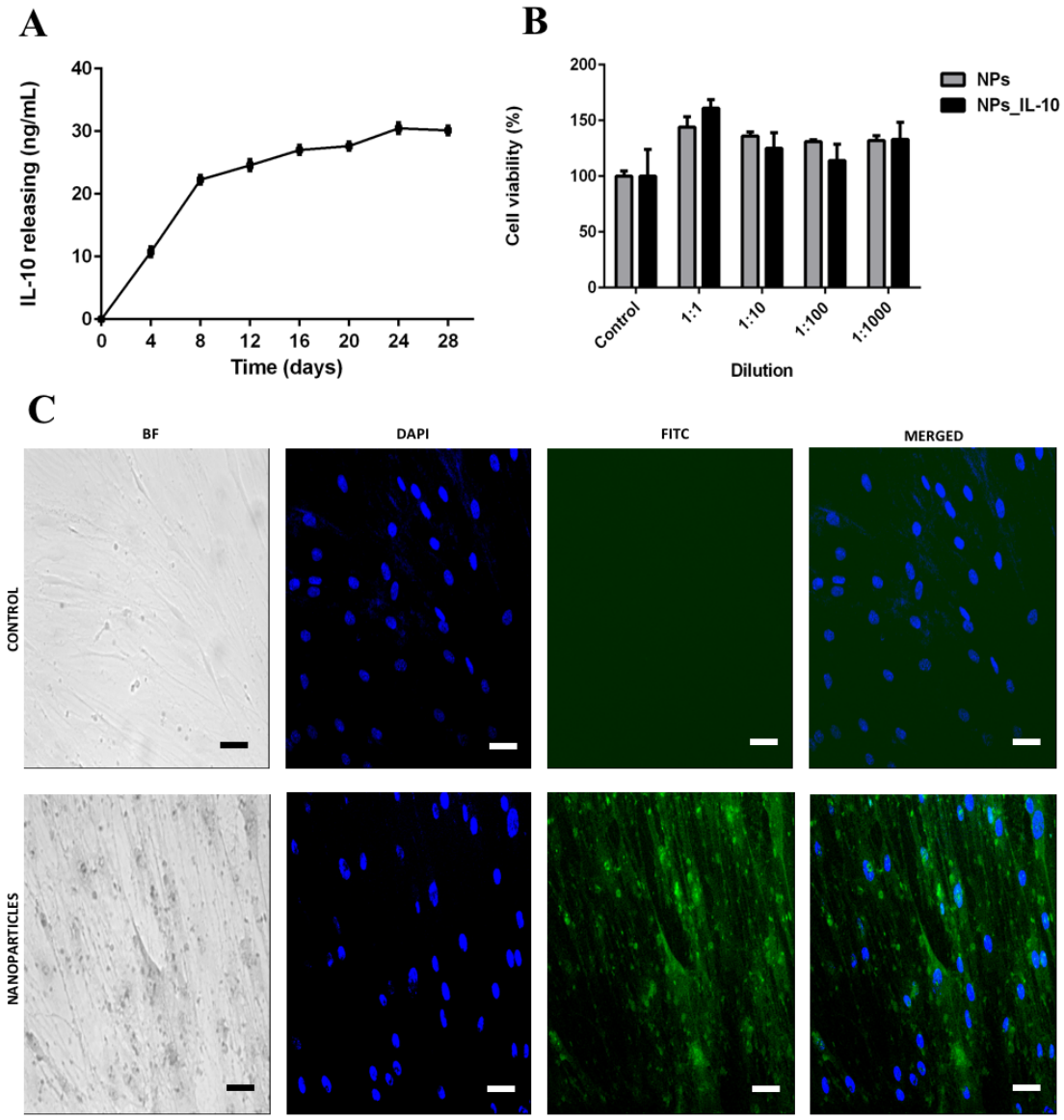


**Figure 3**. (A) Release profile of IL-10-CSNPs over 28 days. (B) Results of Cell Counting Kit-8 (CCK-8) assay showing no toxic effect of CSNPs and IL-10-CSNPs. Data represent mean ± SD (*n* = 3). (C) Fluorescence images of HASM cells incubated for 24 hours with BSA-FITC-CSNPs. Cells in culture medium were used as the control.

### 4.3. Cytotoxicity studies

Cytotoxicity of CSNPs and IL-10-CSNPs on HASM cells were studied using CCK-8 assay as shown in **Fig. 3B**. HASM cells exposed to CSNPs and IL-10-

CSNPs showed high cell viability for all dilutions tested indicating the non-toxicity of the nanoparticles.

### 4.3. Fluorescence microscopy

Cellular uptake of chitosan nanoparticles was examined in HASM cells exposed for 24 h to BSA-FITC and BSA-FITC loaded chitosan nanoparticles (BSA-FITC-CSNPs) by visualizing the intrinsic fluorescence of BSA-FITC using fluorescence microscopy using fluorescence microscopy. While HASM cells exposed to BSA-FITC showed no fluorescence, the cells incubated with BSA-FITC-CSNPs showed remarkable green fluorescence, including uptake into the cell nucleus, confirming the internalization of the particles **(Fig. 3C)**. This correlates well with the positive zeta potential of the chitosan nanoparticles as the cationic surface charges facilitate nanoparticles interaction with the anionic glycoproteins on the cell membrane [50].

According to Huang et al. (2002) [51] the uptake of FITC-chitosan NPs by the A549 cells, a human cell line derived from the respiratory epithelium, is unlikely to be internalized by fluid-phase endocytosis, since the uptake was a temperature- and concentration-dependent saturable event. Moreover, chitosan molecules at 0.2 mg/ml, despite having near zero zeta potential were capable of adhering to the A549 cells with similar tenacities as the positively charged nanoparticles at the same concentration. Therefore, it was suggested that other forms of interactions, e.g., H-bonding and hydrophobic interactions, could have contributed to the adhesion of the chitosan molecules and chitosan nanoparticles to the A549 cells.

Of the two energy-dependent, saturable endocytic pathways, receptor-mediated endocytosis is initiated by ligand binding to specific cell membrane receptors, however no receptor specific for chitosan has been reported to exist in cell membranes. On the other hand, adsorptive endocytosis is preceded by nonspecific interaction of ligand with the cell membrane, and chitosan is known to interact with cell membranes by nonspecific electrostatic forces of attraction [52, 53].

Additionally, it was demonstrated that by the inhibition of clathrin using chlorpromazine, the most widely studied protein identified to regulate cellular trafficking of cargo by endocytosis, chitosan nanoparticles internalization was reduced up to 65% by the A549 cells [51]. However, the inhibition of clathrin did not completely abolish the internalization of the nanoparticles, suggesting that clathrin independent pathways were probably also involved. Furthermore, such pathways did not seem to involve caveolae since the nanoparticle uptake was unaffected by filipin, which disrupted caveolae structures by binding and precipitating cholesterol.

## 4.4. Magnetic twisting cytometry

### *4.4.1. Interleukin 22*

IL-22 is a member of the IL-10 cytokine family, produced by many types of immune cells, such as lymphoid tissue inducer-like cells, natural killer cells, $CD11c^{+}$ myeloid cells, $T_H1$ cells, $T_H17$ cells, and $T_H22$ T-cell subset [54-60]. The receptor of IL-22 (IL-22R) is a heterodimer that consist of IL-22R1 chain and the IL-10 shared signal transducing receptor of IL-10R2 [12]. While the extracellular

region of IL-22R1 (sIL-22R1) exhibit high affinity (~nM) for IL-22, IL-10R2 interactions are very weak (~μM-mM) [61].

The expression pattern of IL-22R implies that IL-22 exerts its effects including tissue epithelium in the intestine, liver, skin, kidney, and lungs [62, 63]. While IL-22R1 expression is localized to the conducting airways (nonciliated and ciliated cells) in the lungs of naïve mice, in humans, IL-22R1 is expressed by airway smooth muscle cells and epithelium [64], demonstrating that IL-22 may also affect the cells within the bronchial wall. Furthermore, an IL-22 binding protein (IL-22BP) is a secreted receptor of IL-22 that binds to soluble IL-22 with high affinity and shares 34% sequence identity with (sIL-22R1) [61]. However, the biochemical properties and the functional roles of the IL-22BP and its isoforms have not been elucidated.

The inflammatory properties of IL-22 in the lung are conflicting. Some evidence suggested that IL-22, like IL-17, act as a proinflammatory cytokine, inducing the recruitment of granulocytes synergistically with IL-17 and thus increasing inflammation in mouse models of allergic asthma [65, 66]. On the other hand, some studies pointed to a direction in that IL-22 may be protective in allergic airway inflammation. Mice lacking IL-17 production in a mouse model of allergic asthma showed less inflammation, reduced airway tissue damage, and decreased numbers of infiltrating cells after administration of IL-22 [65, 66]. These somewhat contradictory results highlight the importance of study design regarding modeling human asthma.

Therefore, to ascertain whether IL-22 has an inflammation-independent effect on ASM we measured dynamic changes in cytoskeleton stiffness using primary HASM cells derived from 3 asthmatic donor lungs. We evaluated the

effect of three doses (0.1, 1, or 10 ng/ml) of IL-22 on asthmatic HASM cells in response to histamine (1 μM). Our results show that previous exposure to IL-22 for 72 hours at 10 ng/ml caused a significant decrease in cell-stiffening (baseline stiffness) for all asthmatic donors compared to cells from control group **(Fig. 4A, B and C, D and E, F)**.

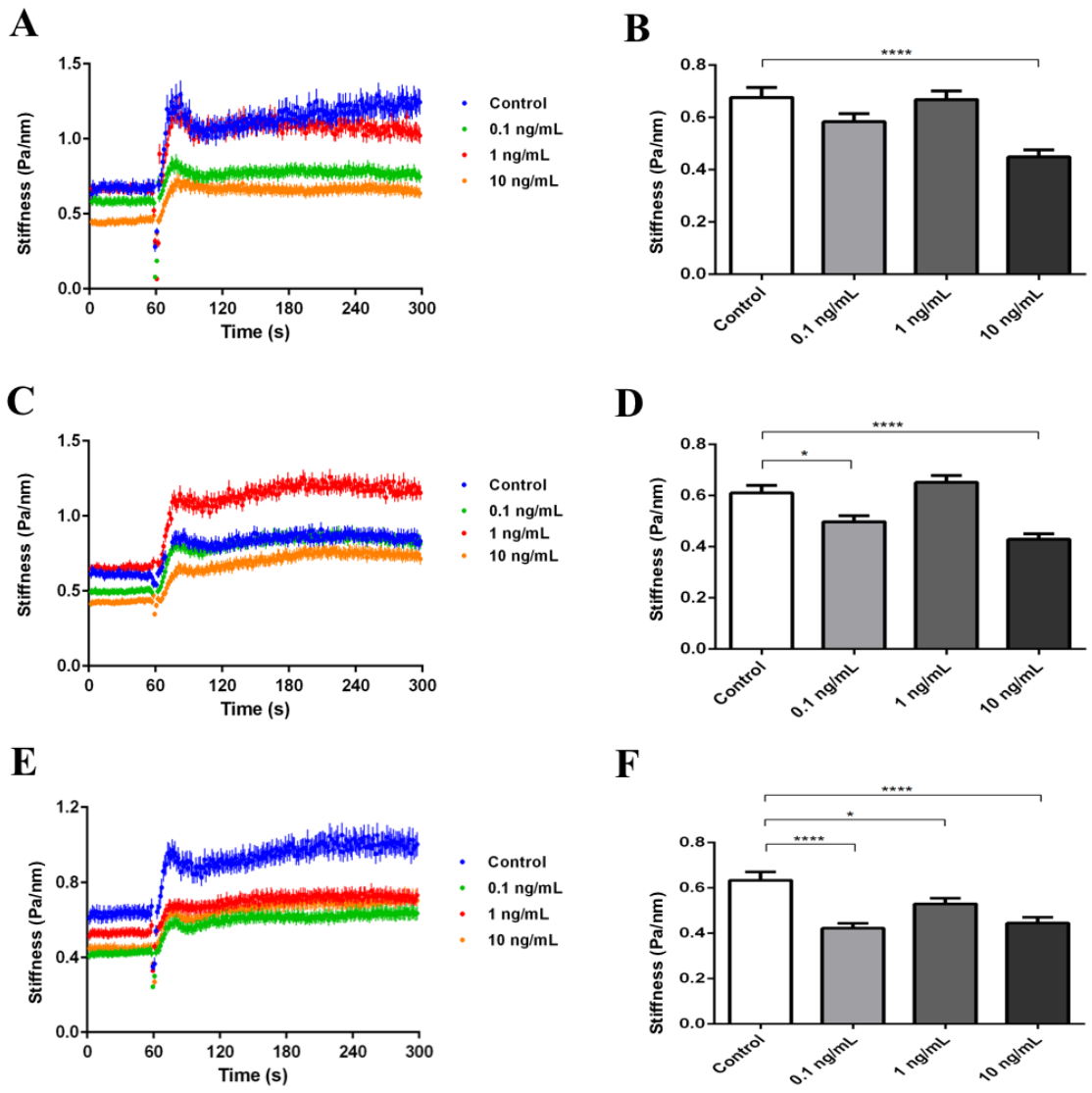


**Figure 4**. Dynamic changes in cell stiffness of HASM cells derived from individual lung donors (A and B), (C and D), and (E and F) pre-treated with IL-22 for 72 h in response to 1 μM histamine. For each individual human HASM cell, baseline stiffness was measured for the first 60 seconds, and after histamine addition stiffness was measured continuously for the next 240 seconds.

As previously reported [67], there is heterogeneity in responses to histamine from cells derived from different donors. Moreover, HASM cells from those with asthma have increased basal tone and contractility to asthmatic spasmogens in response to activation of $H_1$-histamine receptors, G protein-coupled receptors, and $M_3$ muscarinic receptors.

However, our findings are consistent with one report in which was demonstrated that IL-22 transgenic mice (inducible lung-specific) that received OVA showed significantly reduced lung resistance at methacholine concentrations above 6.25 mg/ml, indicating that IL-22 in the airways may protect mice from allergen induced AHR [68]. Similarly, systemic overexpression of IL-22 in OVA-treated mice showed IL-22-mediated suppression of allergic airway inflammation through an IL-10 dependent mechanism [69]. It was also observed an inverse correlation between the expression of the proinflammatory chemokines CCL5/RANTES and CXCL10/interferon-inducible protein 10 and IL-22 expression in BAL fluid of asthmatic patients *in vivo* [70].

In contrast to IL-22R1, which is selectively expressed on different cell types, IL-10R2 is ubiquitously expressed on all cell types [61]. According to Jones et al. (2008) the weak binding of IL-10R2 suggests that IL-10R2 functions as a sensor chain, which in turn activates signaling based on the kinetics of the R1 chain. Importantly, they found that this weak binding also promotes “promiscuous” interactions of IL-10R2 with IL-22, IL-10, and other interleukins such as IL-26, IL-28, and IL-29, reducing the number of unique chains required for IL-10 family cytokine signaling.

Importantly, Lejeune et al. (2002) [71] showed that IL-22 induced the phosphorylation of JAK1 and Tyk2, and because Tyk2 has been shown to be

associated with IL-10R2, they suggest that JAK1 associates with IL-22R. Moreover, both cytokines induce the phosphorylation of the same STAT factors [72]. These observations extend the similarities between IL-22 and IL-10, which also activates JAK1 and Tyk2 [71,72], and provide a reasonable explanation for the very similar effects of both cytokines on HASM cell-stiffening observed in the present study.

Despite the anti-inflammatory and suppressive effects associated with IL-22 such as decreased eosinophils in the bronchoalveolar lavage, reduction in eosinophilic inflammation in the lung, and decreased mucus metaplasia in the airways[68], through mechanisms such as reduction in IL-13 production by cells from IL-22 transgenic mice, our results show that IL-22 also act through an inflammation-independent effect on HASM cells from asthmatic individuals, contributing to the HASM cells responsiveness by acting directly on ASM, and playing an important role in the airway function, and not only as a consequence of its recently reported Reg3$\gamma$-mediated suppressive effects (upon IL-22 stimulation in a STAT3-dependent manner) on lung epithelial cells and $T_H2$ cytokine production in a model of allergic airway inflammation induced by intra-tracheal administration of house dust mites (HDMs) [73].

## 5. CONCLUSION

Recent findings regarding the dynamic behavior of ASM has provided new concepts to the understanding of mechanisms related to the excessive airway narrowing episodes observed in asthma. A body of evidence suggests that cytokines also act directly on HASM cells, promoting airway hyperresponsiveness to contractile agonists and attenuated relaxation to $\beta$-

adrenoreceptor stimulation, which favors such narrowing in the airways of asthmatic patients. In conclusion, our study establishes that cytokines, important airway inflammation modulators, produced by different cell sources, can also contribute to the establishes that IL-10 exerts its suppressive effects not only through inhibition of $T_H1$ responses, but also through an inflammation-independent effect on HASM cells by significantly decreasing its baseline stiffness, which in turn reveals a previously unknown mechanism underlying immunotherapy as a potent therapeutic tool for prevention and treatment of airway allergic inflammation and asthma. However, further studies will be needed to determine the precise signaling pathways triggered by IL-10 in HASM cells, and it should be the major consideration in the design of future therapies for prevention and treatment of asthma.

## 6. REFERENCES

1. An SS, Bai TR, Bates JHT, et al. Airway smooth muscle dynamics: a common pathway of airway obstruction in asthma. Eur Resp J 2007;29:834–860.
2. Shore SA and Moore PE. Effects of cytokines on contractile and dilator responses of airway smooth muscle. Clin Exp Pharmacol Physiol 2002;29:859–866.
3. Renauld J-C. New insights into the role of cytokines in asthma. J Clin Pathol 2001;54: 577–589.
4. Shore SA. Direct effects of Th2 cytokines on airway smooth muscle. Curr Opin Pharmacol 2004;4:235–240.

5. Kudo M, Melton AC, Chen C, et al. IL-17A produced by αβ T cells drives airway hyperresponsiveness in mice and enhances mouse and human airway smooth muscle contraction. Nat Med 2012;18:547–554.
6. Damera G, Fogle HW, Lim P, et al. Vitamin D inhibits growth of human airway smooth muscle cells through growth factor-induced phosphorylation of retinoblastoma protein and checkpoint kinase 1. Br J Pharmacol 2009;158:1429–441.
7. Deshpande DA, Wang WCT, McIlmoyle EL, et al. Bitter taste receptors on airway smooth muscle bronchodilate by localized calcium signaling and reverse obstruction. Nat Med 2010;16:1299–1304.
8. 8. An SS, Fabry B, Trepat X, et al. Do biophysical properties of the airway smooth muscle in culture predict airway hyperresponsiveness? Am J Respir Cell Mol Biol 2006;35:55–64.
9. Fabry B, Maksym GN, Butler JP, et al. Scaling the microrheology of living cells, Phys Rev Lett 2001;87:148102.
10. Rampino A, Borgogna M, Blasi P, et al. Chitosan nanopartciles: preparation, size evolution and stability. Int J Pharm 2013;455:219–228.
11. Hu C-s, Chiang C-s, Hong P-d, Yeah M-k. Influence of charge on FITC-BSA-loaded chondroitin sulfate-chitosan nanoparticles upon cell uptake in human Caco-2 cell monolayers. Int J Nanomed 2012;7:4861–4872.
12. Akdis M, Aab A, Altunbulakli C, et al. Interleukins (from IL-1 to IL-38), interferons, transforming growth factor β, and TNF-α: receptors, functions, and roles in diseases. J Allergy Clin Immunol 2016;138:984–1010.

13. Akdis M, Verhagen J, Taylor A, et al. Immune responses in healthy and allergic individuals are characterized by a fine balance between allergen-specific T regulatory 1 and T helper 2 cells. J Exp Med 2004;199:1567–1575.
14. Chung KF, Patel HJ, Fadlon EJ, et al. Induction of eotaxin expression and release from human airway smooth muscle cells by IL-1β and TNFα: effects of IL-10 and corticosteroids. Br J Pharmacol 199;127:1145–1150.
15. John M, Au BT, Jose PJ, et al. Expression and release of interleukin-8 by human airway smooth muscle cells: inhibition by Th-2 cytokines and corticoids. Am J Resp Cell Mol Biol 1998;18:84–90.
16. John M, Hirst SJ, Jose PJ, et al. Airway smooth muscle dynamics: a common pathway of airway obstruction in asthma. J Immunol 1997;158:1841–1847.
17. Asadulllah K, Sterry W and Wolk HD. Interleukin-10 therapy – review of a new approach. Pharmacol Rev 2003;55:241–269.
18. Fuchs AC, Granowitz EV, Shapiro L, et al. Clinical, hematologic, and immunologic effects of interleukin-10 in humans. J Clin Immunol 1996;16:291–303.
19. Xia Y, Fan Q, Hao D, et al. Chitosan-based mucosal adjuvants: sunrise on the ocean. Vaccine 2015;33:5997–6010.
20. Grunstein MM, Hakonarson H, Leiter J, et al. Autocrine signaling by IL-10 mediates altered responsiveness of atopic sensitized airway smooth muscle. Am J Physiol Lung Cell Mol Physiol 2001;281:L1130–L1137.
21. Engelhardt KR, Shah N, Faizura-Yeop I, et al. Clinical outcome in IL-10- and IL-10 receptor-deficient patients with or without hematopoietic stem cell transplantation. J Allergy Clin Immunol 2013;131:825–30.

22. Glocker EO, Kotlarz D, Boztug K, et al. Inflammatory bowel disease and mutations affecting the interleukin-10 receptor. N Engl J Med 2009;361:2033–45.
23. Grundtner P, Gruber S, Murray SS, et al. The IL-10R1 S138G loss-of-function allele and ulcerative colitis. Genes Immun 2009;10:84–92.
24. Mosser DM and Zhang X. Interleukin-10: new perspectives on an old cytokine. Immunol Rev 2008;226:205–218.
25. Walter MR. The molecular basis of IL-10 function: from receptor structure to the onset of signaling. Curr Top Microbiol Immunol 2014;380:191–212.
26. Chamekh M, Phalipon A, Quertainmont R, et al. Delivery of biologically active anti-inflammatory cytokines IL-10 and IL-1ra in vivo by the Shigella type III secretion apparatus. J Immunol 2008;180:4292–4298.
27. Bhavsar MD and Amiji MM. Oral IL-10 gene delivery in a microsphere-based formulation for local transfection and therapeutic efficacy in inflammatory bowel disease. Gene Ther 2008;15:1200–1209.
28. Hawrylowics CM, Garra AO'. Potential role of interleukin-10-secreting regulatory cells in allergy and asthma. Nat Rev Immunol 2005;5:271–283.
29. Norman PS. Immunotherapy: past and present. J Allergy Clin Immunol 1998;102:1–10.
30. Bousquet J, Lockey R, Malling H-J and WHO panel members. Allergen immunotherapy: therapeutic vaccines for allergic diseases. A WHO position paper. J Allergy Clin Immunol 1998;102:558–562.
31. Norman PS. Immunotherapy: 1999–2004. J Allergy Clin Immunol 2004;113:1013–1023.

32. Wilson DR, Torres LI, and Durham SR. Sublingual immunotherapy for allergic rhinitis. Cochrane Database Syst Rev 2003;2:CD002893.
33. Stämpfli MR, Cwiartka M, Gajewska BU, et al. Interleukin-10 gene transfer to the airway regulates allergic mucosal sensitization in mice. Am J Respi Cell Mol Biol 1999;21:586–596.
34. Oh JW, Seroogy CM, Meyer EH et al. CD4 T-helper cells engineered to produce IL-10 prevent allergen-induced airway hyperreactivity and inflammation. J Allergy Clin Immunol 2002;110:460–468.
35. Akbari O, DeKruyff RH and Umetsu DT. Pulmonary dendritic cells producing IL-10 mediate tolerance induced by respiratory exposure to antigen. Nature Immunol 2001;2:725–731.
36. Akbari O, Freeman GJ, Meyer EH, et al. Antigen-specific regulatory T cells develop via the ICOS–ICOS-ligand pathway and inhibit allergen- induced airway hyperreactivity. Nature Med 2002;8:1024–1032.
37. Valenta R and Kraft D. From allergen structure to new forms of allergen-specific immunotherapy. Curr Opin Immunol 2002;14:718–727.
38. Krieg AM. CpG motifs in bacterial DNA and their immune effects. Annu Rev Immunol 2002;20:709–760.
39. Akira S and Takeda K. Toll-like receptor signalling. Nature Rev Immunol 2004;4:499–511.
40. Duramad O, Fearon KL, Chan JH, et al. IL-10 regulates plasmacytoid dendritic cell response to CpG-containing immunostimulatory sequences. Blood 2003;102:4487–4492.
41. Friedberg JW, Kim H, McCauley M, et al. Combination immunotherapy with a CpG oligonucleotide (1018 ISS) and rituximab in patients with non-Hodgkin

lymphoma: increased interferon-alpha/beta-inducible gene expression, without significant toxicity. Blood 2004;105:489–495.

42. Tighe H, Takabayashi K, Schwartz D, et al. Conjugation of immunostimulatory DNA to the short ragweed allergen amb a 1 enhances its immunogenicity and reduces its allergenicity. J. Allergy Clin Immunol 2000;106:124–134.
43. Sabatel C, Radermecker C, Laurence F, et al. Exposure to bacterial CpG DNA protects airway allergic inflammation by expanding regulatory lung interstitial macrophages. Immunity 2017;46:457–473.
44. 44. McGuirk P and Mills KH. Pathogen-specific regulatory T cells provoke a shift in the $T_H1/T_H2$ paradigm in immunity to infectious diseases. Trends Immunol 2002;23:450–455.
45. 45. Joint Task Force on Practice Parameters. Allergen immunotherapy: a practice parameter. American Academy of Allergy Asthma and Immunology. American College of Allergy, Asthma and Immunology. Ann Allergy Asthma Immunol 2003;90(1 supplement 1):1–40.
46. 46. Agostinis F, Tellarini L, Canonica GW, et al. Safety of sublingual immunotherapy with a monomeric allergoid in very young children. Allergy 2005;60:133.
47. Dong X, Bachman LA, Kumar R, et al. Generation of antigen-specific, interleukin-10-producing T-cells using dendritic stimulation and steroid hormone conditioning. Transpl Immunol 2003;11:323–333.
48. Hawrylowicz C, Richards D, Loke TK, et al. A defect in corticosteroid-induced IL-10 production in T lymphocytes from corticosteroid-resistant asthmatic patients. J Allergy Clin Immunol 2002;109:1369–370.

49. Tsai M-L, Chen R-H, Bai S-W, et al. The storage stability of chitosan/tripolyphosphate nanoparticles in a phosphate buffer. Carbohydr Polym 2011;84:756–761.
50. Fröhlich E. The role of surface charge in cellular uptake and cytotoxicity of medical nanoparticles. Int J Nanomedicine 2012;35:5577–5591.
51. Huang M, Ma Z, Khor E, et al. Uptake of FITC-chitosan nanoparticles by A549 cells. Pharm Res 2002;19:1488–1494.
52. Lehr, C. M. (1994) The transcytosis approach, in Drug Absorption Enhancement: Concepts, Possibilities, Limitations and Trends (de Boer, AG., ed.), Harwood Academic, Amsterdam, The Netherlands, 1994, pp. 325–366.
53. Schipper NG, Olsson S, Hoogstraate JA, et al. Chitosans as absorption enhancers for poorly absorbable drugs 2: mechanism of absorption enhancement. Pharm Res 1997;14:923–929.
54. 54. Liang SC, Tan XY, Luxenberg DP, Karim R, Dunussi-Joannopoulos K, Collins M, et al. Interleukin (IL)-22 and IL-17 are coexpressed by Th17 cells and coopera- tively enhance expression of antimicrobial peptides. J Exp Med 2006;203:2271–2279.
55. Eyerich S, Eyerich K, Pennino D, Carbone T, Nasorri F, Pallotta S, et al. Th22 cells represent a distinct human T cell subset involved in epidermal immunity and remodeling. J Clin Invest 2009;119:3573–3585.
56. Duhen T, Geiger R, Jarrossay D, Lanzavecchia A, Sallusto F. Production of inter- leukin 22 but not interleukin 17 by a subset of human skin-homing memory T cells. Nat Immunol 2009;10:857–863.
57. Colonna M. Interleukin-22-producing natural killer cells and lymphoid tissue inducer-like cells in mucosal immunity. Immunity 2009;31:15–23.

58. Trifari S, Kaplan CD, Tran EH, Crellin NK, Spits H. Identification of a human helper T cell population that has abundant production of interleukin 22 and is distinct from T(H)-17, T(H)1 and T(H)2 cells. Nat Immunol 2009;10:864–871.
59. 59. Eyerich S, Onken AT, Weidinger S, Franke A, Nasorri F, Pennino D, et al. Mutual antagonism of T cells causing psoriasis and atopic eczema. N Engl J Med 2011;365:231–238
60. 69. Crellin NK, Trifari S, Kaplan CD, Cupedo T, Spits H. Human NKp441IL-221 cells and LTi-like cells constitute a stable RORC1 lineage distinct from conven- tional natural killer cells. J Exp Med 2010;207:281–290.
61. 61. Jones BC, Longsdon NJ and Walter MR. Structure of IL-22 bound to its high affinity IL22-R1 chain. Structure 2008;16:1333-1344.
62. 62. Eyerich S, Eyerich K, Cavani A, Schmidt-Weber C. IL-17 and IL-22: siblings, not twins. Trends Immunol 2010;31:354–361.
63. Wolk K, Kunz S, Witte E, Friedrich M, Asadullah K, Sabat R. IL-22 increases the innate immunity of tissues. Immunity 2004;21:241–254.
64. Pociask DA, Scheller EV, Mandalapu S, et al. IL-22 is essential for lung epithelial repair following influenza infection. Am J Pathol 2013;182:1286–1296.
65. Sonnenberg GF, Nair MG, Kirn TJ, et al. Pathological versus protective functions of IL-22 in airway inflammation are regulated by IL17A. J Exp Med 2010;207:1293–1305.
66. 66. Besnard AG, R. Sabat, L. Dumoutier, et al. Dual role of IL-22 ion allergic airway inflammation and its cross-talk with IL17A. Am J Respir Crit Care Med 2011;183:1153–1163.

67. An SS, Mitzer W, Tang WY, et al. An inflammation-independent contraction mechanophenotype of airway smooth muscle in asthma. J Allergy Clin Immunol 2016;138:294–297.
68. Fang P, Zhou L, Zhou Y, et al. Immune modulatory effects of IL-22 on allergen-induced pulmonary inflammation. PLoS One 2014;9:e107454.
69. K. Nakagome, M. Imamura, K. Kawarata, et al. High expression of IL-22 supresses antigen-induced immune responses and eosinophilic airway inflammation via an IL-10-associated mechanism. J Immunol 2011;187:5077–5089.
70. Pennino D, Bhavsar PK, Effner R, et al. IL-22 supresses IFN-γ-mediated lung inflammation in asthmatic patients. J Allergy Clin Immunol 2013;131:562–570.
71. Lejeune D, Dumoutier L, Constantinescu, S, et al. Interleukin-22 (IL-22) activates the JAK/STAT, ERK, JNK, and p38 MAP kinase pathways in a rat hepatoma cell line: pathways that are shared with and distinct from IL-10. J Biol Chem 2002;277:33676–33682.
72. Moore KW, de Waal Malefyt R, Coffman RL, et al. Interleukin-10 and the interleukin-10 receptor. Annu Rev Immunol 2001;19:683–765.
73. Ito T, Hirose K, Saku A, et al. IL-22 induces Reg3 and inhibits allergic inflammation in house dust mite-induced asthma models. J Exp Med 2017;214:3037–3050.
74. Takahashi K, Hirose K, Kawashima S, et al. IL-22 attenuates IL-25 production by lung epithelial cells and inhibits antigen-induced eosinophilic airway inflammation. J Allergy Clin Immunol 2011;128:1067–1076.

## CONCLUDING REMARKS AND FUTURE PERSPECTIVES

Chitosan, chitosan derivatives, chitosan/anionic materials and carboxymethyl chitosan/cationic materials complexes can be designed by enhancing the physicochemical properties for biological products delivery for immunotherapy and vaccination respectively.

Chitosan-based adjuvant systems have been developed with versatility in formulation, excellent tolerance, distinct mucoadhesivity, and a robust capacity to stimulate cellular and humoral immunity in both clinical and pre-clinical studies. Application of these adjuvant systems would significantly improve vaccine development to meet the needs of reduced cost, increased stability, and easier administration. However, only a few chitosan adjuvant systems have been approved for clinical trials, and none of them have yet been included in a licensed vaccine product.

The present work deals with chitosan and chemically modified chitosan nanoparticles targeted for use as biological products delivery systems. Importantly, this study demonstrated that these nanoparticles can be stabilized during freeze-drying process when using adequate concentrations of suitable excipients.

While the use of carboxymethyl chitosan has expanded in recent decades, this may have been limited because it has to be synthetized, in contrast to CS, which is an easily obtained pharmaceutical ingredient. Despite these derivatives are produced by organic synthesis, the process is easy and produces good yields. Furthermore, the production of such derivatives does not require expensive pharmaceutical ingredients and reagents and, therefore, industrial scale production is extremely feasible.

Chitosan derivatives-based delivery systems appear to be interesting because of the practical applicability of these modified polymers. Solubility is an important characteristic for modulating drug release and changing production processes that generate materials with appropriate properties for the intended use.

Most of the studies using chitosan derivatives as delivery systems were focused on drug delivery tests, which showed the effective control of drug release. However, few studies have been conducted in animal models, although cellular studies have revealed that these systems showed good properties. Additionally, studies performed in mammalian models have shown that chitosan derivatives-based delivery systems are nontoxic and biocompatible. Therefore, it is possible to control the release of biological products and increase their absorption, which subsequently increases or maintains pharmacodynamic biological responses as shown in this study. Moreover, the present study shows the enormous potential these polymers have for use as in delivery systems.

The use of these chitosan derivatives is increasing in the research and development of delivery systems, and these advances could be remarkable and will manifest themselves in new publications in the coming years. However, future research is needed to investigate the mode of action of chitosan and chitosan derivatives, based on its different properties, and establish criteria for advancing chitosan development. We envisage a booming future for chitosan and its derivatives as adjuvants in novel mucosal vaccine formulations. Although there are hurdles that still need to be overcome, it is reasonable to expect that it will not be very long before chitosan-based delivery systems for vaccines are released onto the market.

# ATTACHMENTS